

First-principles Theoretical Analysis of Thermoelectric Properties and Electronic Topological Transitions in Chalcogenides

A Thesis

Submitted in partial fulfillment for the Degree of

MASTER OF SCIENCE

as a part of Integrated Ph.D. programme in

MATERIALS SCIENCE

by

Raagya Arora



CHEMISTRY AND PHYSICS OF MATERIALS UNIT
JAWAHARLAL NEHRU CENTRE FOR ADVANCED SCIENTIFIC RESEARCH
Bangalore – 560 064

MARCH 2019

To my parents and sister

DECLARATION

I hereby declare that the matter embodied in the thesis entitled “**First-principles Theoretical Analysis of Thermoelectric Properties and Electronic Topological Transitions in Chalcogenides**” is the result of investigations carried out by me at the Chemistry and Physics of Materials Unit, Jawaharlal Nehru Centre for Advanced Scientific Research, Bangalore, India under the supervision of Prof. Umesh V. Waghmare and that it has not been submitted elsewhere for the award of any degree or diploma.

In keeping with the general practice in reporting scientific observations, due acknowledgement has been made whenever the work described is based on the findings of other investigators.

Raagya Arora

CERTIFICATE

I hereby certify that the matter embodied in this thesis entitled “**First-principles Theoretical Analysis of Thermoelectric Properties and Electronic Topological Transitions in Chalcogenides**” has been carried out by Ms. Raagya Arora at the Chemistry and Physics of Materials Unit, Jawaharlal Nehru Centre for Advanced Scientific Research, Bangalore, India under my supervision and that it has not been submitted elsewhere for the award of any degree or diploma.

Prof. Umesh V. Waghmare
(Research Supervisor)

Acknowledgements

First of all I want to thank my supervisor Prof. Umesh V. Waghmare whom I owe deepest gratitude for his constant support, guidance and motivation all through the academic and non academic work. The work which I have done, would not be possible without his help and advices. Working with him has been a thoroughly enjoyable experience, and his contagious enthusiasm for science has motivated me at various times. His valuable comments and instructions in preparing presentations, posters, seminars and writing papers have helped me immensely. I am extremely grateful for his kindness, endless support and encouragement.

I am very grateful to all the members of the Materials Theory Group who helped me in many ways during my MS thesis and in fact I have learned a lot from seniors specially Dr. Koushik Pal, Pawan, Suchitra, Meha, Dr. Anjali Singh and Lakshay. I would also like to thank other members of the group Narendra, Koyendrila, Shivani, Shashank, Rajendra, Dr. Sweta, Dr. Anuja, Dr. Prasad, Dr. Sampath and Dr. Shazia.

The life outside lab was made enjoyable by my Integrated Ph.D. batch-mates Pragya, Nijita, Tarandeep, Shashank, Brijesh, Ashutosh and Shivani. I am grateful to them for teaching important life lessons and to the fun times we spent during coursework. I will always cherish the enjoyable time we shared during the stay at NVSH. I also owe a lot to the senior Ph.D. and Integrated Ph.D. students whose help (or advices) made both my academic and non-academic life a memorable and a comfortable one here at JNC.

I am highly indebted to Prof. S. Balasubramanian, Prof. A. Sundaresan, Prof. S. M. Shivaprasad, Prof. C. Narayana, Prof. K. S. Narayan, Prof. G. U. Kulkarni, Prof.

R. Ganapathy, Prof. R. Datta, Prof. T. K. Maji, Prof. M. Eswaramoorthy, Prof. S. Narasimhan, Prof. U. V. Waghmare, Prof. Vidhyadiraja, Prof. Sarit Agasti, Prof. Sridhar Rajaram, Prof. Meher Prakash, Prof. Swapan Pati, Prof. Subir K. Das and Prof. A. Chakraborty (IISc) whose classes during the coursework greatly helped me in my research. Being friendly to the students always, it's been a great pleasure to discuss with them about any scientific and non-scientific issues.

I want to thank my collaborators Prof. A. K. Sood, Prof. Kanishka Biswas, Prof. Chandrabhas Narayana, Dr. Ananya Banik, V. Rajaji, Subhajit Roychowdhury, Dr. Tanmoy Ghosh, Sukanya Pal. I thank them for engaging me in exciting and rigorous scientific interactions and meetings. Working with experimentalists has helped me gain better understanding of the problem. I am highly motivated by their way of questioning the subject in a deeper level.

I would like to sincerely thank Prof. C.N.R Rao, FRS, for being a person I will always look up to for the rest of my life. I convey deepest respect to those teachers in my school and college who always inspired and motivated me to pursue higher studies. I am grateful to few of the people I met in JNC specially Nimish, Nikhil, Srinath, Srimayee, Harshit, Geetika, Ekashmi, Amit, Aditi, Navin, Sushmita, Shantanu, Abhijit, Reetendra and Sudarshan who have made the journey in JNC memorable so far. A special thanks to the Cultural committee members with whom I share a special bond and loved organising all the events. I am grateful to my friends Supriya, Radhika, Subhi, Alvina, Harshal, Sravya, Prantika, Rupika and Surbhi for their immense motivation and support.

A special thanks to my brother Parth and nani for their unconditional support at all stages of life. My sincere thanks also goes to my friend Subhi who was always there to support me in the best and the worst times.

Finally, it will be an incomplete task if I forget to acknowledge my parents. It's their unconditional love and support which has motivated me to fulfil my dreams. Last but not least, I would like to thank my sister Pragya for always standing by me in all situations.

Synopsis

The theoretical and experimental advancements in science have led to tremendous technological growth. One of the most significant factors contributing towards it is the discovery of materials exhibiting exotic properties and improved efficiency. With advances in computational resources first-principles Density functional theory (DFT) based calculations have played significant role in predicting, designing and understanding novel functional materials and their properties. The central idea involves microscopic investigation of various macroscopic properties of materials.

The work in my M.S. thesis focusses on studying materials with non-trivial electronic topology using first-principles calculations based on density functional theory (DFT). DFT calculations have proven to be very useful and effective in studying electronic topology of materials and in analysing and predicting pressure induced topological quantum phase transitions. Another important aspect of this thesis involves determination and analysis of thermoelectric properties of materials. The motivation of our theoretical analysis lies in getting a deeper understanding of the experimental strategies employed by experimentalists to design materials with improved thermoelectric performance. We have studied the above mentioned properties in a particular class of materials termed as “Chalcogenides”. These exhibit rich compositional and structural diversity and constitute one of the most important classes in the field of chemistry.

In chapter 1, we present a brief introduction to the theme of this thesis followed by methods and formalism used in our calculations in chapter 2. The thesis is broadly divided into two parts based on the properties we have studied.

In the **first part** (chapter 3-4), we focus on thermoelectric properties of materials. Specifically we have studied the effect of alloying and cationic substitution on two specific chalcogenides. In chapter 3 we devised an efficient strategy of engineering the local structural distortions and the associated ferroelectric instability in crystalline solids which induces soft polar phonons. The strong coupling of these soft polar phonons with acoustic phonons carrying heat minimizes lattice thermal conductivity in lead free $SnTe$. This strategy opens up a new avenue of achieving high thermoelectric performance as many materials encompass such a ferroelectric instability. In chapter 4 we have studied the alloying of $AgBiSe_2$ with $GeSe$. Interestingly, cubic $(GeSe)_{1-x}(AgBiSe_2)_x$ possess n-type conduction with reasonable high carrier concentration, which is rare in Ge-chalcogenides based thermoelectrics.

In the **second part** (chapter 5-6), we focus on the pressure induced topological quantum phase transitions in materials belonging to different symmetry and topological classes. Chapter 5 deals with pressure induced changes in the electronic topology of $TlBiS_2$ in the low pressure regime (< 4 GPa) which we confirmed using the Z_2 topological invariant and the mirror chern number n_M calculated at various pressures. In chapter 6 we study the pressure induced phase transitions in a topological crystalline insulator SnTe and a normal semiconductor SnSe.

Density functional theory simulations have thus proved to be powerful tools in selecting materials for given application based on concerns of cost and performance, in understanding the confines of materials and also shown ability to engineer new materials with designer properties.

List of Publications

1. “Stabilizing n-Type Cubic $GeSe$ by Entropy-Driven Alloying of $AgBiSe_2$: Ultralow Thermal Conductivity and Promising Thermoelectric Performance”, Subhajit Roychowdhury, Tanmoy Ghosh, **Raagya Arora**, Umesh V Waghmare, Kanishka Biswas, *Angewandte Chemie* **130**, 15387 (2018).
2. “Engineering ferroelectric instability to achieve ultralow thermal conductivity and high thermoelectric performance in $Sn_{1-x}Ge_xTe$ ”, Ananya Banik, Tanmoy Ghosh, **Raagya Arora**, Moinak Dutta, Juhi Pandey, Somnath Acharya, Ajay Soni, Umesh V. Waghmare and Kanishka Biswa, *Energy & Environmental Science* **12**, 589 (2019).
3. “Phonon signatures of multiple topological quantum phase transitions in compressed $TlBiS_2$: A combined experimental and theoretical study”, V. Rajaji, **Raagya Arora**, Saurav Ch. Sarma, B. Joseph, Umesh V. Waghmare, Sebastian C. Peter, and Chandrabhas Narayana, (under review in *Phys. Rev. B*).
4. “Raman study of pressure induced phase transitions in a topological crystalline insulator $SnTe$ and a normal semiconductor $SnSe$ ”, Sukanya Pal, **Raagya Arora**, Subhajit Roychowdhury, Kaniska Biswas, D. V. S. Muthu, U. V. Waghmare, and A. K. Sood, (Preprint available).

List of Figures

1.1	<i>Generic diagram of a thermoelectric couple made of n-type and p-type thermoelectric materials. Power generation or refrigeration modes are possible, depending on the configuration</i>	6
2.1	<i>Flow chart showing the self-consistency loop for the iterative solution of Kohn-Sham equations.</i>	30
2.2	<i>Schematic representation of all-electron (dashed lines) and pseudoelectron (solid lines) potentials and their corresponding wavefunctions. The radius at which all electron and pseudoelectron value matches is designated r_c. This figure is taken from https://en.wikipedia.org/wiki/Pseudopotential.</i> . . .	35
2.3	<i>Schematic representation of a LAPW basis set. The unit cell is divided into atom centered region and interstitial region.</i>	36

-
- 3.1 *Phonon dispersion of (a) SnTe and (b) Sn_{0.75}Ge_{0.25}Te in the centrosymmetric cubic rock salt structure at the theoretical lattice parameter without the inclusion of spin-orbit coupling (SOC), exhibiting unstable modes frequencies at 23i cm⁻¹ and 93i cm⁻¹ respectively. Vibrational density of states (VDOS) of (a) SnTe and (b) Sn_{0.75}Ge_{0.25}Te, show significantly larger number of unstable modes in the latter, which also mask notably stronger instability (c). Dependence of the squared frequencies of unstable phonon at zone centre on hydrostatic strain where strain is $(a - a_0)/a_0$ with $a_0 = 6.37 \text{ \AA}$ for SnTe and $a_0 = 6.28 \text{ \AA}$ for Sn_{0.75}Ge_{0.25}Te (d). The slope $\partial\omega_0^2(\epsilon)/\partial\epsilon$ of Sn_{0.75}Ge_{0.25} is significantly steeper than that of SnTe, signifying its stronger strain phonon coupling. 52*
- 3.2 *Visualisation of the atomic displacements of unstable phonons at the zone centre of (a) SnTe and (b) Sn_{0.75}Ge_{0.25}Te, Sn (Red in colour), Te (Blue in colour), and Ge (Pink in colour). There are equal and opposite displacements Sn and Te atoms in (a) SnTe, whereas the displacements of Ge atoms completely dominate the lattice instability in (b) Sn_{0.75}Ge_{0.25}Te. . . 53*
- 3.3 *Phonon dispersion of (a) off-centred Sn_{0.75}Ge_{0.25}Te in the centrosymmetric cubic rock salt structure without the inclusion of spin-orbit coupling (SOC) and the corresponding vibrational density of states (VDOS)(b). Γ Phonons of FE state of Sn_{0.75}Ge_{0.25}Te do not exhibit any unstable modes. 54*
- 3.4 *Electronic structure of cubic (Fm $\bar{3}$ m) phase of SnTe and off-centred Sn_{0.75}Ge_{0.25}Te calculated with the inclusion of effects of spin-orbit coupling (a) and the corresponding electronic density of states (b). 55*
- 3.5 *Total energies of Ge off-centred, all cations off-centred and without any off-centred Sn_{1-x}Ge_xTe systems with (a) $x = 0.125$ and (b) $x = 0.25$. . . 56*

-
- 4.1 *A possible phase diagram of the GeSe–AgBiSe₂ system based on temperature-dependent PXRD and DSC data(a). The evolution of the experimental band gap of GeSe with increasing AgBiSe₂ concentration in (GeSe)_{1-x}(AgBiSe₂)_x 64*
- 4.2 *Crystal structure of different phases of GeSe: orthorhombic (O), rhombohedral (R), and cubic (C). Ge Yellow, Se blue; Ag red, Bi cyan 65*
- 4.3 *Electronic structure of eight atoms FCC (1×1×1) (a) (GeSe)_{0.6}(AgBiSe₂)_{0.4} and (b) offcentered structure calculated with (black color lines) and without (red color lines) the inclusion of spinorbit interaction (SOI). Zoomed version of electronic structure of cubic (GeSe)_{0.60}(AgBiSe₂)_{0.40} (1×1×2, 16 atoms) at (c) M point and (d) A point which clearly shows conduction band minima and valence band maxima don't cross each other. 66*
- 4.4 *Electronic band structure of a) orthorhombic GeSe, b) rhombohedral, and c) cubic (GeSe)_{0.90}(AgBiSe₂)_{0.10} and (GeSe)_{0.60}(AgBiSe₂)_{0.40} respectively with (black lines) and without (red lines) the inclusion of spin-orbit coupling (SOC). 68*
- 4.5 *Electronic density of states (DOS) and projected density of states (PDOS) of (a) GeSe (orthorhombic), (b) (GeSe)_{0.9}(AgBiSe₂)_{0.1} (rhombohedral) and (c) (GeSe)_{0.6}(AgBiSe₂)_{0.4} (cubic) calculated with inclusion of the spin-orbit coupling. 69*
- 5.1 *Unit cell of the hexagonal (supercell) phase of TlBiS₂ (violet, blue, and red spheres represents the Tl, Bi, and S atoms respectively). 79*
- 5.2 *(a) – (f) Electronic structure of TlBiS₂ are calculated with spin-orbit coupling at different hydrostatic pressures (from -1 GPa to 4 GPa). Band inversion takes place at the Γ and F points in the Brillouin zone as a function of pressure near $P_C = -0.4$ GPa and $P_C = 3.6$ GPa, respectively. . . 81*

-
- 5.3 *Isosurfaces of charge densities associated with valence band maxima (VBM) and conduction band minima (CBM) before and after the band inversion at the Γ point (a) and the F point (b) reveal that the band inversion at Γ takes place in between -0.3 GPa and -0.5 GPa (i.e., $-0.5 < P_C < -0.3$ GPa, hence $P_C \sim -0.4$ GPa at Γ point), whereas the band inversion at the F point occurs in between 3.5 and 3.7 GPa (i.e., $3.5 < P_C < 3.7$ GPa, $P_C \sim 3.6$ GPa at F point). 82*
- 5.4 *Electronic structures of rhombohedral TlBiS₂ around the Γ point (a) and the F point (b) showing the band inversion between the top valence and lowest conduction bands as a function of hydrostatic pressures. Band inversion takes place in the Brillouin zone near $P_C = -0.4$ GPa at Γ point and $P_C = 3.6$ GPa at F point. Electronic density of states of TlBiS₂ calculated with spin-orbit coupling at different hydrostatic pressures (c). Evolution of band gap with hydrostatic pressure at Γ and F points showing opening and closing of gaps at the critical pressures (P_C^{Γ} and P_C^F). 83*
- 5.5 *Phonon dispersion of TlBiS₂ for theoretical lattice constant at 0 GPa (a). At 0 GPa negative frequencies are not present in the system indicating a stable structure.(b)Experimental Raman spectrum of TlBiS₂ at an ambient conditions, and (c) visualization of the atomic displacement patterns for the E_g and A_{1g} modes obtained from calculations. 85*
- 5.6 *Changes in the DFT calculated frequencies of Raman active, (a) E_g and (b) A_{1g} modes of TlBiS₂ with pressure (from 0 GPa to 4 GPa). The changes in the electron phonon coupling of these modes are shown in (c,d). There are changes in slope ($=d\omega/dP$) of pressure dependence of both the Raman active phonon modes at ~ 3 GPa. 86*

-
- 6.1 *Electronic structure of cubic ($Fm\bar{3}m$) phase of SnTe calculated with spin-orbit coupling at (a) 0 GPa, (b) 2 GPa and (c) 4 GPa and variation in VBM and CBM with pressure at the L point of the Brillouin zone (d). Isosurfaces of charge densities (e) associated with electronic states at valence band maximum (VBM), conduction band minimum (CBM) and 2nd conduction band minimum at L point below (a) and above (b) the critical pressure revealing inversion of the lowest two conduction bands at this transition. 98*
- 6.2 *Calculated phonon dispersion of the cubic ($Fm\bar{3}m$) structure of SnTe at pressures ranging from 0 GPa to 5 GPa (a), exhibiting imaginary phonon frequencies depicting the instability of cubic structure at $P = 0$ GPa. One and two phonon density of states of cubic SnTe at 0 GPa (b). Calculated frequency ω of the optical phonon (Γ_{15}) at Γ point as a function of pressure showing an anomaly at low pressures and its electron-phonon coupling in (d). Evolution of one phonon DOS (e) and two phonon DOS (f) with hydrostatic pressure ranging from 0 GPa to 3 GPa. 99*
- 6.3 *Pressure dependent enthalpy (ΔH) of cubic $Fm\bar{3}m$, orthorhombic $Pnma$ (GeS), $Cmcm$ and cubic $Pm\bar{3}m$ phases of SnTe relative to the orthorhombic $Pnma$ phase 100*
- 6.4 *Electronic structure of the orthorhombic ($Pnma$) structure of SnTe at $P = 6$ GPa (a), 8 GPa (b), 11 GPa (c), 12 GPa (d), 13 GPa (e) and 16 GPa (f) calculated with the inclusion of effects of the spin orbit coupling and corresponding electronic density of states showing enhanced metallicity with increasing pressure (g). 101*

6.5	<i>Electronic structure of the orthorhombic Pnma (GeS type) structure of SnTe at P = 6 GPa (a), 8 GPa (b), 10 GPa (c), 12 GPa (d), 13 GPa (e) and 16 GPa (f) calculated with the inclusion of spin-orbit coupling. Electronic density of states calculated with spin-orbit coupling at different hydrostatic pressures (g).</i>	102
6.6	<i>Frequencies of the zone centre (Γ) optical phonons of Pnma and Pnma (GeS type) phases at 16 GPa showing notably softer optical phonon modes of Pnma (GeS) phase in comparison to Pnma phase</i>	103
6.7	<i>Electronic structure of the orthorhombic (Pnma) structure of SnSe at P = 0 GPa (a), 2 GPa (b), 3 GPa (c), 4 GPa (d), and 6 GPa (e) calculated with the inclusion of effects of the spin-orbit coupling and corresponding electronic density of states showing enhanced DOS at Fermi level with increasing pressure (f)</i>	104
6.8	<i>Pressure dependent enthalpy (ΔH) of the orthorhombic Pnma phase of SnTe relative to the orthorhombic Cmcm phase, demonstrating a structural phase transition from Pnma to Cmcm phase at P = 6.3 GPa</i>	105
6.9	<i>Electronic structure of the orthorhombic (Cmcm) structure of SnSe at P = 0 GPa (a), 7 GPa (b), 8 GPa (c), 9 GPa (d), 12 GPa (e), 13 GPa (f) and 16 GPa (g) calculated with the inclusion of spin-orbit coupling and corresponding electronic density of states (h).</i>	106
6.10	<i>Phonon dispersion of orthorhombic (Cmcm) structure of SnSe at P = 9 GPa (a), 12 GPa (b) and 16 GPa (c) calculated along the XΓ direction.</i>	107

List of Tables

3.1 Γ Phonons of FE state of $Sn_{0.75}Ge_{0.25}Te$ do not exhibit any unstable modes in comparison to unstable modes in $SnTe$ and $Sn_{0.75}Ge_{0.25}Te$ 54

4.1 Off-centring displacements of atoms in the cubic structure of $(GeSe)_{0.6}(AgBiSe_2)_{0.4}$ obtained after relaxation of the structure. 67

5.1 Mirror Chern number (n_M) and Z_2 topological index of $TlBiS_2$ calculated at 3.5 GPa and 3.7 GPa. The second band inversion at F around $P_C^\Gamma \sim 3.6$ GPa results in a TCI phase characterized by n_M and $\nu_0=0$ (trivial with respect to Z_2 topological insulators 84

Contents

Acknowledgements	v
Synopsis	vii
1 Introduction	1
1.1 Metal Chalcogenides	3
1.1.1 Chalcogenides of p-block elements	4
1.2 Introduction to Thermoelectrics	5
1.2.1 Thermoelectric figure of merit (ZT)	5
1.3 Conflicting thermoelectric parameters	7
1.3.1 Carrier concentration	7
1.3.2 Effective mass	8
1.3.3 Electrical thermal conductivity	8
1.3.4 Lattice thermal conductivity	8
1.3.5 Ways to achieve high performance	9
1.4 Distinct topological phases of matter	10
1.4.1 Quantum Hall effect and Quantum anomalous Hall effect	11
1.4.2 Quantum spin Hall effect	12
1.4.3 Z ₂ topological insulators	12
1.5 Elements of topological band theory	14
1.5.1 Bulk-boundary correspondence principle	14
1.5.2 Berry curvature and Berry phase	14

1.5.3	Chern number	15
1.5.4	Z_2 invariants	15
1.5.5	Mirror Chern Number	16
Bibliography		18
2 Methods and Formalism		22
2.1	Basic equations for interacting electrons and nuclei	23
2.1.1	Adiabatic Born-Oppenheimer Approximation	24
2.1.2	Classical nuclei approximation	25
2.1.3	Independent electron approximation	25
2.2	Density functional theory	26
2.2.1	Thomas-Fermi theory	26
2.2.2	Hohenberg-Kohn theorem	27
2.2.3	Kohn-Sham approach	28
2.2.4	Basis Set	31
2.2.5	Approximation to exchange & correlation energy	32
2.2.6	Pseudopotentials	34
2.2.7	Linearized Augmented Plane Wave (LAPW) method	36
2.3	Phonons	37
2.3.1	Frozen-phonon approach	38
2.3.2	Density functional perturbation theory	38
2.4	Wannier functions in electronic structure calculation	39
2.4.1	Maximally localized Wannier function (MLWF)	41
2.4.2	Calculation of Z_2 invariants via WCC	42
Bibliography		45
3 Engineering ferroelectric instability to achieve ultralow thermal conductivity and high thermoelectric performance in $Sn_{1-x}Ge_xTe$		47

3.1	Introduction	47
3.2	Computational Details	49
3.3	Results and Discussions	50
3.4	Conclusion	56
	Bibliography	57
4	Stabilizing n-Type Cubic GeSe by Entropy-Driven Alloying of AgBiSe₂: Ultralow Thermal Conductivity and Promising Thermoelectric Performance	61
4.1	Introduction	61
4.2	Computational Details and Crystal Structure	63
4.3	Results and Discussion	65
4.4	Conclusion	69
	Bibliography	71
5	Phonon signatures of multiple topological quantum phase transitions in compressed TlBiS₂	74
5.1	Introduction	74
5.2	Computational Details and Crystal Structure	77
5.3	Results and Discussions	79
5.3.1	Evolution of electronic structure	79
5.3.2	Calculation of topological invariants	81
5.3.3	Vibrational Properties	84
5.4	Conclusions	86
	Bibliography	88
6	Raman study of pressure induced phase transitions in a topological crys- talline insulator SnTe and a normal semiconductor SnSe	91

6.1	Introduction	91
6.2	Computational Methods	94
6.3	Results and Discussion	95
6.3.1	SnTe	95
6.3.2	SnSe	103
6.4	Conclusions	108

Bibliography	109
---------------------	------------

Chapter 1

Introduction

The importance of materials has been known and realized for ages. Dating back to 3000 BC the significant contribution of materials in the development of civilization was recognized. Starting from the origin of human life on Earth, the Stone Age to the Bronze Age and more recently the use of iron and steel around 1850, which enabled the railroads and helped in the building of the modern infrastructure of the industrial world the central commonality has been materials. Starting in the 1930s understanding of how materials behave in a certain way, and why they differ in properties was made possible with the atomistic understanding allowed by quantum mechanics, that first explained atoms and then solids. The central domain of Materials Science involves the combination of physics, chemistry, and the focus on the relationship between properties of a material and its microstructure. The development of this field allowed designing new materials and provided a knowledge base for engineering applications. Properties are the materials way of responding to the environment. For example, the mechanical, electrical and magnetic properties are the responses to mechanical, electrical and magnetic forces, respectively. Other important properties include thermal (heat capacity, transmission of heat), optical (absorption, transmission, and scattering of light), and the chemical stability in contact with the environment. Material science involves selecting materials for a given application based on concerns of cost and performance, to understand the confines of materials and

the ability to create new materials that will have some desirable properties.

The central theme involves determining properties of materials on the macroscopic and intermediate length and time scales through a non-empirical description of their chemistry and microscopic structure. It usually starts with computational solution of electronic motion treated within a quantum mechanical density functional theory and identifies the lowest energy degrees of freedom and their interactions. Every material consists of electrons and ions. Microscopic investigations of various macroscopic properties of a material reveal that most of the properties arise due to the interaction between the electrons and the ions and the interaction among themselves. The behavior of these atomic and subatomic particles can best be described by quantum theory very accurately. Nearly all physical properties of materials are related to total energies or difference between total energies [1–4] of the electrons and ions.

To get the total energy of a system containing electrons and ions, the aim is to solve the Schrödinger equation. But solving the Schrödinger equation is a difficult task as electronic degrees of freedom are coupled to ionic degrees of freedom giving rise to a coupled differential equation. Moving towards complex systems that contain many electrons and ions, solving the Schrödinger equation becomes practically an impossible task. In order to tackle this problem, and solve the electronic structure of the condensed phase of a material, Kohn-Sham DFT uses various approximations, where the many body Schrödinger equation is mapped onto a set of self-consistent one-electron equations. Such one-particle Hamiltonian is known as the Kohn-Sham Hamiltonian (KSH). We call this method *ab-initio* because it requires only the specification of atomic number and no other parameters. This thesis contains two applications of *ab-initio* density functional theory in understanding properties of materials.

Electronic structure calculations based on Kohn-Sham density functional theory (DFT) are so far proved to be the most popular and highly successful theory in dealing with condensed matter and materials science problems. DFT has shown extraordinary accuracy in forecasting and explaining the macroscopic as well as microscopic properties of materials

in the bulk form, surfaces and interfaces. This predictive capability of DFT along with advances in supercomputing resources has helped in screening a large number of materials to find the necessary properties, hence reducing the efforts of experimentalists. While some of the predictions can be readily realized within the laboratory, some of them may not be feasible in immediate experimental realization. This confidence, flexibility and success of DFT stem from its ability to compute properties of materials with no adjustable parameters. DFT based calculations are thus helping scientists in making research and scientific exploration of materials cost-effective.

This thesis mainly contains two applications of ab-initio density functional theory to gain an understanding of materials at a deeper level. The thesis revolves around a particular class of materials called "chalcogenides," and the properties we chose to study are thermoelectric properties and electronic topological properties.

1.1 Metal Chalcogenides

Chalcogenides exhibiting rich compositional and structural diversity and constitute one of the most important classes in the field of chemistry, on par with oxides and organic compounds. The term "chalcogen" was proposed around 1930 by Werner Fischer [5] to denote the elements of group 16. It was quickly accepted among German chemists, and was recommended by Heinrich Remy for its official use in 1938 to the International Union of Chemistry (later IUPAC). Following this, it was internationally accepted that the elements oxygen, sulfur, selenium, and tellurium will be called chalcogens and their compounds chalcogenides.

Chalcogenides are compounds that contain at least one chalcogen Q atom ($Q = S, Se, Te$) in a chemically reduced state compared to its elemental form. One of the most distinct differences between oxides and chalcogenides is the ability of the chalcogen to form stable Q-Q bonds: catenation. In general, on moving from sulfides to selenides to tellurides, the degree of covalent bonding, delocalization of electrons and metallic behaviour increase,

and the importance of long range Q-Q interactions increases [6].

Metal chalcogenides have enormous application in many research areas. Some examples include, photovoltaic energy conversion, thermoelectric energy conversion [7, 10], thin-film electronics [12], spintronics [13], fast-ion conductivity [14], catalysis [16], and science in two dimensions [8]. Recently, the sensational discoveries pertinent to metal chalcogenides such as quantum spin Hall Effect [17], topological insulators [18], and many others which have hugely implicated the fields of spintronics and (Opto) electronics. Most of the applications and phenomena are associated with chalcogenides of transition metals and main group p-block metals.

1.1.1 Chalcogenides of p-block elements

The p-block metal chalcogenides exhibit rich structural diversity. In quasi-binary III₂-VI₃ metal chalcogenides wurtzite and zincblende structures are prevalent. Anisotropic layered structures are also found in III-VI compounds with covalently bonded layers stacked via weak van der Waals interactions. Among IV-VI metal chalcogenides, GeQ and SnQ (Q=S, Se) exhibit orthorhombic puckered layered structure, which are derivatives of three-dimensional distorted of the rock salt (NaCl) structures. GeTe and SnTe have rocksalt (NaCl) structures with slight deformations due to phase transitions. For GeTe and SnTe, above 670 K and 100 K respectively the high-temperature phase stabilises in perfect NaCl-structure. PbQ (Q=S, Se, Te) crystallizes in cubic rock-salt structure. Among group V-VI chalcogenides, *Sb₂S₃*, *Sb₂Se₃*, and *Bi₂S₃* have orthorhombic *Sb₂S₃*-type stibnite structure. *Sb₂Te₃*, *Bi₂Se₃*, and *Bi₂Te₃* are found in rhombohedral layered structures comprised of covalently bonded Q-M-Q-M-Q (M=Sb/Bi; Q=Se/Te) quintuple layers stacked via weak van der Waals interactions along the c-axis.

1.2 Introduction to Thermoelectrics

Looking at the current global energy crisis the development of technology for capturing and converting otherwise wasted heat into useful electrical power will be of utmost importance. The class of materials capable of converting thermal gradients into electrical energy or vice versa by virtue of a unique combination of electrical and thermal properties are called thermoelectric (TE) materials. With the coming years TE materials are stated to play a significant role in the energy management [9,10].

Thermoelectric effect is based on two important transport effects: Seebeck effect and Peltier effect. According to Seebeck effect, if two dissimilar metals are joined together with the junctions kept at different temperatures having a temperature difference ΔT , then a resulting voltage difference (ΔV) will be generated [23]. The voltage difference is proportional to ΔT . The ratio of the generated voltage to the temperature difference ($\Delta V / \Delta T$) is related to intrinsic property of the materials and is termed as Seebeck coefficient (S) or the thermopower. By establishing a temperature gradient across a material, the more energetic carriers of hot junction diffuse to a lower potential i.e. cold junction till an electric field is established and the further flow of carriers is inhibited [24].

$$S = \frac{\Delta V}{\Delta T} \quad (1.1)$$

The inverse Seebeck effect is known as Peltier effect where the metal junctions either releases or absorb the heat while current is passed in the close circuit [25].

1.2.1 Thermoelectric figure of merit (ZT)

E. Altenkirch introduced the concept of figure of merit in the early 1900s [25]. It was qualitatively shown that good thermoelectric materials should have high electrical conductivity (σ) (to minimize Joule heating), low thermal conductivity (κ) to prevent heat transport across the junctions leading to maintenance of a large temperature gradient, and large Seebeck coefficients (S) for maximum conversion of heat to electrical power or

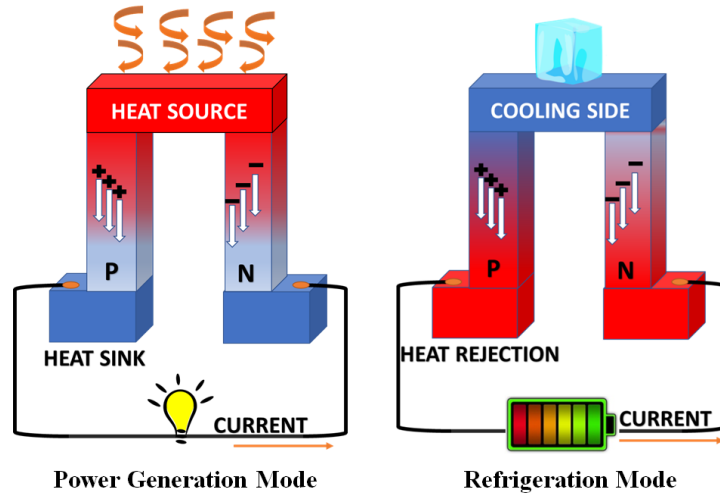


Figure 1.1: *Generic diagram of a thermoelectric couple made of n-type and p-type thermoelectric materials. Power generation or refrigeration modes are possible, depending on the configuration*

vice-versa. These properties define the dimensionless thermoelectric figure of merit, ZT as

$$ZT = \frac{\sigma S^2}{\kappa} T \quad (1.2)$$

where T is the temperature in Kelvin [19, 20, 22, 24]. σS^2 is called the power factor and is the key to achieve high performance. A large power factor implies higher current generation. The thermal conductivity κ has a contribution from lattice vibrations, κ_{latt} , called the lattice thermal conductivity. Thus, $\kappa = \kappa_{el} + \kappa_{latt}$, where κ_{el} is the electronic thermal conductivity. For power generation, the thermoelectric efficiency (η) is defined by combining the Carnot efficiency ($\eta_c = \Delta T / T_{hot}$) and the average figure of merit (ZT_{av}) as shown in equation.

$$\eta_{TE} = \eta_c \frac{(\sqrt{1 + ZT_{av}} - 1)}{\left(\sqrt{1 + ZT_{av} + \frac{T_{cold}}{T_{hot}}}\right)} \quad (1.3)$$

where T_{hot} and T_{cold} are the temperature of the hot and cold ends in a thermoelectric device and ΔT is their difference. Improving the efficiency requires both high ZT values and a large temperature difference across the thermoelectric materials.

1.3 Conflicting thermoelectric parameters

A efficient TE material must simultaneously possess, a high σ such that the Joule heating is low, a large S which will result in large potential difference and low κ_L corresponding to a large temperature difference to realize high TE efficiency. One of the most challenging problems in this field is to design a single TE material that meets all the above criteria; moreover, the high interdependence of all the above properties poses an inherent limit to the maximum zT that can be attained in a given material.

1.3.1 Carrier concentration

Large Seebeck coefficient requires only single type of carriers [20]. Mixed n-type and p-type conduction results in both charge carriers moving to the cold end, and hence cancelling out the induced Seebeck voltages. Insulators and semiconductors (low carrier concentration) have very high Seebeck coefficients, and at the same time very low electrical conductivity. The interrelationship between carrier concentration and Seebeck coefficient can be seen from the models of electron transport. For metals or degenerate semiconductors (single parabolic band) the Seebeck coefficient is given by:

$$S = \frac{8\pi^2 k_B^2}{3eh^2} m^* T \left(\frac{\pi}{3n} \right)^{2/3} \quad (1.4)$$

where n is carrier concentration and m^* is effective mass.

Electrical conductivity (σ) is related to n through the following expression.

$$\sigma = ne\mu \quad (1.5)$$

Here μ is carrier mobility. The peak value of ZT arises in the carrier concentration range of 10^{19} - 10^{21} cm^{-3} which falls in between metals and semiconductors that is concentration found in heavily doped semiconductors (degenerate semiconductor) [20, 22].

1.3.2 Effective mass

The effective mass of the charge carrier offers another conflicting problem, large effective mass generates high thermopower but at the same time results in low electrical mobility. The m^* in equation 1.4 refers to the density-of-states effective mass, which increases with flat and narrow bands with high density of states at the Fermi surface. Since the inertial effective mass is related to m^* , heavy carriers move with slower velocities resulting in small mobility, which in turn leads to low electrical conductivity (equation 1.5).

1.3.3 Electrical thermal conductivity

Another conflict in designing materials comes from the requirement of low thermal conductivity [20]. Thermal conductivity in thermoelectrics appears from two sources: (a) electrons and holes transporting heat (κ_{el}) and (b) transport of phonons through the lattice (κ_{latt}). Here κ_{el} is directly related to the electrical conductivity through the Wiedemann–Franz law:

$$\kappa_{el} = L\sigma T \quad (1.6)$$

where L is the Lorenz factor, $2.4 \times 10^{-8} \text{ W}\Omega\text{K}^{-2}$ for free electrons. The Lorenz factor can vary with carrier concentration. Accurate evaluation of κ_{el} is important, as κ_{latt} is often computed as the difference between κ_{total} and κ_{el} using the experimental electrical conductivity.

1.3.4 Lattice thermal conductivity

In a glass, rather than rapid transport via phonons, thermal conductivity is considered as a random walk of energy throughout a lattice leading to the concept of a minimum thermal conductivity, κ_{min} [20]. The reason actual glasses make poor thermoelectrics is because of the absence of needed electron-crystal properties, required for enhanced electrical transport property (σ). Comparison with crystalline semiconductors suggests lower

mobility in glasses is due to increased electron scattering and lower effective masses because of broader bands. Good thermoelectric materials are therefore crystalline materials that are able to scatter phonons without significantly interrupting the electrical conductivity. The heat flow is carried by a spectrum of phonons with widely varying wavelengths and mean free paths (from less than 1 nm to greater than 10 μm), creating a need for phonon scattering agents at a variety of length scales [20].

1.3.5 Ways to achieve high performance

Two approaches are employed to boost zT viz. enhancement of power factor (σS^2) and reduction of thermal conductivity. Some strategies to enhance power factor include: a) engineering of carrier-concentration through chemical doping, b) enhancement of effective carrier mass (m^*) and hence, the Seebeck coefficient either via convergence of multiple valence/conduction band extrema, or distortion of density of states near Fermi level by resonant impurity levels, and c) enhancement of carrier mobility by modulation-doping.¹⁹ On the other hand thermal conductivity is suppressed traditionally through a) point defects, b) endotaxial nanoscale precipitates in the host matrix and c) mesoscale grain boundaries. Sometimes all the above three are incorporated in what are referred to as hierarchical architectures where the atomic scale, nanoscale and mesoscale defects would scatter phonons with a broad range of wavelengths [9, 19]. However, in addition to scattering of phonons, an undesirable scattering of carriers can occur and hence limiting the overall zT in most other TE materials. Taking this consideration into account, materials with intrinsically low thermal conductivity are, therefore, practically more attractive being robust to impurities, doping, grain sizes etc.

In chapter 3 and 4 of my thesis, we present thermoelectric (TE) properties of two chalcogenide materials. In Chapter 3, we present a new strategy to significantly reduce the κ_{lat} without degrading power factor (σS^2) by engineering the ferroelectricity instability in crystalline solid. We have shown that the high lattice anharmonicity caused by the

introduction of Ge atom in SnTe crystal is responsible for its notably lower lattice thermal conductivity. In chapter 4, using first-principles calculations within density functional theory, we reproduce the trend in the evolution of band gap of $(GeSe)_{1-x}(AgBiSe_2)_x$ with increasing x . Interestingly, cubic $(GeSe)_{1-x}(AgBiSe_2)_x$ possess n-type conduction with reasonable high carrier concentration, which is rare in Ge-chalcogenides based thermoelectrics.

1.4 Distinct topological phases of matter

In 1980 the discovery of integer quantum Hall (IQH) effect [26], lead to the realization of robust topologically nontrivial electronic phase in a non-interacting system for the first time. The IQH state possesses robust edge states and exhibits quantized Hall conductivity which are unaffected by the smooth adiabatic changes in the material parameters and hence can not be destroyed without a quantum phase transition. For breaking time reversal (TR) symmetry in IQH effect an external magnetic field is required. Later, TR invariant systems with robust edge/surface states were proposed e.g., in Haldane mode [27] and quantum spin Hall (QSH) insulator [25] which possess nontrivial band topology. It was realized that the strong spin-orbit interaction in non-interacting fermionic systems can give rise to topologically nontrivial phases in the electronic structure.

The topological band theory is the extended branch of band theory of solids that describes the topological physics of non-interacting electronic systems. Berry connection, Berry phase, Chern number are the crucial elements of topological band theory which can be easily formulated and computed within single particle quantum mechanics. Therefore, DFT proves to be a very useful theoretical tool in dealing with materials with nontrivial electronic topology since it accurately treats a material within single particle approximation and also includes the effect of spin-orbit coupling (SOC) in the KS Hamiltonian.

David J. Thouless, F. Duncan M. Haldane and J. Michael Kosterlitz laid the foundations of modern topological phenomena in physics, who in the early 1970s and 1980s

theoretically [27, 29, 30] explained the physics associated with quantum Hall effect [31], superfluid phase transition [32]. Their theory not only unraveled new exotic and unusual quantum states of matter but also opened research activity in topological materials that could be used in future applications of fast electronics, superconductors or even quantum computers. For these pioneering works, David J. Thouless, F. Duncan M. Haldane and J. Michael Kosterlitz were awarded the Nobel prize in physics in 2016 “for theoretical discoveries of topological phase transitions and topological phases of matter”¹. Topological nontrivial phases have been discovered in materials ranging from systems in 1D [33] to 2D materials to even materials in three dimensions.

1.4.1 Quantum Hall effect and Quantum anomalous Hall effect

In 1980 the discovery of quantum Hall (QH) effect [34] in a two-dimensional electron gas system subjected to a strong magnetic field at low temperature kick started the modern research in the field of topological phases of matter. A quantum Hall system exhibits quantized hall conductance $\left(\sigma_{xy} = \nu \frac{e^2}{h}\right)$, which originates from the Berry curvature of the filled magnetic Bloch bands (or Landau level). Topological invariant quantity (ν) known as the Thouless-Khomoto-Nightingale-den Nijs (TKNN) number [36] originates from the integration of the Berry curvature associated with these bands in the Brillouin zone. The conducting edge states in a QH system are robust and their conduction is dissipation-less.

It was in 1982 that Haldane proposed an analogous model known as the Haldane model [27] to realize the quantum Hall effect in a 2D honeycomb lattice. The system did not require an external magnetic field to exhibit quantized conductance $\left(\sigma_{xy} = \nu \frac{e^2}{h}\right)$ with $\nu=1$. In this model, the time-reversal (TR) symmetry of the honeycomb lattice was broken by applying a periodic magnetic field in such a way that the net magnetic flux in a unit cell became zero. The broken TR symmetry lifts the degeneracy of Dirac cone in the electronic structure of the honeycomb lattice and opens up a gap at the Dirac point. In this gapped state, the Chern number of the system is unity. This type of Hall effect,

¹citation from https://www.nobelprize.org/nobel_prizes/physics/laureates/2016/

which does not require any net magnetic field, is known as quantum anomalous Hall effect (QAHE), and an insulating material exhibiting such property is called quantum anomalous Hall insulator or Chern insulator.

1.4.2 Quantum spin Hall effect

The possibility of having a time-reversal invariant topological insulator in two-dimension was first proposed in the Kane-Mele model [35] which is considered to be composed of two copies of the Haldane model with both up and down spin electrons. Addition of spin-orbit interaction term in the Kane-Mele model gives rise to topological insulating state in it. This 2D topological insulator is also known as quantum spin Hall (QSH) insulator that exhibits quantized spin Hall conductance, but with a vanishing charge Hall conductance. After the theoretical prediction of the QSH effect, it was experimentally realized in HgTe/CdTe quantum well heterostructure [38].

However, the presence of spin-orbit coupling (SOC) in a material allows a different topological classification of insulators which are invariant under time-reversal symmetry and also exhibit robust gapless topologically nontrivial edge/surface states. These insulators where TR symmetry is preserved are called Z_2 topological insulators [37], and their associated topological invariants are characterized by Z_2 indices.

1.4.3 Z_2 topological insulators

Strong topological insulator

The concept of topological insulating phase in 2D systems (or QSH insulators) can be extended to three dimensions. In a 3D topological insulator, the electronic structure of a material remains gapped in the bulk but on its surface it hosts gapless surface states. These robust gapless surface conducting states are protected by time-reversal symmetry in the Z_2 topological class. In three dimensions, topological insulators are divided into two classes (a) strong topological insulator (STI) and (b) weak topological insulator (WTI).

In a seminal work, Zhang et al. theoretically predicted the first three dimensional STI in Bi_2Se_3 materials class, which hosts a single Dirac cone in the electronic structure of (001) surface. These states are robust and show spin-momentum locking. In three-dimension, there are four \mathbb{Z}_2 invariants $(\nu_0; \nu_1, \nu_2, \nu_3)$ for a time-reversal invariant system. For a STI, ν_0 must be 1 and the rest of the indices may or may not take non-zero values.

Weak topological insulator

If ν_0 is zero, but at least one of the other three indices (ν_1, ν_2, ν_3) becomes 1, then the TR-invariant material belongs to weak topological insulating phase. For a weak topological insulator (WTI), the appearance of the topological surface states depend on surface termination. A WTI consists of stacked layers of 2D topological insulators and topological surface states only appear on its side surfaces [39]. WTIs are very interesting as they exhibit several intriguing quantum phenomena like one dimensional helical modes along dislocation lines [40], weak anti-localization effect [41] and half quantum spin Hall effect [42]. The essential reason why the WTI is considered weak is that its surface modes may be gapped without breaking TR symmetry or closing the bulk gap.

Topological crystalline insulator

Another interesting class of materials are called as topological crystalline insulators (TCI) [11, 12], where the gapless surface states are protected by mirror symmetry. These materials are different from topological insulators (TI) in which the time reversal symmetry protects the surface states and hence the protection of surface states for TCI perseveres even when time-reversal symmetry is broken. The presence of mirror symmetry in the crystal structure of a material results in the presence of planes in the BZ that are mirror symmetric. Therefore, mirror symmetry protected Dirac cones arise in the surface electronic structure. TCIs are characterized by a non-zero mirror Chern number. The individual Chern numbers C_{+i} and C_{-i} are defined on a mirror-invariant plane. The mirror Chern number [11] defined as $n_M = (C_{+i} - C_{-i})/2$ can be used as a topological invariant

for TCI. A TCI supports an even number of Dirac cones and band inversions in sharp contrast to a TI characterized by odd number of band inversions. The first TCI phase experimental [13] observation was made in SnTe, which were earlier theoretically [14] predicted. Soon after its theoretical prediction, TCI phase was experimentally verified in $\text{Pb}_{1-x}\text{Sn}_x\text{Se}$ using ARPES experiments. [43].

1.5 Elements of topological band theory

1.5.1 Bulk-boundary correspondence principle

The bulk-boundary correspondence principle states that at the interface between two materials belonging to same symmetry but different topological classes, topological edge or surface states appear. For example, if n and m are the bulk topological invariants of two materials, then at their interface there will be precisely $|n-m|$ number of edge states [44]. This principle in general holds true for non-interacting fermionic systems [45]. This principle establishes the relation between edge/surface states to topological properties of the bulk wave functions.

1.5.2 Berry curvature and Berry phase

Berry phase (γ) is a phase that may be acquired by an electronic state when the electronic state undergoes a cyclic adiabatic evolution in a closed path in the Brillouin zone. If there are M non-degenerate bands present in a material, then for each band n , Berry's phase is given by $\gamma_n = \oint_c d\mathbf{k} \cdot \mathbf{A}_n(\mathbf{k})$, where $\mathbf{A}_n(\mathbf{k})$ is the Berry connection of the n -th band and is analogous to magnetic vector potential in the reciprocal space. Berry connection is given by $\mathbf{A}_n(\mathbf{k}) = i \langle u_n(\mathbf{k}) | \frac{\partial}{\partial \mathbf{k}} | u_n(\mathbf{k}) \rangle$. Berry curvature is defined as the field associated with the Berry potential $\mathbf{A}_n(\mathbf{k})$ and can be obtained as: $\Omega_n(\mathbf{k}) = \nabla_{\mathbf{k}} \times \mathbf{A}_n(\mathbf{k})$. In the case of non-degenerate bands, Berry curvature is Abelian. But when degeneracy is present within the band manifold of interest, the conventional adiabatic theorem needs to be generalized, and Berry curvature becomes non-Abelian which is represented by a tensor. This extension of

the Berry curvature to the tensor framework was done in analogy with the non-Abelian gauge theories by Wilczek and Zee [46] in 1984. In the case of degenerate bands, the Berry connection is given by, $A_{mn}(\mathbf{k}) = i \langle u_m(\mathbf{k}) | \frac{\partial}{\partial \mathbf{k}} | u_n(\mathbf{k}) \rangle$, where m, n indicate the band indices ($m, n \in \Sigma$) within the degenerate subspace ($\Sigma = 1, \dots, N$). In this case, the non-Abelian Berry curvature is given by [47],

$$\Omega_{mn}(\mathbf{k}) = i \left\langle \frac{\partial u_m(\mathbf{k})}{\partial \mathbf{k}} \middle| \times \middle| \frac{\partial u_n(\mathbf{k})}{\partial \mathbf{k}} \right\rangle + i \sum_{l \in \Sigma} \langle u_m(\mathbf{k}) | \frac{\partial u_l(\mathbf{k})}{\partial \mathbf{k}} \rangle \times \langle u_l(\mathbf{k}) | \frac{\partial u_n(\mathbf{k})}{\partial \mathbf{k}} \rangle \quad (1.7)$$

1.5.3 Chern number

Chern number is a topological invariant quantity which is obtained as an integration of the Berry curvature in a closed surface in the Brillouin zone. Using the definition of Berry curvature for the non-degenerate case above, the Chern number for the n -th band is given by,

$$C_n = \frac{1}{2\pi} \int \Omega_n(\mathbf{k}) d^2k, \quad (1.8)$$

where the integration is taken over the two-dimensional Brillouin zone.

1.5.4 Z_2 invariants

The presence of robust edge states in quantum Spin Hall (QSH) insulator or two-dimensional topological insulator suggests that there must exist a topological distinction between quantum spin Hall insulator and ordinary insulator for which there are no topological edge states present. For a time reversal invariant system, Z_2 topological invariants differentiate a QSH phase from an ordinary insulating phase. In two dimensions, there is a single Z_2 invariant ν (which can be either 0 and 1). In three dimensions, there are four Z_2 topological indices ($\nu_0; \nu_1, \nu_2, \nu_3$) [48], where ν_0 is the strong topological index and the rest (ν_1, ν_2, ν_3) are called weak topological indices. According to Fu & Kane, a Z_2 invariant quantity can be described as an obstruction to finding a smooth gauge for the Bloch wavefunction in

the half-Brillouin zone (BZ) and is given by [49, 50],

$$\Delta = \frac{1}{2\pi} \left(\oint_{\partial\tau_{\frac{1}{2}}} \mathbf{a} \cdot d\mathbf{l} - \int \Omega_{xy} d^2k \right) \text{ mod } 2, \quad (1.9)$$

where $\tau_{\frac{1}{2}}$ and $\partial\tau_{\frac{1}{2}}$ denote half-BZ and its boundary respectively. $a_j = i \sum_n \langle u_n(\mathbf{k}) | \frac{\partial}{\partial \mathbf{k}_j} | u_n(\mathbf{k}) \rangle$ is the the Berry connection and Ω_{xy} is the Berry curvature.

For a centrosymmetric material, the Z_2 topological invariants can be computed straightforwardly using the parity of the wave functions of the occupied bands at the time-reversal invariant momenta (TRIM) in the Brillouin zone [48]. In three dimensions, there are eight TRIM which form a parallelepiped in the BZ, which are given by $\Gamma_i = \frac{1}{2}(n_1 \mathbf{b}_1 + n_2 \mathbf{b}_2 + n_3 \mathbf{b}_3)$, where $\mathbf{b}_1, \mathbf{b}_2, \mathbf{b}_3$ are primitive reciprocal lattice vectors and n_1, n_2, n_3 can take values of 1 and 0. In this method, the strong topological index is given by, $(-1)^{\nu_0} = \prod_{i=1}^8 \sigma_i$, where $\sigma_i = \prod_m \xi_{2m}^{(i)}$ is the product of parity of the occupied bands at i -th time reversal invariant momentum, and m indicates a band from each doubly degenerate Kramer's pairs. The other three weak topological indices ($\nu_k, k = 1, 2, 3$) are determined based on the parity of the occupied states at four different combinations of TRIM in the BZ which form a surface of the parallelepiped excluding the Γ point (in the $k_x k_y$ -, $k_y k_z$ - and $k_x k_z$ - planes) through the relation [51] $(-1)^{\nu_k} = \prod_{i=1}^4 \sigma_i$.

1.5.5 Mirror Chern Number

The presence of mirror symmetry in the crystal structure of some materials results in the presence of planes in the BZ that are mirror-symmetric. This implies that the Bloch states on these planes are eigenstates of a unitary matrix M which describes the action of mirror symmetry. In the presence and absence of spin-orbit coupling this matrix squares to -1 and 1 respectively. This means that the eigenvalues of M are $\pm i$ for spinor Bloch states on the mirror-symmetric planes. The individual Chern numbers C_{+i} and C_{-i} are then defined for each of these subspaces. The mirror Chern number is defined as $n_M = (C_{+i} - C_{-i})/2$. This number can be used as a Z topological invariant for the systems with TR-symmetry,

where $C_{+i} = -C_{-i}$. To compute the individual Chern numbers C_{+i} and C_{-i} , it is first necessary to classify each Hamiltonian eigenstate according to the mirror eigenvalues $+i$ or $-i$. This is done by computing and diagonalizing at each \mathbf{k} the matrix.

$$\langle \psi_n(\mathbf{k}) | \hat{M} | \psi_m(\mathbf{k}) \rangle \quad (1.10)$$

where M is the mirror operator, for all occupied states $\Psi_j(\mathbf{k})$. Using the unitary transformation $U(\mathbf{k})$ which diagonalizes this matrix, a set of states with definite mirror eigenvalues is constructed as

$$|\tilde{\psi}_m(\mathbf{k})\rangle = \sum_m U_{mn}(\mathbf{k}) |\psi_n(\mathbf{k})\rangle \quad (1.11)$$

These states are then separated into two groups corresponding to the $\pm i$ eigenvalues to compute C [52].

In chapter 5 we study topology of $TlBiS_2$ as a function of pressure. As a consequence of band inversions there are changes in the electronic topology of the system, confirmed with Z_2 and n_M topological invariants calculated at various pressures. Chapter 6 deals with Raman study of pressure induced phase transitions in a topological crystalline insulator SnTe and a normal semiconductor SnSe.

Bibliography

- [1] M. C. Payne, M. P. Teter, D. C. Ailan, T. A. Arias and J. D. Joannopoulos, *Rev. Mod. Phys.* **64**, 1045 (1992).
- [2] J. Ihm, *Rep. Prog. Phys.* **51**, 105 (1988).
- [3] J. Kohanoff, *Electronic Structure Calculations for Solids and Molecules*, Cambridge University Press, Cambridge (2006), ISBN:13-978-0-521-81591-8.
- [4] R. M. Martin, *Electronic Structure, Basic Theory and Practical Methods*, Cambridge University Press, Cambridge (2004), ISBN: 978-0-521-78285-6.
- [5] Fischer W, A second note on the term “Chalcogen”. *J Chem Educ* **78**, 1333 (2001)
- [6] *Transition Metal Sulfides: Chemistry and Catalysis*, eds. T. Weber, R. Prins and R. A. v. Santen, Kluwer Academic Publishers, 1998.
- [7] J. R. Sootsman, D. Y. Chung and M. G. Kanatzidis, *Angew. Chem. Int. Ed.* **48**, 8616 (2009)
- [8] Q. H. Wang, K. Kalantar-Zadeh, A. Kis, J. N. Coleman and M. S. Strano, *Nat Nanotechnol.* **7**, 699 (2012).
- [9] G. Tan, L.-D. Zhao and M. G. Kanatzidis, *Chem. Rev.* **116**, 12123 (2016).
- [10] C. J. Vineis, A. Shakouri, A. Majumdar and M. G. Kanatzidis, *Adv. Mater.* **22**, 3970 (2010).
- [11] A. Rogalski, *Rep. Prog. Phys.* **68**, 2267 (2005).

-
- [12] B. Radisavljevic, A. Radenovic, J. Brivio, V. Giacometti and A. Kis *Nat. Nanotechnol.* **6**, 147 (2011).
- [13] J. J. Cha, J. R. Williams, D. Kong, S. Meister, H. Peng, A. J. Bestwick, P. Gallagher, D. Goldhaber-Gordon and Y. Cui, *Nano Lett.* **10**, 1076 (2010).
- [14] N. Kamaya, K. Homma, Y. Yamakawa, M. Hirayama, R. Kanno, M. Yonemura, T. Kamiyama, Y. Kato, S. Hama, K. Kawamoto and A. Mitsui, *Nat. Mater.* **10**, 682 (2011).
- [15] F. Cheng, J. Liang, Z. Tao and J. Chen, *Adv. Mater.* **23**, 1695 (2011).
- [16] D. Merki and X. Hu, *Energy Environ. Sci.* **4**, 3878 (2011).
- [17] M. König, S. Wiedmann, C. Brüne, A. Roth, H. Buhmann, L. W. Molenkamp, X.-L. Qi and S.C. Zhang, *Science* **318**, 766 (2007).
- [18] D. Hsieh, Y. Xia, D. Qian, L. Wray, J. H. Dil, F. Meier, J. Osterwalder, L. Patthey, J. G. Checkelsky, N. P. Ong, A. V. Fedorov, H. Lin, A. Bansil, D. Grauer, Y. S. Hor, R. J. Cava and M. Z. Hasan, *Nature* **460**, 1101 (2009).
- [19] Biswas, K., He, J., Blum, I. D., Wu, C. I., Hogan, T. P., Seidman, D. N., Drazid, V. P., Kanatzidis, M. G. *Nature* **489**, 414 (2012).
- [20] Snyder, G. J., Toberer, E. S. *Nat. Mater.* **7**, 105 (2008).
- [21] Rowe, D. M. (ed.) *CRC Handbook of & Thermoelectrics* (CRC, Boca Raton) 1995.
- [22] Sootsman, J., Chung, D. Y., Kanatzidis, M. G. *Angew. Chem. Int. Ed.* **48**, 8616 (2009).
- [23] Seebeck, A. *Ann. Chim. Phys.* **56**, 133 (1826).
- [24] Tritt, T. M.; Subramanian, M. A. *Mater. Res. Soc. Bull.* **31**, 188 (2006).

-
- [25] (a) Altenkirsch, E. E. Phys. Z. **10**, 560 (1909). (b) Altenkirsch, E. E. Phys. Z. **12**, 920 (1911).
- [26] K. v. Klitzing, G. Dorda, and M. Pepper, Phys. Rev. Lett. **45**, 494 (1980).
- [27] F. D. M. Haldane, Phys. Rev. Lett. **61**, 2015 (1988).
- [28] B. A. Bernevig, T. L. Hughes and S. C. Zhang, Science **314**, 1757 (2006).
- [29] D. Thouless, M. Kohmoto, M. Nightingale, and M. Den Nijs, Physical Review Letters **49**, 405 (1982).
- [30] F. Haldane, Physical Review Letters **50**, 1153 (1983).
- [31] Q. Niu, D. J. Thouless, and Y.-S. Wu, Physical Review B **31**, 3372 (1985).
- [32] D. R. Nelson and J. Kosterlitz, Physical Review Letters **39**, 1201 (1977).
- [33] F. Pollmann and A. M. Turner, Physical Review B **86**, 125441 (2012).
- [34] K. v. Klitzing, G. Dorda, and M. Pepper, Phys. Rev. Lett. **45**, 494 (1980).
- [35] C. L. Kane and E. J. Mele, Phys. Rev. Lett. **95**, 226801 (2005).
- [36] D. J. Thouless, M. Kohmoto, M. P. Nightingale, and M. den Nijs, Phys. Rev. Lett. **49**, 405 (1982).
- [37] C. L. Kane and E. J. Mele, Phys. Rev. Lett. **95**, 146802 (2005).
- [38] M. König et al., Science **318**, 766 (2007).
- [39] Z. Ringel, Y. E. Kraus, and A. Stern, Physical Review B **86**, 045102 (2012).
- [40] Y. Ran, Y. Zhang, and A. Vishwanath, Nature Physics **5**, 298 (2009).
- [41] R. S. Mong, J. H. Bardarson, and J. E. Moore, Physical Review Letters **108**, 076804 (2012).

-
- [42] C. X. Liu, X. L. Qi, and S. C. Zhang, *Physica E: Low-dimensional Systems and Nanostructures* **44**, 906 (2012).
- [43] P. Dziawa et al., *Nature Materials* **11**, 1023 (2012).
- [44] M. Franz and L. Molenkamp, *Topological Insulators* (Elsevier, Amsterdam, 2013), Vol. 6.
- [45] B. A. Bernevig and T. L. Hughes, *Topological insulators and topological superconductors* (Princeton University Press, Princeton and Oxford, 2013).
- [46] F. Wilczek and A. Zee, *Phys. Rev. Lett.* **52**, 2111 (1984).
- [47] M. Gradhand et al., *Journal of Physics: Condensed Matter* **24**, 213202 (2012).
- [48] L. Fu, C. L. Kane, and E. J. Mele, *Physical Review Letters* **98**, 106803 (2007).
- [49] L. Fu and C. L. Kane, *Phys. Rev. B* **74**, 195312 (2006).
- [50] R. Yu et al., *Physical Review B* **84**, 075119 (2011).
- [51] B. Yan, L. M^uchler, and C. Felser, *Physical Review Letters* **109**, 116406 (2012).
- [52] Dominik Gresch, Gabriel Autès, Oleg V. Yazyev, Matthias Troyer, David Vanderbilt, B. Andrei Bernevig, and Alexey A. Soluyanov, *Phys. Rev. B* **95**, 075146 (2017)
- [53] F. Bloch, *Z. Phys.* **52**, 555 (1928).
- [54] A. H. Wilson, *Proc. Roy. Soc. A* **133**, 458 (1931).
- [55] A. H. Wilson, *Proc. Roy. Soc. A* **134**, 277 (1931).
- [56] W. Kohn, *Phys. Rev. A* **171**, 133 (1964).
- [57] R. Resta, *Ferroelectrics* **51**, 136 (1992).
- [58] R. D. King-Smith and D. Vanderbilt, *Phys. Rev. B* **47**, 1651 (1993).

Chapter 2

Methods and Formalism

The aim of this chapter is to briefly discuss the theoretical background and the computational methods involved in our first-principles calculations within the framework of density functional theory. The ability of quantum mechanics to predict the total energy of a system of electrons and nuclei has been the driving force to perform quantum-mechanical calculations.

In first section we show how any property exhibited by a material can be described by the total quantum mechanical Hamiltonian involving the interaction between the electrons, the ions and the interaction among themselves. We then describe certain approximations e.g., Born-Oppenheimer and classical nuclei approximations considered while calculating the electronic structure of a material. Next section involves converting these many body Schrödinger equation to a set of coupled one electron equations using Hohenberg-Kohn theorems and Kohn-Sham Ansatz. The Kohn-Sham hamiltonian can then be practically solved to obtain the total energy of system of electrons and nuclei which is the essential quantity needed to calculate many physical quantities. The first order derivatives of total energy give important physical quantities like polarization, magnetization and forces while dielectric constant, magnetic susceptibility, force constant can be obtained by taking the second order derivatives of the total energy.

The next section involves discussing the theoretical approaches within the adiabatic

density functional perturbation theory (DFPT) used to describe phonons which are essentially quanta of lattice vibrations in a material.

In the last section, we describe how maximally localized Wannier function (MLWF) can be used efficiently to calculate Berry phase, Berry curvature, Chern number of a material. We review how various topological invariants can be obtained using MLWF and employing the idea of time reversal polarization.

2.1 Basic equations for interacting electrons and nuclei

The full Hamiltonian of a material taking into account all possible interactions between electrons and ions is given in Eq.(2.1) as,

$$\begin{aligned} \mathcal{H} = & - \sum_I \frac{\hbar^2}{2M_I} \nabla_I^2 - \sum_i \frac{\hbar^2}{2m} \nabla_i^2 + \frac{e^2}{2} \sum_I \sum_{J \neq I} \frac{Z_I Z_J}{|\mathbf{R}_I - \mathbf{R}_J|} \\ & + \frac{e^2}{2} \sum_i \sum_{j \neq i} \frac{1}{|\mathbf{r}_i - \mathbf{r}_j|} - e^2 \sum_{I=1} \sum_{i=1} \frac{Z_I}{|\mathbf{R}_I - \mathbf{r}_i|} \end{aligned} \quad (2.1)$$

Here, electrons are denoted by lowercase subscripts and nuclei by uppercase subscripts. The first term in the above expression is the kinetic energy of nuclei, the second term represents the kinetic energy of electrons, the third and fourth terms represent the interaction between electrons and the interaction between nuclei respectively. Fifth term also termed as external potential denotes interaction between electrons and nuclei.

Given this total Hamiltonian of any system, we can write the time-independent Schrödinger equation as,

$$\mathcal{H}\Xi(\mathbf{R}_I, \mathbf{r}_i) = E\Xi(\mathbf{R}_I, \mathbf{r}_i), \quad (2.2)$$

where $\Xi(\mathbf{R}_I, \mathbf{r}_i)$ is the total wave function consisting of electronic and ionic part.

If total energies can be calculated, any physical property that can be related to total

energy can be determined computationally. The problem in obtaining exact quantum mechanical total energy is to solve a set of very complicated coupled differential equation. This is because any material has a very large number of ions and electrons with their degrees of freedom coupled to each other. The only possible solution is taking into account reasonably good approximations.

2.1.1 Adiabatic Born-Oppenheimer Approximation

The adiabatic approximation (*Born-Oppenheimer* approximation [1]) is the first and the most important assumption made to simplify the grand hamiltonian of a system of interacting electrons and ions. This assumption is based on the fact that the mass of the nucleus is approximately 1836 times larger than that of an electron hence the time scale associated with the motion of the nuclei (ions) are much slower than that associated with electrons. Therefore, kinetic energy of nuclei can be neglected in comparison to that of electrons. The electrons instantaneously follow the motion of the ions while remaining in the same stationary (adiabatic) state (ground or excited). If this condition is followed then the dynamics is said to be adiabatic.

\mathcal{H} is the total Hamiltonian of the system

$$\mathcal{H} = T_n + V(\mathbf{R}_I) + H_e \quad (2.3)$$

where the electronic Hamiltonian of a system can be written in a short notation as,

$$H_e = T_e + U_{ee} + u(\mathbf{r}_i, \mathbf{R}_I), \quad (2.4)$$

where T_e , T_n are the kinetic energies of electrons and nuclei respectively. $U_{ee}(= \sum_{i \neq j} \frac{e^2}{|\mathbf{r}_i - \mathbf{r}_j|})$ and $V(\mathbf{R}_I)$ are electron-electron and nuclear-nuclear interaction potential respectively. $u(\mathbf{r}_i, \mathbf{R}_I)$ is the interaction potential between the electrons and nuclei.

2.1.2 Classical nuclei approximation

The second most important assumption made in simplifying the electronic structure of a matter is the classical nuclei approximation. Since the nuclear masses are very heavy as compared to electrons, the wave functions for nuclei are much more localized and therefore one can assume that quantum phase coherence of the nuclear wave functions is very less or does not exist at all. This led to the safe assumption of treating nuclei as classical particles. Within this approximation, the total nuclear wave function can be expressed as the product of all individual nuclear wave function. By doing so we can neglect the exchange and correlation interactions among them.

The dynamics of the mean values of position and momentum operators can be obtained through Ehrenfest's theorem.

2.1.3 Independent electron approximation

Independent electron approximation is the oldest approximation which considers two basic independent-particle approaches that may be classified into "non-interacting" or *Hartree* method and *Hartree-Fock* method. In *Hartree* method, only the classical electrostatic Coulomb interaction energy is taken into account while neglecting the exchange and correlation effect. Hartree did not consider the asymmetric nature of electronic wavefunctions. But in *Hartree-Fock* method, in addition to the electrostatic interaction energy, the exchange effect due to Pauli principle and correlation effect are taken into account. Antisymmetric nature of electrons was considered in the Hartree-Fock Approximation. In this framework, asymmetric electronic wavefunction can be written in the form of a Slater determinant such that the wavefunctions are indistinguishable.

In modern DFT, the electronic Hamiltonian is taken to be non-interacting like in *Hartree* approach and electrons are assumed to move in an effective external potential chosen so as to incorporate the exchange-correlation effect approximately.

2.2 Density functional theory

In literature there exist many methods for calculating the electronic structure of a system. The existing most popular ones include density functional theory preferred by physicists and approaches like *Hartree-Fock* method which is mostly favored by the chemists owing to its many computational advantages. Density functional theory is an approach which treats the ground state of many body system accurately and at the same time is efficient to apply. It reduces the complexity of many electron problem to a great extent by converting function of $3N$ -variables (N is the number of electrons and to each N , 3 spatial variables are associated) associated with many electron-wave functions with a functional of electron density which is a function of only 3 spatial variables. The main idea of density functional theory is that it casts the interacting many-body problem into single particle problem via the particle density with the many-body effects included in the exchange-correlation functional. It is based on two powerful theorems given by Hohenberg & Kohn [4] and Kohn & Sham [5] which will be described in the subsequent sections.

The concept of the full electronic density being a fundamental variable in many body problems rather than the many-body wave function lead to the development of density functional theory. The pioneers of this concept were L. H. Thomas, E. Fermi and Hartree at about the same time. This approximation is known as *Thomas-Fermi* approximation.

2.2.1 Thomas-Fermi theory

The Thomas-Fermi theory provides a functional form for the kinetic energy of a non-interacting electron gas in some known external potential $V(r)$ (usually due to impurities) as a function of the density. It is a local density functional and is based on a semiclassical approximation. The formulation becomes exact for a uniform electron gas.

For an interacting system, if the form of the interaction potential is known as a function of the ground state density, such as in the density functional theory, one can also add this contribution to the external potential $V(r)$, and solve the non-linear equations, now with

an effective potential $V_{eff} = V + V_H + V_{xc}$. Here, the newly added terms are respectively the Coulomb interaction (Hartree potential) and the exchange-correlation potential seen by an electron.

Thomas and Fermi constructed the total electronic energy of an inhomogeneous system as a functional of electron density ρ as given below,

$$E_\alpha[\rho] = \int \rho(\mathbf{r})\epsilon_\alpha[\rho(\mathbf{r})]d\mathbf{r}, \quad (2.5)$$

where $\epsilon_\alpha[\rho(\mathbf{r})]$ is the energy density which consists of the contributions (α) from kinetic, exchange and correlation energy of a homogeneous electron gas for which good approximations already exist. This energy density is calculated locally at every point and integrated over whole space. The above expression is called a functional which depends on some function (here it is the electron density $\rho(\mathbf{r})$).

2.2.2 Hohenberg-Kohn theorem

The Hamiltonian of any interacting system whose particles are assumed to move in an external potential $V_{ext}(\mathbf{r})$ can be written as,

$$H_e = T_e + V_{ext}(\mathbf{r}) + U_{ee}(\mathbf{r}) \quad (2.6)$$

The formulation of DFT applies to such Hamiltonians. The modern density functional theory is based upon two powerful theorems given by Hohenberg & Kohn [4] who formulated DFT as an exact many-body theory of a many-body system. Their theorems can be stated as follows:

First Hohenberg-Kohn theorem - For any system of interacting particles in an external potential $V_{ext}(\mathbf{r})$, the potential $V_{ext}(\mathbf{r})$ is uniquely determined by the ground state electronic density $\rho_0(\mathbf{r})$ of the system within the ambiguity of an additive constant.

Second Hohenberg-Kohn theorem - A universal functional of energy $E[\rho]$ can be defined corresponding to any external potential $V_{ext}(\mathbf{r})$. The ground state energy of a system

is the global minimum of this functional. The electronic density $\rho(\mathbf{r})$ which minimizes the functional is called ground state density $\rho_0(\mathbf{r})$ of the system.

The total energy functional, as uniquely determined by $n(\mathbf{r})$, is

$$E_{HK}[n] = T[n] + \int d^3r V_{ext}(\mathbf{r})n(\mathbf{r}) + E_{int}[n] + E_{II} \quad (2.7)$$

where E_{II} denotes the energy of electrostatic interaction of nuclei.

A functional $F_{HK}[n]$, which includes kinetic and potential energies of interacting electron system, can be defined as:

$$F_{HK}[n] = T[n] + E_{int}[n] \quad (2.8)$$

Thus, if the functional $F_{HK}[n]$ is known, minimization of total energy with respect to $n(\mathbf{r})$ can be used to determine, the exact ground state density and energy.

These Hohenberg and Kohn theorems make a significant contribution towards calculation of ground state energy by reducing it to the minimization problem with function of $3N_e$ to that of 3 variables. The difficulty with the above formulation is that there is no direct way to extract kinetic energy from the density. This implies that the exact functional varies in a non-analytic manner as a function of number of electrons. This lead to Kohn and Sham approach, where kinetic energy is treated in terms of single particle wavefunctions and interaction terms as functionals of the density.

2.2.3 Kohn-Sham approach

The central theme of Kohn-Sham approach to density functional theory involves assuming a system of non-interacting electrons in an external potential. In their approach, the unknown Hohenberg-Kohn functional is nothing but the kinetic energy of the electrons. The idea of Kohn-Sham [5] was that if one can find any non-interacting electronic system that produces the same electronic density as that of the interacting system, then the kinetic energy of the electrons can be calculated through one electron orbitals. Though the kinetic energy calculated in this way will not be exactly same as that of the kinetic

energy obtained from a many-body wave function. The missing fraction is due to the *correlation* among the electrons which can be approximately included in the exchange-correlation functional.

Using the Kohn-Sham approach the energy functional can now be written as:

$$E[n(\mathbf{r})] = T_s[n(\mathbf{r})] + \frac{1}{2} \int \frac{n(\mathbf{r})n(\mathbf{r}') d^3r d^3r'}{|\mathbf{r} - \mathbf{r}'|} + \int n(\mathbf{r})V_{ext}(\mathbf{r})d\mathbf{r} + E_{xc}[n(\mathbf{r})] \quad (2.9)$$

The first term is the kinetic energy of electrons, the second term is the electrostatic interaction energy between electrons, the third term is the interaction energy of electrons with external potential and the fourth term is the exchange-correlation interaction between electrons.

The electron density is constructed using single-particle states and is expressed as,

$$n(\mathbf{r}) = \sum_i |\Psi_i(\mathbf{r})|^2 \quad (2.10)$$

where the summation is over all occupied states.

The Kohn-Sham non-interacting single particle Hamiltonian is,

$$H_{KS} = T_s[n] + V_{KS}(\mathbf{r}) \quad (2.11)$$

where V_{KS} is Kohn-Sham potential which is defined as,

$$V = V_{ext}(r) + V_{Hartree}(r) + V_{XC}(\mathbf{r}) \quad (2.12)$$

where V_{ext} , $V_{Hartree}$ and V_{XC} are external, Hartree and exchange-correlation potentials respectively.

The exchange-correlation potential defined as:

$$V_{xc}[n(\mathbf{r})] = \frac{\delta E_{xc}[n(\mathbf{r})]}{\delta n(\mathbf{r})} \quad (2.13)$$

The single particle Kohn-Sham equations are,

$$\left(-\frac{\hbar^2}{2m}\nabla_I^2 + V_{KS}(\mathbf{r})\right)\Psi_i(\mathbf{r}) = \varepsilon_i\Psi_i(\mathbf{r}) \quad (2.14)$$

Since Kohn-Sham equations are non-linear equations (Eq. 2.11), a self-consistent iterative method is used to solve them as illustrated in Figure 2.1.

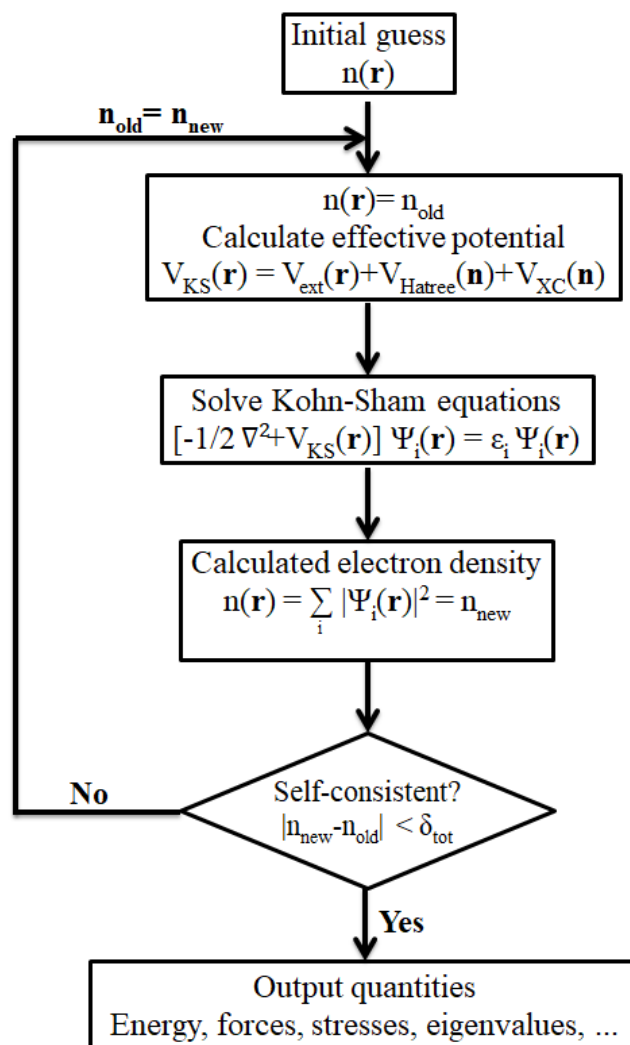


Figure 2.1: Flow chart showing the self-consistency loop for the iterative solution of Kohn-Sham equations.

2.2.4 Basis Set

In order to numerically solve the Kohn Sham equations one requires to choose a mathematical representation for the one electron orbital. The requirement is a basis to expand the wave functions Ψ_n , and then truncating the basis such that the calculation time remains finite. Different classification of basis sets include plane-waves, atomic orbitals and mixed which is a set of atom centred basis along with plane waves or other basis sets. The atomic orbital basis is the most commonly used basis set for isolated systems such as atoms and molecules. A basis set of mutually orthonormal basis is used for representation of extended periodic systems.

The electronic wave functions are expanded in terms of plane-wave basis set which are often very large. Considering the infinite system as a repeating array of unit cells allow us to expand the finite number of electronic wave functions. The potential experienced by an electron is invariant under crystal lattice translation i.e, $V_{ext}(\mathbf{r}) = V_{ext}(\mathbf{r}+\mathbf{R})$ where, \mathbf{R} is a lattice vector. Bloch's theorem states that in periodic solid each electronic wave functions has two parts and can be written as the product of these i.e. a cell-periodic part and a wavelike part:

$$\psi_{jk}(\mathbf{r}) = u_{jk}(\mathbf{r})e^{i\mathbf{k}\cdot\mathbf{r}} \quad (2.15)$$

Here, u_{jk} is a cell periodic part, and an exponential term is a plane wave. The cellperiodic part can be expanded in terms of a discrete set of plane waves whose wave vectors are reciprocal lattice vectors (\mathbf{G}) of the crystal.

$$u_{jk} = \frac{1}{\sqrt{V}} \sum_{\mathbf{G}} C_{jk}(\mathbf{G})e^{i\mathbf{G}\cdot\mathbf{r}} \quad (2.16)$$

Therefore, each electronic Bloch wave function can be written as a sum of plane waves,

$$\psi_{jk} = \frac{1}{\sqrt{V}} \sum_{\mathbf{G}} C_{j,k+\mathbf{G}} e^{i(\mathbf{k}+\mathbf{G})\cdot\mathbf{r}} \quad (2.17)$$

The kinetic energy of plane waves is given by the following relations:

$$T_{|k+G|} = \frac{\hbar^2 |\mathbf{k} + \mathbf{G}|^2}{2m} \quad (2.18)$$

For low energy states plane waves basis with smaller kinetic energy are more relevant. Hence, plane waves are truncated by using an energy cutoff parameter E_{cut} . The advantage of the plane wave basis is that they represent all region of space with the same resolution and are independent of atomic positions. The calculation of energy and its derivative is analytic and simple and the quality of the basis can be controlled by a single parameter. The main disadvantage of the plane wave basis being the rapid oscillations of the valence wavefunctions in the region occupied by the core electrons. This is due to the strong ionic potential in this region and hence demands a large basis set, making it computationally expensive.

2.2.5 Approximation to exchange & correlation energy

All the many-body effects in kinetic, exchange and correlation are grouped into the exchange-correlation energy E_{XC} . The exchange-correlation energy functional Kohn Sham approach can be defined as:

$$E_{xc}[n(\mathbf{r})] = T[n(\mathbf{r})] - T_o[n(\mathbf{r})] + E_{ee}[\mathbf{r}] - E_H[n(\mathbf{r})] \quad (2.19)$$

The spatial separation between the electrons that have the same spin leads to a reduction in the Coulomb energy of the electronic system. The reduction in energy due to anti-symmetric nature of wavefunction is called the exchange energy, this is generally referred to as the Hartree-Fock approximation. Coulomb energy of the system is also reduced at the cost of an increase in kinetic energy when the electrons of the same spin are spatially separated. The difference between the many body energy of an electronic system and that calculated in the Hartree-Fock approximation is called the correlation energy. It is quite difficult to determine the exact value of exchange-correlation functional due to

electron-electron interactions involved. Kohn Sham replaces many electron problem by single electron equation.

Here, $T_o[n(r)]$ and $E_{ee}[(r)]$ are exact kinetic and electron-electron interaction energies respectively. Since, exact value of E_{xc} is not known; so various approximations based on electron density have been introduced to describe it.

Local density approximation (LDA) and Generalized Gradient Approximations (GGA)

One of the main difficulties in density functional theory is to formulate a correct exchange-correlation functional. Among all the existing functionals the most popular and widely used are local density approximation (LDA) and generalized gradient approximation (GGA).

In LDA, the effect of exchange and correlation are considered to be local in nature as it was assumed by Kohn & Sham [5]. In this approach, the inhomogeneous system is thought to be locally homogeneous. The exchange-correlation energy can be obtained by integrating the exchange-correlation energy density at each point over whole space. The LDA approximation proves to be very successful for many systems especially for those whose electron density is quite uniform such as bulk metals, ionic crystals etc. LDA fails to produce some properties (e.g. band gap) in semiconductors, strongly correlated systems due to fact that the excitation spectrum of homogeneous electron gas is gap-less and exchange-correlation energy is regular [8]. Another failure is its ability to capture weak inter-molecular bonds, hydrogen bonds etc.

The exchange-correlation energy in LDA is thus given by,

$$E_{xc}^{LDA}[\rho] = \int d^3\mathbf{r} \rho(\mathbf{r}) \epsilon_{xc}^{homo}[\rho(\mathbf{r})] \quad (2.20)$$

In LDA several aspects like inhomogeneity of electrons, non-local exchange correlation effect, complete cancellation of self-energies of electrons were not present. The improvement of LDA resulted in the development of GGA. In general the exchange-correlation energy in GGA can be written as [9],

$$E_{xc}^{GGA}[n(\mathbf{r})] = \int d^3r \varepsilon_{xc}(n(\mathbf{r}), \nabla \mathbf{n}) n(\mathbf{r}) \quad (2.21)$$

Here, the exchange-correlation energy is expressed as a sum of contributions from each point in real-space depending only on the density and its gradient at each point and independent of other points. The GGA method turns out to be better than LDA in the sense that it improves binding energies, bond lengths. GGA also improves the band gap of semiconductors over LDA. Semiconductors are also better described in GGA than LDA.

The Perdew-Zunger (PZ), Perdew-Wang (PW), and Vosko-Wilk-Nusair (VWN) functionals are the LDA functionals used commonly in calculations, which interpolate between exact results available at high and low densities n . Perdew and Wang (PW91) and Perdew, Burke and Ernzerhof (PBE) are some of the functional within GGA.

2.2.6 Pseudopotentials

Another approximation in our DFT calculations is that of pseudopotentials. In solids or molecules, the core electrons are tightly bound to the nucleus and hence are not involved in bonding. The core electrons are relatively unaffected by the chemical environment of an atom. The contribution of core electrons to the total binding energy remains unaffected when isolated atoms are brought together to form a molecule or a crystal. The actual energy differences of interest involve changes in the valence electron interaction and energies. The contribution of valence electrons to the total binding energy is a much larger fraction than that of valence electrons, and makes it easier to calculate accurately. The reason is the difficulty in numerical representation of highly localized core electron wave-functions

because of strong nuclear Coulomb potential. So, core electrons are removed from the cal-

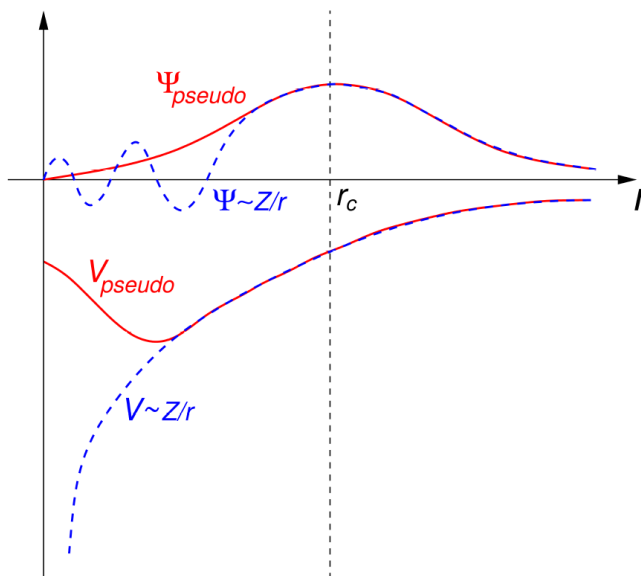


Figure 2.2: *Schematic representation of all-electron (dashed lines) and pseudoelectron (solid lines) potentials and their corresponding wavefunctions. The radius at which all electron and pseudoelectron value matches is designated r_c . This figure is taken from <https://en.wikipedia.org/wiki/Pseudopotential>.*

ulation, and the interaction of the valence electrons with the nucleus plus the core states is replaced by an effective screened potential. Pseudopotentials are constructed using a cutoff radius (r_c) which sort of separates out the the valence region from the core region. The region beyond r_c is treated as a valence region and within r_c as the core region. The value of r_c is chosen in such a way that the last node of the all electron wavefunction fall inside it. Pseudopotential and all electron wavefunction are identical outside the cutoff radius. Traditionally, a pseudopotential is divided into local and non-local parts, where the former is long-ranged and the later is typically short-ranged.

In the norm-conserving pseudopotentials, the norm of all electron wavefunction in the core region (0 to r_c) remains conserved. Atoms like 2p, 3d, and 4f have highly localized charge densities in the valence shell as well as in the core. Another alternative to this is the ultrasoft pseudopotential. The ultrasoft pseudopotential reduces the size of the required plane wave basis set, by increasing the value of r_c and generates smoother wavefunction.

2.2.7 Linearized Augmented Plane Wave (LAPW) method

The linearized augmented plane wave (LAPW) method is one of the most accurate methods for performing electronic structure calculations for crystals. It is based on the density functional theory for the treatment of exchange and correlation. Results of all-electron i.e. explicit treatment of core and valence electrons calculations have higher accuracy but at the same time are computationally more expensive than pseudopotential-based (valence electrons only) electronic structure calculations. LAPW method [10] derives its idea from Slater's augmented plane wave (APW) [11, 12] method which includes core electronic states and excludes the necessity of a pseudopotential. In LAPW method to obtain total energies and eigenvalues of the electrons in a solid we use a basis set. This is achieved by dividing the unit cell into non-overlapping spherical regions centered at each atom (marked as I) and the interstitial region (marked as II). Two different types of

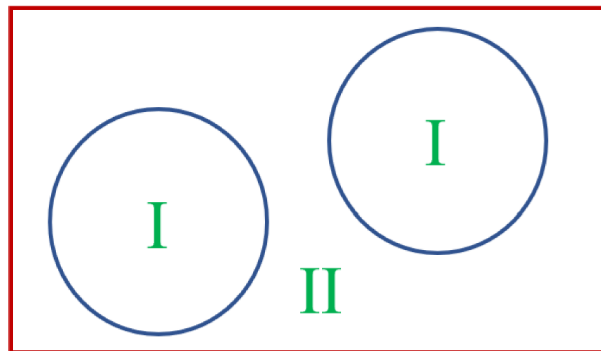


Figure 2.3: *Schematic representation of a LAPW basis set. The unit cell is divided into atom centered region and interstitial region.*

basis sets are used in these two regions: a) Plane wave basis set is used in expansion of the electronic wave functions inside the interstitial region, and b) Atomic like wave functions (linear combination of the solutions of the radial Schrödinger equation and spherical harmonics) in the space inside every atomic sphere. Inside each non-overlapping atomic sphere the atomic-like wave functions form the basis set.

In this formalism the basis function in the interstitial region can be written as:

$$\phi(\mathbf{r}) = \frac{1}{\sqrt{V}} \sum_G C_G e^{i(\mathbf{k}+G)\cdot\mathbf{r}} \quad (2.22)$$

Inside atomic spheres the wave functions can be written as:

$$\phi(\mathbf{r}) = \sum_{lm} (A_{lm} u_{lm}(\mathbf{r}) + B_{lm} u'_l(\mathbf{r})) Y_{lm}(\mathbf{r}) \quad (2.23)$$

The plane wave nature in the interstitial region allows for highly accurate solutions for any atomic arrangement: close-packed or open, highsymmetry or low, surfaces or bulk whereas the atomic-like nature of the LAPW basis in the vicinity of the atoms leads to an efficient representation.

2.3 Phonons

To understand how heat spreads through a material, consider that heat — as well as sound — is actually the motion or vibration of atoms and molecules: Low-frequency vibrations correspond to sound, while higher frequencies correspond to heat. At each frequency, quantum mechanics principles dictate that the vibrational energy must be a multiple of a basic amount of energy, called a quantum, that is proportional to the frequency. Physicists call these basic levels of energy phonons. Phonons are quanta of lattice vibrations in a crystal. In condensed matter physics, properties of a material typically arise from collective excitations. For example, a material consisting of Fermi liquid or an electron gas is used to explain the electrical conductivity of a material. To calculate any property of a material arising from the lattice vibrations, we have to treat the collective oscillations of all the atoms. In a crystal, the atoms are neatly arranged in a uniform, repeating structure; when heated, the atoms can oscillate at specific frequencies. The bonds between the individual atoms in a crystal behave essentially like springs. When one of the atoms gets pushed or pulled, it sets off a wave (or phonon) travelling through

the crystal. In practice, most materials are filled with a chaotic mix of phonons that have different frequencies and are travelling in different directions, all superimposed on each other.

Phonon dispersion of a crystal reveals very interesting physics and insightful dynamical information of a system.

2.3.1 Frozen-phonon approach

Frozen-phonon approach is a computationally inexpensive and practical method to calculate the normal modes of lattice vibrations. This approach involves displacing each atom in the unit cell of the crystal by some value and then calculating the forces on them with the help of density functional theoretical calculation using the *Hellman-Feynman* theorem. The next step involves constructing a force constant matrix by collecting forces from all the atoms and converting it to dynamical matrix with the help of Fourier transformation which, then, can be solved at any \mathbf{q} point in the Brillouin zone to get the phonon frequencies.

One drawback of the frozen-phonon method is that it requires large supercells to calculate the force constant matrix accurately, and hence is computationally expensive. Another very accurate method, based on the linear response theory exists to calculate the frequencies of lattice vibration, is the *density functional perturbation theory* which will be discussed in the next subsection.

2.3.2 Density functional perturbation theory

Within the framework of density functional theory this method involves calculating the second-order change in the DFT total energy (δ^2E). Lattice-dynamical properties of a system have some profound electronic connections. A combination of density functional theory and linear response theory gives rise to what is known as the density functional perturbation theory [17–19]. The perturbation is induced by introducing small displacement $\delta\mathbf{R}$ of ion from its equilibrium positions which results in changes in the external

potential V_{ext} . The external potential induces changes in the KS equation, and hence the charge density. The inter-atomic force constants (IFCs) are obtained using second order derivatives of ground state energy with respect to perturbation, i.e. ionic displacement,

$$K_{IJ} = \frac{\partial^2 E(\{\mathbf{R}\})}{\partial \mathbf{R}_I \partial \mathbf{R}_J} = \int \frac{\partial n(\mathbf{r})}{\partial \mathbf{R}_J} \frac{\partial V_{[R]}(\mathbf{r})}{\partial \mathbf{R}_I} d\mathbf{r} + \delta_{IJ} \int n(\mathbf{r}) \frac{\partial^2 V_{[R]}(\mathbf{r})}{\partial \mathbf{R}_I \partial \mathbf{R}_J} d\mathbf{r} + \frac{\partial^2 E_N(\{\mathbf{R}\})}{\partial \mathbf{R}_I \partial \mathbf{R}_J} \quad (2.24)$$

The IFC depends on ground state charge density and its linear response to displacement of ion. In the perturbation theory, Kohn-Sham equation is given as:

$$\left(H_{SCF}^{(0)} - \epsilon_i^{(0)} \right) |\phi_i^{(1)}\rangle + \left(V_{SCF}^{(1)} - \epsilon_i^{(1)} \right) |\phi_i^{(0)}\rangle = 0 \quad (2.25)$$

Here, $H_{SCF}^{(0)}$ is unperturbed Kohn-Sham Hamiltonian. $\epsilon_i^{(0)}$ and $\phi_i^{(0)}$ are the eigenvalues and eigenvectors of this Hamiltonian. The self-consistent Kohn-Sham effective potential is given at first order by:

$$V_{SCF}^{(1)}(\mathbf{r}) = V_{ext}^{(1)}(\mathbf{r}) + e^2 \int \frac{n^{(1)}(\mathbf{r}') d\mathbf{r}'}{|\mathbf{r} - \mathbf{r}'|} + \int d\mathbf{r}' \left. \frac{dV_{XC}(\mathbf{r})}{dn(\mathbf{r}')} \right|_{n^{(0)}(\mathbf{r})} n^{(1)}(\mathbf{r}') \quad (2.26)$$

By solving the above equations, the change in charge density can be evaluated using:

$$\frac{\partial n(\mathbf{r})}{\partial \mathbf{R}_I} = 4Re \sum_{n=1}^{N/2} \psi_n^*(\mathbf{r}) \frac{\partial \psi_n(\mathbf{r})}{\partial \mathbf{R}_I} \quad (2.27)$$

Δn is used to evaluate the second derivative of total energy.

2.4 Wannier functions in electronic structure calculation

The unitary transformation of the extended Bloch functions to a localized basis set [20–22] leads to the construction of Wannier function (WF). From an isolated set of J Bloch bands (eigenstates of a Hamiltonian), it is always possible to find another set J bands though a

unitary transformation. This set might not be the Hamiltonian eigenstate but can span the same Hilbert space. Thus, one trades off localization in energy for localization in space. Although the concept of Wannier function is prevalent in solid state theory for a long time, practical calculations involving WFs were rarely performed due to the phase indeterminacy of the Bloch function ($\psi_{n\mathbf{k}}$) at each wave vector, which restricts carrying out arbitrary unitary transformation to a set of occupied Bloch function and presence of degeneracy in the electronic band structure at certain high symmetric points in the Brillouin zone (BZ) making it difficult to separate the bands and applying wannierization. Hence, the important condition before computing WFs being choosing a correct set of bands in a given material.

WFs can provide better insight into the nature of chemical bonding which is otherwise missing from the calculations based on an extended basis set and using WF basis, accurate model Hamiltonian can be constructed. Thus, WFs have become an established tool to post-processing electronic structure calculation based on modern state-of-the-art density functional theory. One of the most crucial developments came in 1997 from the works of Marzari and Vanaderbilt [23], who introduced a "maximal localization" criterion for identifying a unique set of WFs in a given crystalline insulating material. For metals in which some of the bands have partial occupations the procedure of the maximal localization was later extended. Importantly, the evolution of the charge centres of the WFs are formally linked to the Berry phase of the Bloch function [24,25] and more recently it has gained significant attention in the research of topological physics as Berry curvature, Chern number, and topological invariants [26] can be computed easily in the framework of maximally localized Wannier function (MLWF).

The WF in the R -th unit cell and corresponding to n -th band is given by the following expression,

$$|\mathbf{R}n\rangle = \frac{V}{(2\pi)^3} \int d\mathbf{k} e^{-\mathbf{k}\cdot\mathbf{R}} |\psi_{n\mathbf{k}}\rangle, \quad (2.28)$$

where \mathbf{R} is the real space lattice vector, that has the effect of translating the real space

WF by \mathbf{R} . V is the volume of the unit cell. Here the integration is done over the whole BZ.

Now, we will briefly discuss how to calculate Berry curvature, Chern number and Z_2 topological invariants using MLWFs.

2.4.1 Maximally localized Wannier function (MLWF)

The formula of the Wannier function involves only a single Bloch band, n . In general, we can consider a manifold of J Bloch bands and hence within this manifold, these may cross each other and degeneracies may be present.

In the multi-band case the formula modifies to,

$$|\mathbf{R}n\rangle = \frac{V}{(2\pi)^3} \int d\mathbf{k} e^{-\mathbf{k}\cdot\mathbf{R}} \sum_{m=1}^J U_{nm}^{(\mathbf{k})} |\psi_{m\mathbf{k}}\rangle, \quad (2.29)$$

where $U_{nm}^{(\mathbf{k})}$ is the unitary rotation or gauge transformation that performs an unitary rotation of the original Bloch function which are the eigenstate of the Hamiltonian,

$$|\tilde{\psi}_{n\mathbf{k}}\rangle = \sum_{m=1}^J U_{nm}^{(\mathbf{k})} |\psi_{m\mathbf{k}}\rangle \quad (2.30)$$

In order to restore the smoothness and to get well localized WFs in the real space, we need to cancel out the discontinuity of the Bloch bands using this unitary transformation. This is because in general the eigenstates of a Hamiltonian may not be smooth.

Hence, even if this unitary gauge transformation might not be necessary in the wannierization procedure for cases in which the bands in the manifold do not touch each other within the BZ unitary rotation is necessary to get well localized WFs.

Marzari and Vanderbilt [23] gave a very general and widely used procedure to generate maximally localized Wannier functions by introducing a *localization criterion* and refining the unitary transformation $U_{nm}^{(\mathbf{k})}$ that satisfy the criterion. The localization function defined by them is given by,

$$\Omega = \sum_n [\langle 0n|r^2|0n\rangle - (0n|\mathbf{r}|0n)^2] = \sum_n [\langle r^2\rangle - \mathbf{r}_n^2], \quad (2.31)$$

which measures the sum of the quadratic spreads of the J WFs in the home unit cell. The above expression is cast as function of \mathbf{k} to minimize the functional with respect to $U_{nm}^{(\mathbf{k})}$. The form of finite difference formula given by Marzari and Vanderbilt is,

$$\begin{cases} \mathbf{r}_n = -\frac{1}{N} \sum_{\mathbf{k}, \mathbf{b}} w_b \mathbf{b} \operatorname{Im} \ln M_{nn}^{(\mathbf{k}, \mathbf{b})} \\ \langle r^2 \rangle = \frac{1}{N} \sum_b w_b \left[1 - |M_{nn}^{(\mathbf{k}, \mathbf{b})}|^2 \right] + \left[\operatorname{Im} \ln M_n^{(\mathbf{k}, \mathbf{b})} \right]^2 \end{cases} \quad (2.32)$$

Here, $M_{nn}^{(\mathbf{k}, \mathbf{b})} = \langle u_{m\mathbf{k}} | u_{n, \mathbf{k}+\mathbf{b}} \rangle$ is the overlap matrix element between two neighboring \mathbf{k} points in the mesh of k-points considered for the evaluation of Eq. 2.41. \mathbf{b} is a vector that connects a \mathbf{k} point to one of its neighbors and w_b is an appropriate weight factor that depends on number of points in the shells in the k-mesh and its geometry. N is the number of k-points in the mesh. Thus, procedure of obtaining MLWF gives us the expectation values \mathbf{r}_n and $\langle r^2 \rangle$ (Wannier charge centres) which are the primary ingredients needed to calculate Chern number and Z_2 topological invariants.

2.4.2 Calculation of Z_2 invariants via WCC

Wannier charge centre is the average position of the charge of Wannier function in the home unit cell given by the expression,

$$\mathbf{r}_n = \langle 0n|\mathbf{r}|0n\rangle \quad (2.33)$$

WCCs are only defined modulo a lattice vector due to the ambiguity in choosing the home unit cell. Moreover, when there are multiple bands present in the chosen band manifold individual WCC are not gauge invariant and only the sum of all the WCCs is gauge-invariant modulo a lattice vector.

As unitary transformation (gauge choice) is not unique, the resultant WFs will show change in shape and their localization in real space if different gauge choices are taken

in the wannierization process. A smooth gauge is needed to have an exponentially localized WF. Mathematically it was proven that it is always possible to find a smooth gauge in 1D [21] ensuring the maximal localization of 1D Wannier function. The 1D maximally localized Wannier function satisfies the required gauge criteria needed to define Z_2 topological invariant [26].

In 1D, the WCC charge centre can be written in terms of Berry connection by the following expression,

$$\begin{cases} \bar{x}_n = \frac{i}{2\pi} \int_{-\pi}^{\pi} \langle u_{n\mathbf{k}} | \partial_k | u_{n\mathbf{k}} \rangle \\ = \frac{1}{2\pi} \int_{-\pi}^{\pi} A(\mathbf{k}) \cdot dk, \end{cases} \quad (2.34)$$

where $A(\mathbf{k}) = i \langle u_{n\mathbf{k}} | \partial_k | u_{n\mathbf{k}} \rangle$ is the Berry connection.

Z_2 topological invariants can be defined using the notion of time reversal polarization [26, 27] derived in terms of hybrid Wannier charge centres (WCCs) [41]. In a time-reversal invariant system, electronic bands always come in time-reversed pairs. Then the Z_2 invariant in a time-reversal invariant plane is given by [26],

$$\left(\sum_n [\bar{x}_n^I(T/2) - \bar{x}_n^{II}(T/2)] - \sum_n [\bar{x}_n^I(0) - \bar{x}_n^{II}(0)] \right) \text{ mod } 2, \quad (2.35)$$

where $\bar{x}_n = \frac{i}{2\pi} \int_{-\pi}^{\pi} dk \langle u_{nk} | \frac{\partial}{\partial k} | u_{nk} \rangle$ is the Wannier charge centres calculated at $t=0$ and $t=T/2$ planes which are invariant under time reversal symmetry. T represents the period of a full cyclic adiabatic evolution. In the Brillouin zone of a periodic crystal T is equivalent to a reciprocal lattice vector which defines the periodicity in the reciprocal space.

If the WCCs switch pairs under a cyclic adiabatic evolution the topological invariant of a plane is non-zero. This can be easily tracked by seeing evolution of the mid-point of the largest gap between two adjacent WCCs at any $t \in [0, T/2]$ in the half-cycle. In such a case the largest gap exhibits abrupt jumps in their cyclic evolution [26]. The procedure to calculate the strong topological index (ν_0) involves taking the sum (modulo 2) of the topological invariants calculated at $k_z=0$ and $k_z=0.5$ planes. At each of these

planes, WCCs are calculated along k_x direction, which evolve along the k_y direction and is parametrized with time, t .

Bibliography

- [1] M. Born and J. R. Oppenheimer, *Ann. Physik* **84**, 457 (1927).
- [2] S. Pisana, M. Lazzeri, C. Casiraghi, K. S. Novoselov, A. K. Geim, A. C. Ferrari and F. Mauri, *Nature Materials* **6**, 198 (2007).
- [3] R. P. Feynman, *Phys. Rev.* **56**, 340 (1939).
- [4] P. Hohenberg and W. Kohn, *Phys. Rev.* **136**, 864 (1964).
- [5] W. Kohn and L. J. Sham, *Phys. Rev. A* **140**, 1133 (1965).
- [6] P. A. M. Dirac, *Proc. Cambridge Phil. Soc.* **26**, 376 (1930).
- [7] E. P. Wigner, *Trans. Faraday Soc.* **34**, 678 (1938).
- [8] J. Kohanoff, *Electronic Structure Calculations for Solids and Molecules*, Cambridge University Press, Cambridge (2006), ISBN:13-978-0-521-81591-8.
- [9] R. M. Martin, *Electronic Structure, Basic Theory and Practical Methods*, Cambridge University Press, Cambridge (2004), ISBN: 978-0-521-78285-6.
- [10] O. K. Andersen, *Physical Review B* **12**, 3060 (1975).
- [11] J. C. Slater, *Physical Review* **81**, 385 (1951).
- [12] J. C. Slater, *Phys. Rev. B* **51**, 846 (1937).
- [13] C. Herring, *Phys. Rev.* **57**, 1169 (1940).

-
- [14] J. C. Philips and L. Kleinman, *Phys. Rev.* **116**, 287 (1959).
- [15] D. R. Hamann, M. Schlüter, C. Chiang, *Phys. Rev. Lett.* **43**, 1494 (1979).
- [16] D. Vanderbilt, *Phys. Rev. B* **41**, 7892 (1990).
- [17] R. Pick, M. H. Cohen and R. M. Martin, *Phys. Rev. B* **1**, 910 (1970).
- [18] S. Baroni, P. Giannozzi and A. Testa, *Phys. Rev. Lett.* **58**, 1861 (1987).
- [19] S. Baroni, P. Giannozzi and A. Testa, *Phys. Rev. Lett.* **59**, 2662 (1987).
- [20] G. H. Wannier, *Physical Review* **52**, 191 (1937).
- [21] W. Kohn, *Physical Review* **115**, 809 (1959).
- [22] J. Des Cloizeaux, *Physical Review* **129**, 554 (1963).
- [23] N. Marzari and D. Vanderbilt, *Physical Review B* **56**, 12847 (1997).
- [24] R. King-Smith and D. Vanderbilt, *Physical Review B* **47**, 1651 (1993).
- [25] R. Resta, *Reviews of Modern Physics* **66**, 899 (1994).
- [26] A. A. Soluyanov and D. Vanderbilt, *Physical Review B* **83**, 235401 (2011).
- [27] J. Bhattacharjee and U. V. Waghmare, *Physical Review B* **71**, 045106 (2005).

Chapter 3

Engineering ferroelectric instability to achieve ultralow thermal conductivity and high thermoelectric performance in $\text{Sn}_{1-x}\text{Ge}_x\text{Te}^*$

3.1 Introduction

Innovative design of solid state structures and compositions with low thermal conductivity while maintaining the high electrical transport is the way forward to high performance thermoelectric (TE) materials, which offer an environment friendly solution for recovery of waste heat in the form of electricity [1, 2]. The crux of improving a material's thermoelectric performance involves essentially the optimization of three interdependent material properties: electrical conductivity (σ), Seebeck coefficient (S) and thermal conductivity (κ_{total} = electronic (κ_{el}) + lattice (κ_{lat}) thermal conductivity) which govern the dimensionless thermoelectric figure of merit, $zT = \sigma S^2 T / (\kappa_{lat} + \kappa_{el})$ [3]. The reduction in κ_{lat} by devising an efficient mechanism of scattering heat carrying acoustic phonons is one of

*This work has been published in Energy & Environmental Science **12**, 589 (2019). Reproduced with permission from the Royal Society of Chemistry.

the most effective and widely used avenues for high performance thermoelectrics [4–6]. Innovative material design like broadband phonon scatterings based on extrinsic all-scale hierarchical nano/meso-architectures [5,7] or intrinsic material properties [8], e.g., complex crystal structures [9], part-crystalline part-liquid state [10], bonding asymmetry [11,12], superionic substructure with liquid-like cation disordering [13–15], lone-pair induced bond anharmonicity [16] and anisotropic layered crystal structure [17,18] have been employed in the past to achieve low κ_{lat} . However, in many of these approaches like the introduction of nano/meso-architectures, the reduction in κ_{lat} comes with a steep cost of reduced charge carrier mobility (μ) and electrical conductivity, resulting in a suboptimal power factor (σS^2).

Here, we present a new strategy to significantly reduce the κ_{lat} without degrading power factor (σS^2) by engineering the ferroelectric instability in crystalline solid. A ferroelectric phase transition is typically marked by temperature dependent softening of polar transverse optical (TO) phonons at the center of the Brillouin zone with its energy becoming comparable to that of heat transporting acoustic phonons [19]. This results in a strong acoustic-optical phonon coupling [20,21], and consequently cause significant scattering of acoustic phonons [22], and low κ_{lat} in solids. The same soft polar optical phonons cause divergently large dielectric response near the ferroelectric instability, and hence the screening of the mobile charge carriers from scattering at impurities/defects, enhancing the charge carrier mobility [23,24]. Therefore, a successful deployment of the ferroelectric instability in thermoelectric solid will be an effective approach to achieve low κ_{lat} while retaining the high carrier mobility which is one of the most challenging problem in thermoelectrics.

We demonstrate that engineering of ferroelectric instability can be used to achieve high thermoelectric performance in inorganic solids like tin telluride ($SnTe$). $SnTe$ has recently emerged as an environment friendly alternative to $PbTe$ for mid-temperature thermoelectric power generation [25–32]. The global centrosymmetric room temperature rocksalt structure of $SnTe$, however, has a lattice instability originating from resonant

bonding [33–38] and undergoes a temperature dependent paraelectric to ferroelectric transition with rhombohedral (R-3m) structure below 100 K [39]. Ferroelectricity in its rhombohedral phase originates from relative displacements of the Sn and Te sublattice along [111] direction [39–43]. In the close proximity of the ferroelectric transition, *SnTe* exhibits softening of the zone centre (Γ - point) TO phonon modes^{34,44} and the frequencies of these TO phonons are in fact lower in the cubic phase compared to that of the rhombohedral phase [43]. This ferroelectric instability associated with soft TO phonons in cubic *SnTe*, can be employed to further improve its thermoelectric performance by reducing the κ_{lat} without degrading the electrical transport properties. However, ferroelectric phase transition and softening of TO phonons in *SnTe* occur in a temperature regime of ≤ 100 K, making it impractical for use in thermoelectric power generation.

Here, Prof. Kanishka Biswas’s group [†] performed experiments utilizing the substitution of Ge (0-30 mol) in *SnTe* to strengthen its ferroelectric instability and achieve soft phonon modes in a wide range of momenta around ferroelectric instability near room temperatures. Experiments along with DFT calculations show that this report opens up a new avenue to inhibit thermal conduction while retaining high carrier mobility in crystalline solids by employing local distortion associated with ferroelectric instability.

3.2 Computational Details

We use density functional theoretical (DFT) methods as implemented in QUANTUM ESPRESSO (QE) code [45], taking into account only the valence electrons and replacing the potential of the ionic core with a pseudopotential. We used a generalised gradient approximation (GGA) [46] to the exchange-correlation energy functional as parametrized by Perdew, Burke, and Ernzerhof (PBE) [47]. To describe the interactions between valence electrons and ions we used Projected Augmented-Wave (PAW) potentials. Valence and semi-core electronic states of Sn, Te and Ge were considered through the use of pseudopotentials (in $4d^{10} 5s^2 5p^2$, $4d^{10} 5s^2 5p^4$, and $3d^{10} 4s^2 4p^2$ configurations respectively). *SnTe*

[†]New Chemistry Unit, Jawaharlal Nehru Centre for Advanced Scientific Research, Bangalore-560064

crystallizes in the rocksalt structure belonging to Fm-3m space group, with two atoms in the primitive unit cell and 8 atoms in the conventional cubic unit cell. Pristine and Ge substituted $SnTe$ were simulated using conventional cubic unit cell containing 4 $SnTe$. Electronic wave functions and charge density were represented in plane wave basis sets truncated with cut-off energies of 45 Ry and 400 Ry respectively. The Brillouin Zone (BZ) integrations were sampled on a uniform $20 \times 20 \times 20$ mesh of k-points. The discontinuity in occupation numbers of electronic states was smeared using a Fermi-Dirac distribution function with broadening of $k_B T = 0.003$ Ry. We determined lattice dynamical properties of $SnTe$ and $Sn_{3/4}Ge_{1/4}Te$ in their optimized structures obtained after vc-relaxation at the experimental lattice parameter [48]. The PBE optimized lattice parameters of $SnTe$ (a=b=c=6.37 Å) and $Sn_{0.75}Ge_{0.25}Te$ (a=b=c= 6.28 Å) were considered for further calculations. Dynamical matrices were calculated within the Density Functional Perturbation Theory (DFPT)5 on a $2 \times 2 \times 2$ q-points grid in the Brillouin Zone. We Fourier interpolated these dynamical matrices to obtain the phonon dispersion along high symmetry lines ($\Gamma - X - M - \Gamma - R - X - M - R$) in the Brillouin zone. We estimated the measure of strain phonon coupling (couplings between acoustic and optical phonons) using a finite difference formula of $\partial \omega_0^2(\epsilon) / \partial \epsilon$, having calculated squared phonon frequencies at strained structures. While we included the effect of spin-orbit coupling (SOC) in calculation of electronic structure by using fully relativistic pseudopotentials, we used scalar relativistic pseudopotentials (SOC=0) in DFT-LR calculations of phonons.

3.3 Results and Discussions

At room temperature (T), $SnTe$ is experimentally known to be an efficient thermoelectric with a cubic structure [50]. As the temperature is lowered, $SnTe$ undergoes a ferroelectric phase transition at $T=T_C$, transforming from the cubic to rhombohedral structure through relative displacements of Sn and Te along [111] direction [51, 52]. The soft vibrational modes whose frequency decreases anomalously near T_C govern the dynamics of such a

transition. As σ the restoring force constant of the mode softens, it is called the “soft-mode”.

Here, we investigate the origin of ultra-low thermal conductivity and enhanced ferroelectric T_C observed in Ge substituted $SnTe$. To begin with, we used DFPT calculations to determine the phonon dispersion of $SnTe$ and $Sn_{0.75}Ge_{0.25}Te$ at their theoretical lattice parameter, as shown in Figure 3.1a) and 3.1b) respectively. The optical phonons of $SnTe$ (Fig. 3.1a) exhibit triply degenerate instability at a frequency of $23i\text{ cm}^{-1}$ at Γ point. Ferroelectricity in $SnTe$ is associated with condensation of all the three unstable modes, giving a rhombohedral distortion of the high temperature cubic phase, with off-centring of Sn atoms, seen in the PDF [49] and EXAFS [53] analysis.

The zone centre Γ) optical phonons of $Sn_{3/4}Ge_{1/4}Te$ exhibit much stronger instability at $\omega \sim 91i\text{ cm}^{-1}$ (see Fig. 3.1b). An interesting feature evident in the phonon dispersion of $Sn_{3/4}Ge_{1/4}Te$ (Fig 3.1b) is the presence of unstable modes at all wave vectors except near the R point ($= (\pi/a)(1, 1, 1)$). This is linked through Fourier analysis with the local distortions with chain-like short-range order [54], size of the distorted region $\sim 1/q_C$. The character of the purely displacive phase transition in $SnTe$ (unstable modes only close to the zone centre) thus changes to order-disorder like transition in $Sn_{0.75}Ge_{0.25}Te$.

We now examine the eigen displacements of the unstable phonon modes (those having imaginary frequencies) at the Γ point of $SnTe$ and Ge doped $SnTe$ to access the relative roles of Ge and Sn in the phase transition (see Fig. 3.2a and 3.2b). While the structural instability in $SnTe$ involves displacements of both Sn and Te atoms, Ge displacements completely dominate the instability in $Sn_{0.75}Ge_{0.25}Te$ (see Fig. 3.2b). This signifies the presence of a rattler kind of behaviour in Ge doped $SnTe$, with the dynamical local displacements of Ge atoms along the chains of Ge – Te - Sn – Te – Ge – Te. Significantly stronger instability results in higher T_C observed in the Ge substituted $SnTe$ than in $SnTe$. The off-centred site is favored energetically due to the large ionic size difference between Sn^{+2} and Ge^{2+} (Ge^{2+} :0.87 Å; Sn^{+2} :0.93 Å), higher polarization power of Ge^{2+} as compared to Sn^{+2} arising from stronger stereochemical activity of ns^2 lone pair in

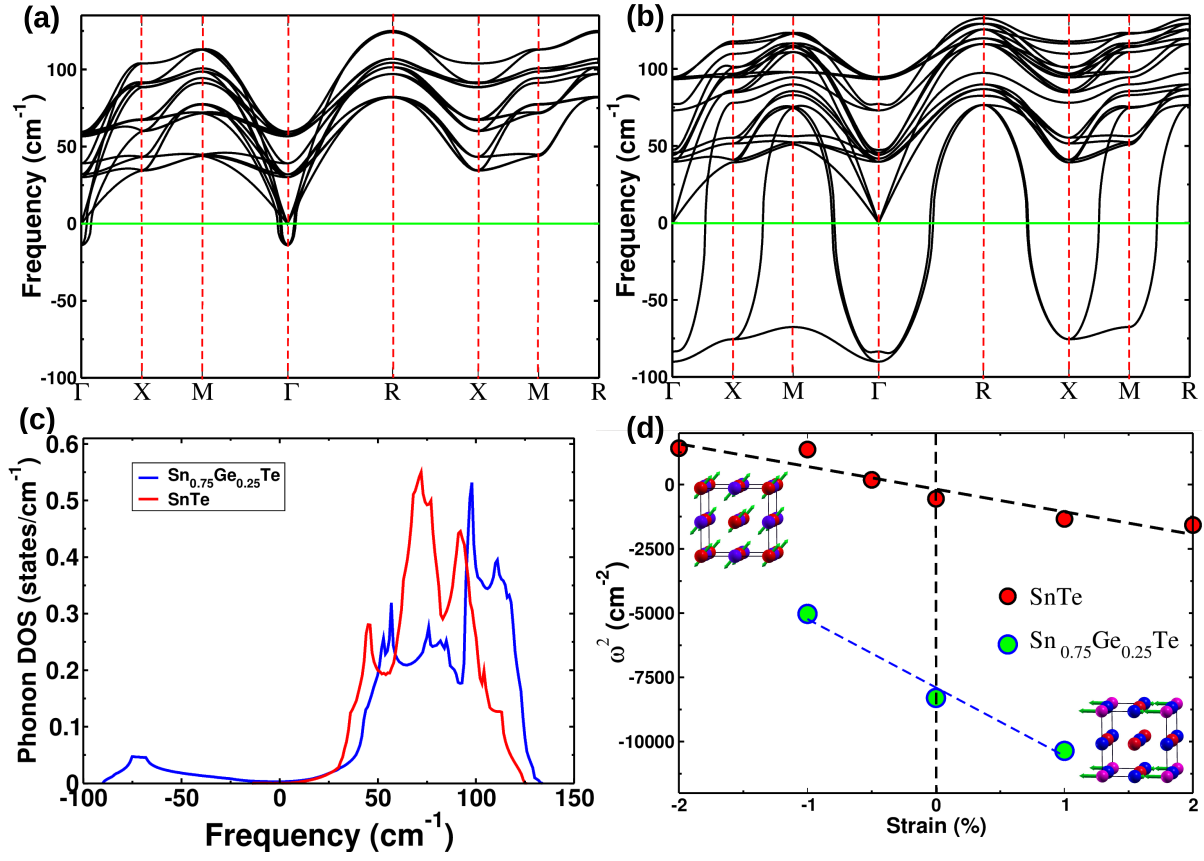


Figure 3.1: Phonon dispersion of (a) SnTe and (b) $\text{Sn}_{0.75}\text{Ge}_{0.25}\text{Te}$ in the centrosymmetric cubic rock salt structure at the theoretical lattice parameter without the inclusion of spin-orbit coupling (SOC), exhibiting unstable modes frequencies at $23i \text{ cm}^{-1}$ and $93i \text{ cm}^{-1}$ respectively. Vibrational density of states (VDOS) of (a) SnTe and (b) $\text{Sn}_{0.75}\text{Ge}_{0.25}\text{Te}$, show significantly larger number of unstable modes in the latter, which also mask notably stronger instability (c). Dependence of the squared frequencies of unstable phonon at zone centre on hydrostatic strain where strain is $(a - a_0)/a_0$ with $a_0 = 6.37 \text{ \AA}$ for SnTe and $a_0 = 6.28 \text{ \AA}$ for $\text{Sn}_{0.75}\text{Ge}_{0.25}\text{Te}$ (d). The slope $\partial\omega_0^2(\epsilon)/\partial\epsilon$ of $\text{Sn}_{0.75}\text{Ge}_{0.25}$ is significantly steeper than that of SnTe , signifying its stronger strain phonon coupling.

$\text{Sn}_{0.75}\text{Ge}_{0.25}\text{Te}$ [55,56]. We calculated the Born effective charges (Z^*) which reveals higher polarization power (significant deviations of Z^* from their nominal valence charges) of Ge^{2+} as compared to Sn^{+2} in $\text{Sn}_{0.75}\text{Ge}_{0.25}\text{Te}$ (Sn: $Z^*_{xx/yy/zz} = 6.63$; Ge: $Z^*_{xx/yy/zz} = 10.113$; Te: $Z^*_{xx/yy/zz} = -8.28$). Significantly stronger instability results in higher transition temperatures in $\text{Sn}_{1-x}\text{Ge}_x\text{Te}$ than that in SnTe .

We determined the extent of off-centring in SnTe and $\text{Sn}_{0.75}\text{Ge}_{0.25}\text{Te}$, to confirm the role of Ge displacements in giving a higher T_C of the doped system. We introduced

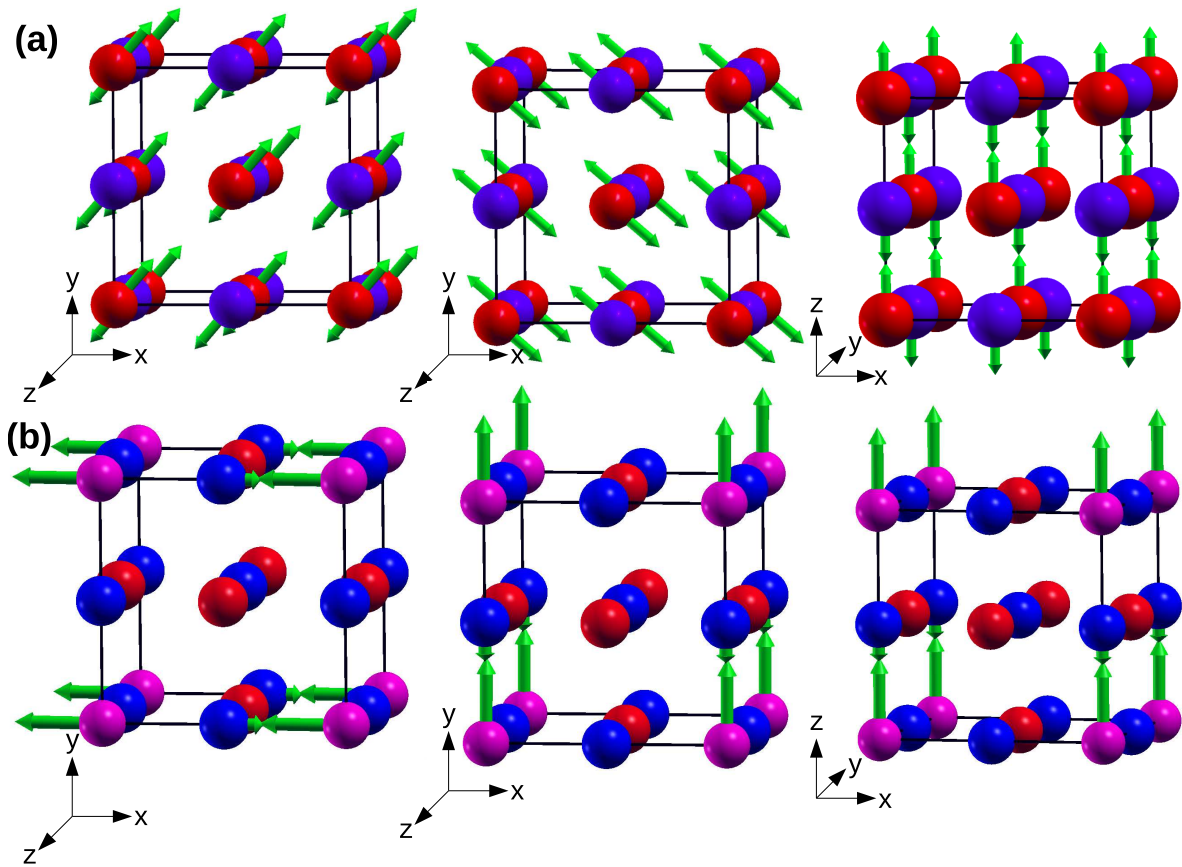


Figure 3.2: Visualisation of the atomic displacements of unstable phonons at the zone centre of (a) SnTe and (b) $\text{Sn}_{0.75}\text{Ge}_{0.25}\text{Te}$, Sn (Red in colour), Te (Blue in colour), and Ge (Pink in colour). There are equal and opposite displacements Sn and Te atoms in (a) SnTe , whereas the displacements of Ge atoms completely dominate the lattice instability in (b) $\text{Sn}_{0.75}\text{Ge}_{0.25}\text{Te}$.

displacements of $\sim 0.06 \text{ \AA}$ in $\langle 111 \rangle$ direction of all the cations and find that the relaxation of these distorted structures results in off-centring of 0.06 \AA of all the Sn atoms in SnTe and off-centring of $\sim 0.17 \text{ \AA}$ of Ge atom alone in $\text{Sn}_{0.75}\text{Ge}_{0.25}\text{Te}$ significantly higher than Sn displacements, off-centring Te by 0.08 \AA along the x, y and z directions in the first, second and third unstable modes respectively. From the larger negative frequencies, along with larger off-centring of Ge in $\text{Sn}_{0.75}\text{Ge}_{0.25}\text{Te}$ and the presence of larger polarization in the Ge: SnTe we conclude that the higher T_C of Ge: SnTe is due to strong Ge off-centring and associated a deeper potential energy well than in SnTe [57]. Γ Phonons of FE state of $\text{Sn}_{0.75}\text{Ge}_{0.25}\text{Te}$ do not exhibit any unstable modes with the lowest three optical modes at frequencies of 29 cm^{-1} , 32 cm^{-1} and 32 cm^{-1} , (related to the unstable modes of the

cubic structure with $\omega = 91.10i \text{ cm}^{-1}$) confirming its stability.

Mode	SnTe cm^{-1}	$\text{Sn}_{0.75}\text{Ge}_{0.25}\text{Te}$ cm^{-1}	Off-centred $\text{Sn}_{0.75}\text{Ge}_{0.25}\text{Te}$ cm^{-1}
1, 2, 3	23.4i	91.1i	29.7, 32.0, 32.0
4, 5, 6	0.0	0.0	0.0
7, 8, 9	21.1	38.2	35.1, 36.9, 36.9
10, 11, 12	21.4	40.8	42.6, 42.6, 47.2
13, 14, 15	31.2	46.1	61.7, 61.7, 71.1
16, 17, 18	54.1	73.3	75.5, 75.5, 82.4
19, 20, 21	55.5	88.5	88.1, 88.1, 91.2
22, 23, 24	58.1	93.2	91.9, 91.9, 104.7

Table 3.1: Γ Phonons of FE state of $\text{Sn}_{0.75}\text{Ge}_{0.25}\text{Te}$ do not exhibit any unstable modes in comparison to unstable modes in SnTe and $\text{Sn}_{0.75}\text{Ge}_{0.25}\text{Te}$

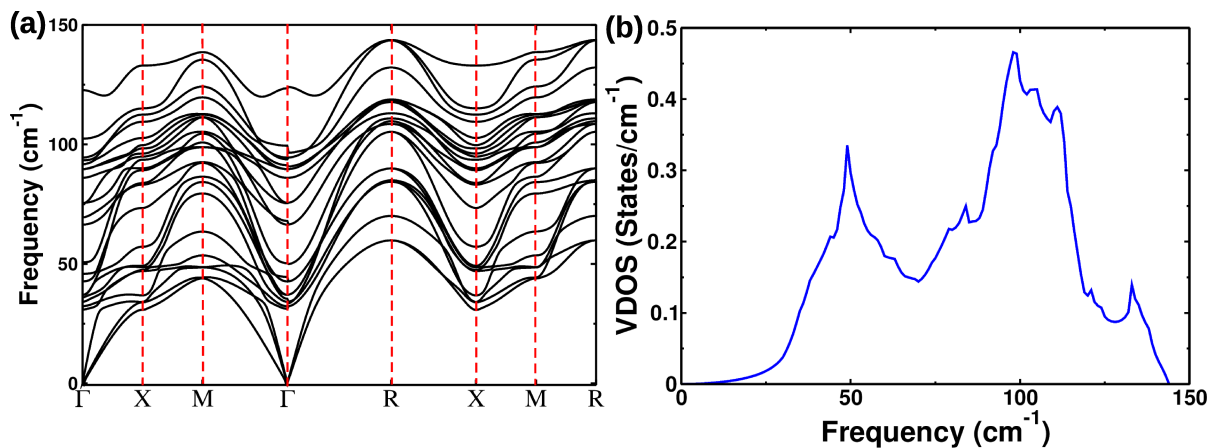


Figure 3.3: Phonon dispersion of (a) off -centred $\text{Sn}_{0.75}\text{Ge}_{0.25}\text{Te}$ in the centrosymmetric cubic rock salt structure without the inclusion of spin-orbit coupling (SOC) and the corresponding vibrational density of states (VDOS)(b). Γ Phonons of FE state of $\text{Sn}_{0.75}\text{Ge}_{0.25}\text{Te}$ do not exhibit any unstable modes.

We estimated the strength of lattice anharmonicity as measured by strain-phonon coupling using $\partial\omega_0^2(\epsilon)/\partial\epsilon$, where ω_0 is the frequency of unstable optical mode and $\epsilon = (a - a_0)/a_0$ is the strain applied in the system, a_0 being the theoretical lattice constant. The value of $(\partial\omega_0^2(\epsilon)/\partial\epsilon)$ gives the third order anharmonic coupling and our estimates are 785 cm^{-1} and 2664 cm^{-1} for SnTe and $\text{Sn}_{0.75}\text{Ge}_{0.25}\text{Te}$ (see Fig. 3.1d) respectively. Thus, the unstable optical phonons couple much more strongly with the acoustic phonons in

Ge:*SnTe* than in *SnTe*. It leads to the scattering of heat carrying acoustic phonons (essentially the sound waves) in the crystal structure and hence lower thermal conductivity.

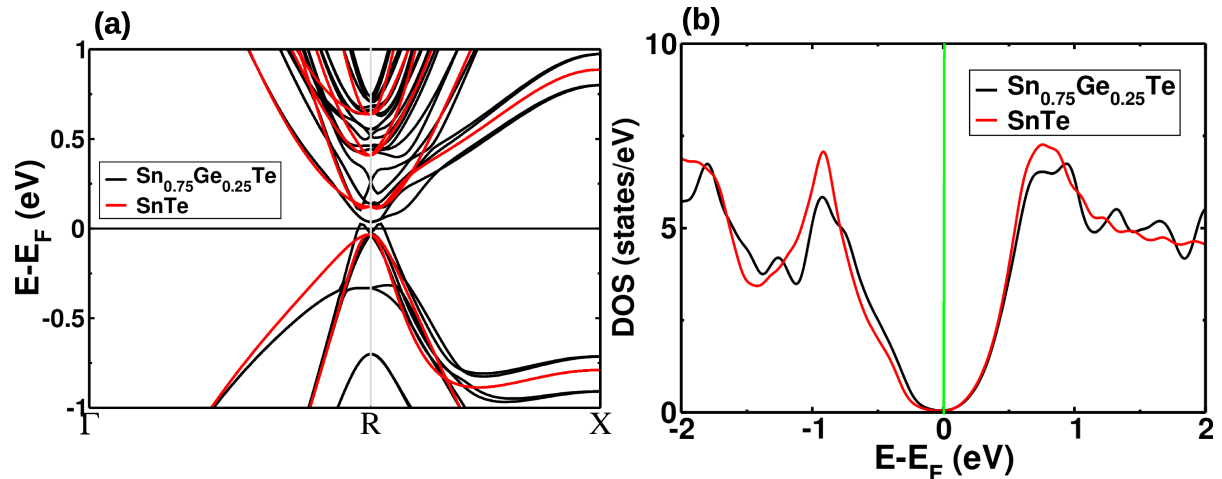


Figure 3.4: *Electronic structure of cubic ($Fm\bar{3}m$) phase of $SnTe$ and off-centred $Sn_{0.75}Ge_{0.25}Te$ calculated with the inclusion of effects of spin-orbit coupling (a) and the corresponding electronic density of states (b).*

Finally, the substantial role of Ge off-centring in suppressing thermal conductivity at higher Ge concentrations in comparison to lower Ge concentration was studied. The reduction of total energy (with respect to no off-centring) for only Ge off-centred $Sn_{0.75}Ge_{0.25}Te$ is -3.29 meV in comparison to -0.49 meV for $Sn_{0.875}Ge_{0.125}Te$ signifying the role of Ge off-centring in stabilising $Sn_{0.75}Ge_{0.25}Te$. The reduction of total energy for all cation off-centred $Sn_{0.75}Ge_{0.25}Te$ is -0.87 meV in comparison to -1.97 meV for $Sn_{0.875}Ge_{0.125}Te$ demonstrating the importance of Sn cation off-centring in reduction of total energy in $Sn_{0.875}Ge_{0.125}Te$. The prominent difference on moving from $Sn_{0.875}Ge_{0.125}Te$ (higher Ge concentration) to $Sn_{0.75}Ge_{0.25}Te$ being the reversal in the role of cations which are responsible for reduction in energy. This implies the significant involvement of Ge off-centring in reduction of energy for $Sn_{0.75}Ge_{0.25}Te$ and of Sn cations off-centring in $Sn_{0.875}Ge_{0.125}Te$ for lowering the energy. This establishes the substantial role of Ge off-centring in suppressing thermal conductivity at higher Ge concentrations in comparison to lower Ge concentration.

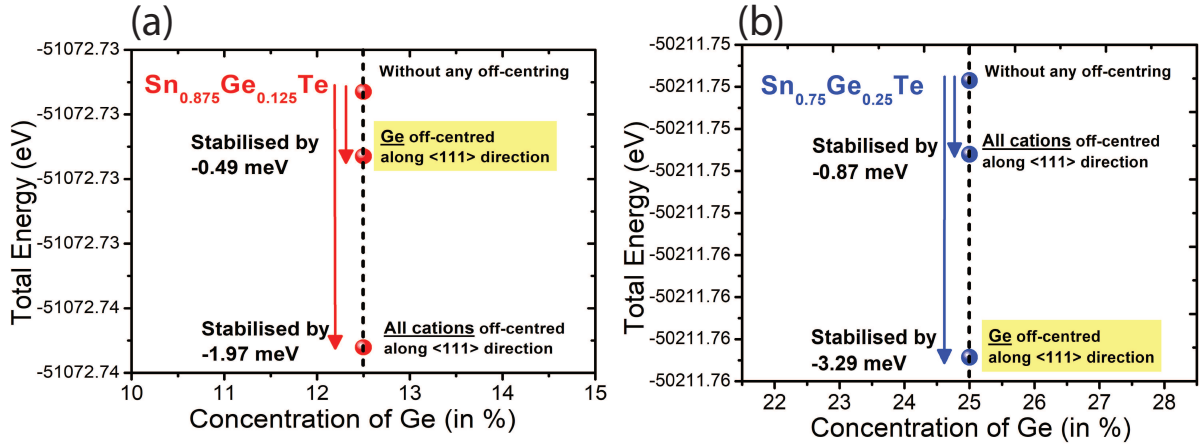


Figure 3.5: Total energies of Ge off-centred, all cations off-centred and without any off-centred $\text{Sn}_{1-x}\text{Ge}_x\text{Te}$ systems with (a) $x = 0.125$ and (b) $x = 0.25$.

3.4 Conclusion

In summary, we have shown that the high lattice anharmonicity caused by the introduction of Ge atom in SnTe crystal is responsible for its notably lower lattice thermal conductivity. Our analysis suggests that Ge exhibits rattler kind of behaviour i.e. the presence of dynamical local distortions in the doped system. The strategy of improving thermoelectric performance by tuning ferroelectric instability and associated local structural distortion as demonstrated here opens up a new avenue to achieve high performance thermoelectrics. This new strategy is engaging, particularly, because it can be readily applied to further boost the thermoelectric performance of materials like SnSe , GeTe , which are close to ferroelectric instabilities.

Bibliography

- [1] Tan, G., Zhao, L. -D. & Kanatzidis, M. G., *Chem. Rev.* **116**, 12123 (2016).
- [2] Ge, Z. -H. et al., *Mater. Today* **19**, 227 (2016).
- [3] Zhao, L. -D., Dravid, V. P. & Kanatzidis, M. G., *Energy Environ. Sci.* **7**, 251 (2014).
- [4] Xiao, Y. et al., *J. Am. Chem. Soc.* **139**, 18732 (2017).
- [5] Biswas, K. et al., *Nature* **489**, 414 (2012).
- [6] Samanta, M. & Biswas, K. *J. Am. Chem. Soc.* **139**, 9382 (2017).
- [7] Tan, G. et al., *Nat. Commun.* **7**, 12167 (2016).
- [8] Jana, M. K. & Biswas, K., *ACS Energy Lett.* **3**, 1315 (2018).
- [9] Snyder, G. J. & Toberer, E. S., *Nat. Mater.* **7**, 105 (2008).
- [10] Li, B. et al., *Nat. Mater.* **17**, 226 (2018).
- [11] Jana, M. K. et al., *J. Am. Chem. Soc.* **139**, 4350 (2017).
- [12] Jana, M. K., Pal, K., Waghmare, U. V. & Biswas, K., *Angew. Chem., Int. Ed.* **55**, 7792 (2016).
- [13] . Liu, H. et al., *Nat. Mater.* **11**, 422 (2012).
- [14] Roychowdhury, S. et al., *Angew. Chem., Int. Ed.* **57**, 4043 (2018).
- [15] Olvera, A.A. et al., *Energy Environ. Sci.* **10**, 1668 (2017).

-
- [16] Morelli, D., Jovovic, V. & Heremans, J., Phys. Rev. Lett. **101**, 035901 (2008).
- [17] Zhao, L. -D. et al., Nature **508**, 373 (2014).
- [18] Samanta, M., Pal, K., Pal, P., Waghmare, U. V. & Biswas, K., J. Am. Chem. Soc. **140**, 5866 (2018).
- [19] Cochran, W., Adv. Phys. **9**, 387 (1960).
- [20] . Murphy, R. M., Murray, É. D., Fahy, S. & Savić, I., Phys. Rev. B **95**, 144302 (2017).
- [21] Seddon, T., Farley, J. M. & Saunders, G.A., Solid State Commun. **17**, 55-57 (1975).
- [22] Delaire, O. et al., Nat Mater **10**, 614 (2011).
- [23] Jena, D. & Konar, A., Phys. Rev. Lett. **98**, 136805 (2007).
- [24] Zhang, X. & Pei, Y., npj Quantum Mater. **2**, 68 (2017).
- [25] Banik, A., Roychowdhury, S. & Biswas, K., Chem. Comm. **54**, 6573 (2018).
- [26] Zhang, Q. et al., Proc. Natl. Acad. Sci. USA **110**, 13261 (2013).
- [27] Tan, G. et al., J. Am. Chem. Soc. **136**, 7006 (2014).
- [28] Banik, A., Shenoy, U. S., Anand, S., Waghmare, U. V. & Biswas, K., Chem. Mater. **27**, 581 (2015).
- [29] Tan, G. et al., J. Am. Chem. Soc. **137**, 5100 (2015).
- [30] Banik, A., Shenoy, U. S., Saha, S., Waghmare, U. V. & Biswas, K., J. Am. Chem. Soc. **138**, 13068 (2016).
- [31] Banik, A., Vishal, B., Perumal, S., Datta, R. & Biswas, K., Energy Environ. Sci. **9**, 2011 (2016).
- [32] Li, W. et al., Adv. Mater. **29**, 1605887 (2017).

-
- [33] Waghmare, U. V., Spaldin, N. A., Kandpal, H. C. & Seshadri, R., Phys. Rev. B **67**, 125111 (2003).
- [34] Katayama, S. & Kawamura, H., Solid State Commun. **21**, 521 (1977).
- [35] Knox, K. R., Bozin, E. S., Malliakas, C. D., Kanatzidis, M. G. & Billinge, S. J. L., Phys. Rev. B **89**, 014102 (2014).
- [36] Mitrofanov, K. V. et al., Phys. Rev. B **90**, 134101 (2014).
- [37] Aggarwal, L. et al., J. Materiomics **2**, 196 (2016).
- [38] Lee, S. et al., Nat. Commun. **5**, 3525 (2014).
- [39] Sist, M. et al., IUCrJ **3**, 377 (2016).
- [40] Pawley, G. S., Cochran, W., Cowley, R. A. & Dolling, G., Phys. Rev. Letters **17**, 753 (1966).
- [41] Iizumi, M., Hamaguchi, Y., F. Komatsubara, K. & Kato, Y., J. Phys. Soc. Jpn. **38**, 443 (1975).
- [42] Murase, K. & Sugai, S., Solid State Comm. **32**, 89 (1979).
- [43] O'Neill, C.D. et al., Phys. Rev. B **95**, 144101 (2017).
- [44] Sugai, S., Murase, K. & Kawamura, H., Solid State Commun. **23**, 127 (1977).
- [45] Quantum-ESPRESSO is a community project for high-quality quantum-simulation software, based on density-functional theory, and coordinated by P. Giannozzi. See <http://www.quantum-espresso.org> and <http://www.pwscf.org>.
- [46] X. Hua, X. Chen, W. A. Goddard III, Phys. Rev. B **55**, 16103 (1997).
- [47] J. P. Perdew, K. Burke, M. Ernzerhof, Phys. Rev. Lett. **77**, 3865 (1996).
- [48] Bashkirov, Ss, and Ia Dobryakov, Kristallografiya **34**, 5 (1989).

-
- [49] S. Baroni, S. de Gironcoli, A. Dal Corso, and P. Giannozzi, *Rev. Mod. Phys.* **73**, 515 (2001).
- [50] K.R. Knox, E.S. Bozin, C.D. Malliakas, M.G. Kanatzidis, S.J.L. Billinge, *Phys Rev B* **89**, 1 (2014)
- [51] S. Sugai, K. Murase, H. Kawamura, *Solid State Commun.* **23**, 127 (1977).
- [52] W. Jantsch, *Dielectric Properties and Soft Modes in Semiconducting (Pb, Sn, Ge) Te* (Springer, 1983)
- [53] Mitrofanov, K. V., A. V. Kolobov, P. Fons, M. Krbal, T. Shintani, J. Tominaga, and T. Uruga, *Physical Review B* **90**, 13 (2014).
- [54] Krakauer, H., Yu, R., Wang, C. Z., Rabe, K. M., and Waghmare, U. V., *Journal of Physics: Condensed Matter* **11**, 18 (1999).
- [55] Trajic, J. et al., *J. Serb. Chem. Soc.* **72**, 55 (2007).
- [56] Zeier, W. G. et al., *Angew. Chem., Int. Ed.* **55**, 6826 (2016).
- [57] Lebedev, A. I., and I. A. Sluchinskaya, *Physics of the Solid State* **49**, 6 (2007).

Chapter 4

Stabilizing n-Type Cubic GeSe by Entropy-Driven Alloying of AgBiSe₂: Ultralow Thermal Conductivity and Promising Thermoelectric Performance*

4.1 Introduction

Thermoelectric materials can convert waste heat into electricity, which offers an important alternative to the solution of increasing global energy demand. The efficiency of a thermoelectric material depends on the dimensionless figure of merit, $zT = \sigma S^2 T / \kappa$, where σ , S , κ , and T are the electrical conductivity, Seebeck coefficient, thermal conductivity, and the temperature, respectively. [1,2] Most of the high performance thermoelectric materials are based on metal tellurides [1,2]. However, the abundance of Te is scarce in the Earth crust, which leads to the quest for the design and discovery of new thermoelectric materials

*This work has been published in *Angewandte Chemie* **130**, 15387 (2018). Reproduced with permission from John Wiley and Sons.

comprising earth abundant elements with less toxicity, such as Se. Importantly, although both p-type and n-type materials are required to construct a thermoelectric device, reports of n-type thermoelectric materials with ultralow thermal conductivity are very rare. Germanium chalcogenides (especially *GeTe*) are one of the most efficient thermoelectric materials in the Group IV–VI family and have been used for power generation in the mid-temperature range (600–800 K) since the 1960s [2, 3]. However, these germanium chalcogenide based thermoelectric materials are all p-type, limited by their intrinsic Ge vacancies [2, 3]. Thus, a speedy development of promising n-type germanium chalcogenide based thermoelectric materials is a forthwith requirement.

GeSe crystallizes in three different structures: orthorhombic (Pnma), rhombohedral (R3m), and cubic phases (Fm $\bar{3}$ m; Figure 4.2) depending on the temperature and pressure conditions [4, 5]. At ambient conditions, *GeSe* has the orthorhombic structure similar to that of *SnSe*, which shows an unprecedented zT in the single-crystal form owing to ultralow thermal conductivity [6]. Recently, by using first-principles density functional calculations, Hao et al. predicted the high thermoelectric performance in *GeSe* through carrier engineering [7]. However, the orthorhombic *GeSe* is experimentally found to be a p-type semiconductor with poor thermoelectric performance [8]. Recently, Huang et al. [4] have been able to stabilize the p-type rhombohedral GeSe by alloying it with *AgSbSe₂*, which showed a zT of 0.86 at 710K in *GeAg_{0.2}Sb_{0.2}Se_{1.4}*. They have achieved a low κ_L of $0.9\text{Wm}^{-1}\text{K}^{-1}$, which is, however, still higher than the theoretical κ_{min} of *GeSe* ($0.4\text{Wm}^{-1}\text{K}^{-1}$) [8]a. The room-temperature orthorhombic *GeSe* undergoes to a first-order structural transition to a face-centered cubic (FCC) structure (Figure 4.2) at 920 K [9]. This cubic phase of GeSe is unstable at ambient conditions because of the presence of several imaginary vibration modes in its phonon dispersion. Theoretical calculations, however, indicate that the application of external pressure of 7 GPa would lead to the stabilization of the cubic phase [5]. The high-symmetry cubic phases are in general much sought-after for high-performance thermoelectrics as they possess degenerate electronic band valleys. Therefore, the stabilization of cubic *GeSe* is worthwhile for improving its

thermoelectric performance.

Herein, Prof. Kanishka Biswas's group [†] demonstrate the experimental realization of high temperature and high-pressure cubic rock-salt phase of *GeSe* at ambient conditions by alloying with *AgBiSe₂* ($0.30 \leq x \leq 0.50$). Importantly, they found that cubic $(GeSe)_{1-x}(AgBiSe_2)_x$ exhibits n-type conduction in the 300–723 K range, which is extremely rare in germanium chalcogenide based thermoelectrics. Cubic $(GeSe)_{1-x}(AgBiSe_2)_x$ possesses an ultralow lattice thermal conductivity (κ_L) of 0.43– 0.7 Wm⁻¹K⁻¹ in the 300–723 K range. Solid solution mixing of *AgBiSe₂* with *GeSe* enhances the entropy and consequently leads to the stabilization of the cubic phase of *GeSe* at ambient conditions. The band gap of orthorhombic GeSe (1.1 eV) decreases to 0.05 eV with the initial formation of the rhombohedral $(GeSe)_{1-x}(AgBiSe_2)_x$ phase ($x=0.1$), and thereafter slightly increases to a value in the 0.3–0.4 eV range in cubic $(GeSe)_{1-x}(AgBiSe_2)_x$ ($0.30 \leq x \leq 0.50$). The combination of this ultralow κ_L , high Seebeck coefficient, and narrow band gap generates a promising thermoelectric figure of merit zT of 0.45 at 677 K in n-type $(GeSe)_{0.50}(AgBiSe_2)_{0.50}$. Our DFT calculations aim to verify the evolution of band gap with respect to alloying concentration in $(GeSe)_{1-x}(AgBiSe_2)_x$ and also the n-type character of cubic phase of $(GeSe)_{1-x}(AgBiSe_2)_x$ with ($0.35 \leq x \leq 0.50$).

4.2 Computational Details and Crystal Structure

We use density functional theoretical (DFT) methods as implemented in QUANTUM ESPRESSO (QE) code [10]. We used a generalised gradient approximation (GGA) [11] to the exchange-correlation energy functional as parametrized by Perdew, Burke, and Ernzerhof (PBE) [12]. To describe the interactions between valence electrons and ions we used Projected Augmented-Wave (PAW) potentials. Electronic wave functions and charge density were represented in plane wave basis sets truncated with cut-off energies of 45 Ry and 360 Ry respectively. The discontinuity in occupation numbers of electronic states was smeared using a Fermi-Dirac distribution function with broadening of $k_B T$

[†]New Chemistry Unit, Jawaharlal Nehru Centre for Advanced Scientific Research, Bangalore-560064.

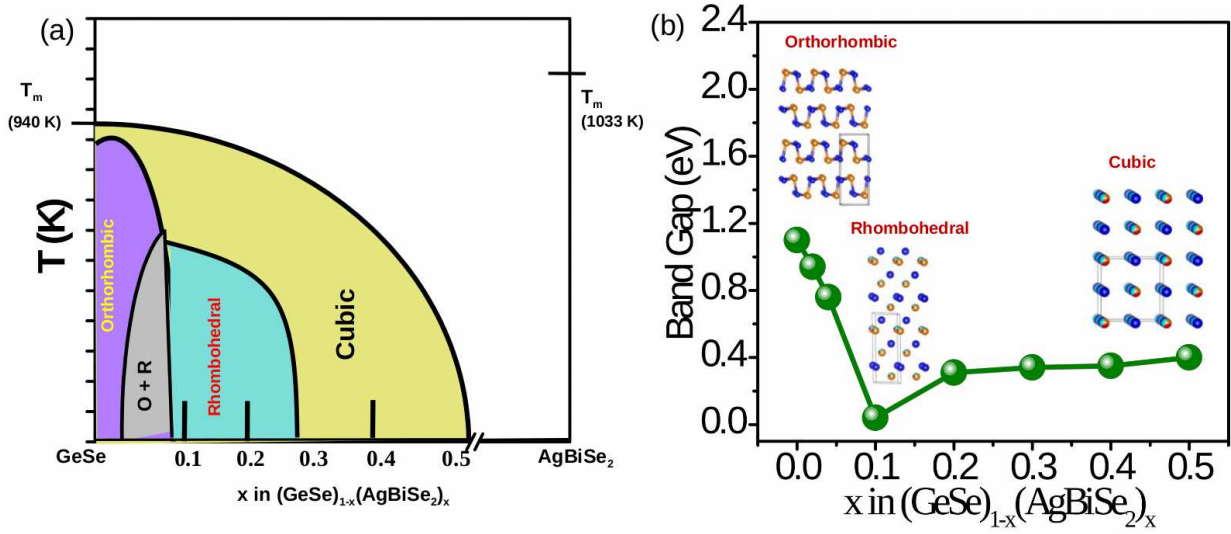


Figure 4.1: A possible phase diagram of the $GeSe-AgBiSe_2$ system based on temperature-dependent PXRD and DSC data(a). The evolution of the experimental band gap of $GeSe$ with increasing $AgBiSe_2$ concentration in $(GeSe)_{1-x}(AgBiSe_2)_x$.

$= 0.003$ Ry. We determined electronic structure of $GeSe$, $(GeSe)_{0.9}(AgBiSe_2)_{0.1}$ and $(GeSe)_{0.6}(AgBiSe_2)_{0.4}$ at their optimized lattice parameters. $GeSe$ crystallizes in three different structures: orthorhombic (Pnma), rhombohedral (R-3m) and cubic phases (Fm-3m) depending on the pressure and temperature conditions [13,14]. At ambient conditions, $GeSe$ stabilizes in the orthorhombic phase containing eight atoms in the unit cell, and we consider this phase in our theoretical analysis. Integrations over Brillouin Zone (BZ) were sampled on a uniform $8 \times 8 \times 8$ mesh of k-points. Electronic spectrum was determined at Bloch vectors along high symmetry lines ($\Gamma - X - S - Y - \Gamma - Z - U - R - T - Z - Y - T - U - X - S$) in the Brillouin zone. $(GeSe)_{0.9}(AgBiSe_2)_{0.1}$ exists in the rhombohedral phase and to simulate the desired concentration a $2 \times 2 \times 1$ supercell was considered. Electronic spectrum was determined at Bloch vectors along high symmetry lines ($\Gamma - M - K - \Gamma - A - L - H - A - L - M - K - H$) in the Brillouin zone of rhombohedral lattice. With further increase in concentration of $AgBiSe_2$, an FCC phase is stabilized. $(GeSe)_{0.6}(AgBiSe_2)_{0.4}$ exists in the cubic structure consisting of 8 atoms in the unit cell. To simulate this composition, a $2 \times 1 \times 1$ supercell was considered, and Brillouin Zone (BZ) integrations were sampled on a uniform $10 \times 12 \times 12$ mesh of k-points. Electronic spectrum was determined at Bloch

vectors along high symmetry lines ($\Gamma - X - M - \Gamma - Z - R - A - Z$) in the Brillouin zone of FCC lattice. We compared electronic structures with and without spin-orbit coupling (SOC) using fully relativistic and scalar relativistic potentials respectively.

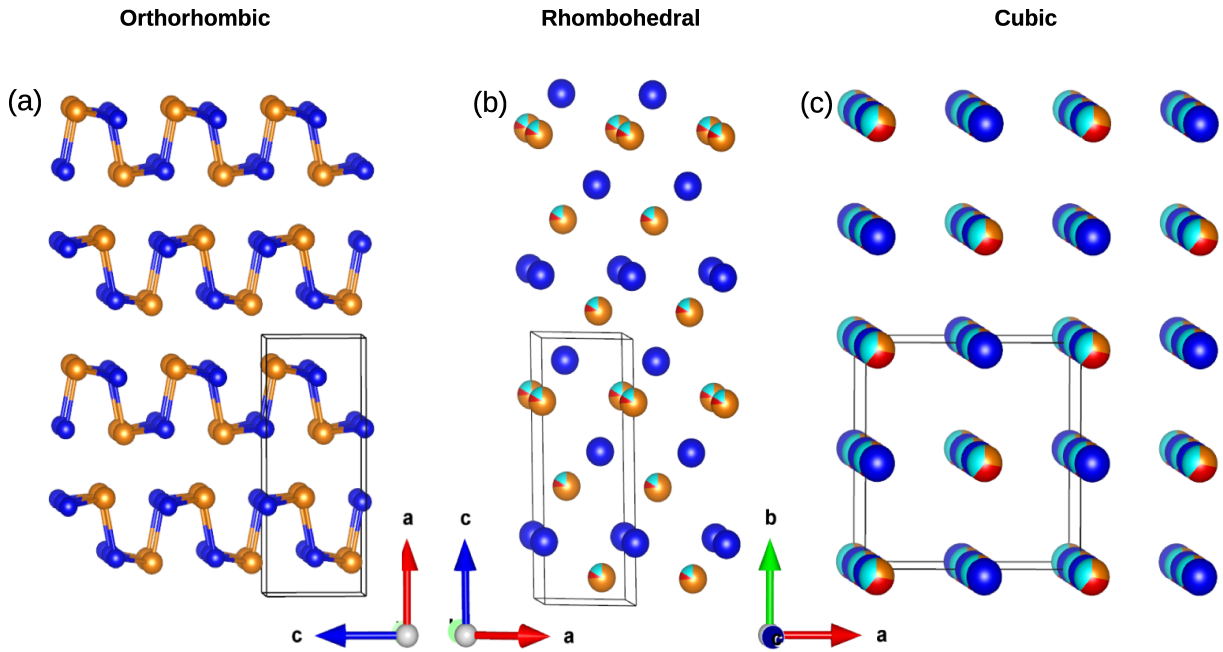


Figure 4.2: *Crystal structure of different phases of GeSe: orthorhombic (O), rhombohedral (R), and cubic (C). Ge Yellow, Se blue; Ag red, Bi cyan*

4.3 Results and Discussion

Experimentally, it is known that orthorhombic $GeSe$, gradually transforms to face-centred cubic structure via an intermediate rhombohedral phase when alloyed with $AgBiSe_2$. To study the evolution of band gap with respect to alloying concentration, we calculate electronic band structure at three concentrations: pure $GeSe$ (orthorhombic), $(GeSe)_{0.9}(AgBiSe_2)_{0.1}$ (rhombohedral) and $(GeSe)_{0.6}(AgBiSe_2)_{0.4}$ (cubic). Our optimized lattice parameters for pristine $GeSe$ in the orthorhombic structure (Pnma) are $a=11.10 \text{ \AA}$, $b=3.88 \text{ \AA}$, $c=4.47 \text{ \AA}$, which agree with the typical GGA errors with experimental lattice parameters ($a=10.92 \text{ \AA}$, $b=3.87 \text{ \AA}$, $c=4.41 \text{ \AA}$). The theoretical band gap of $GeSe$ in the orthorhombic structure is 0.93 eV , irrespective of the inclusion of the spin-orbit coupling in calculations (as shown in Figure 4.4a). Band gap estimated here

is slightly lower than the experimental band gap of 1.1 eV, which is typical of DFT calculations of gaps.

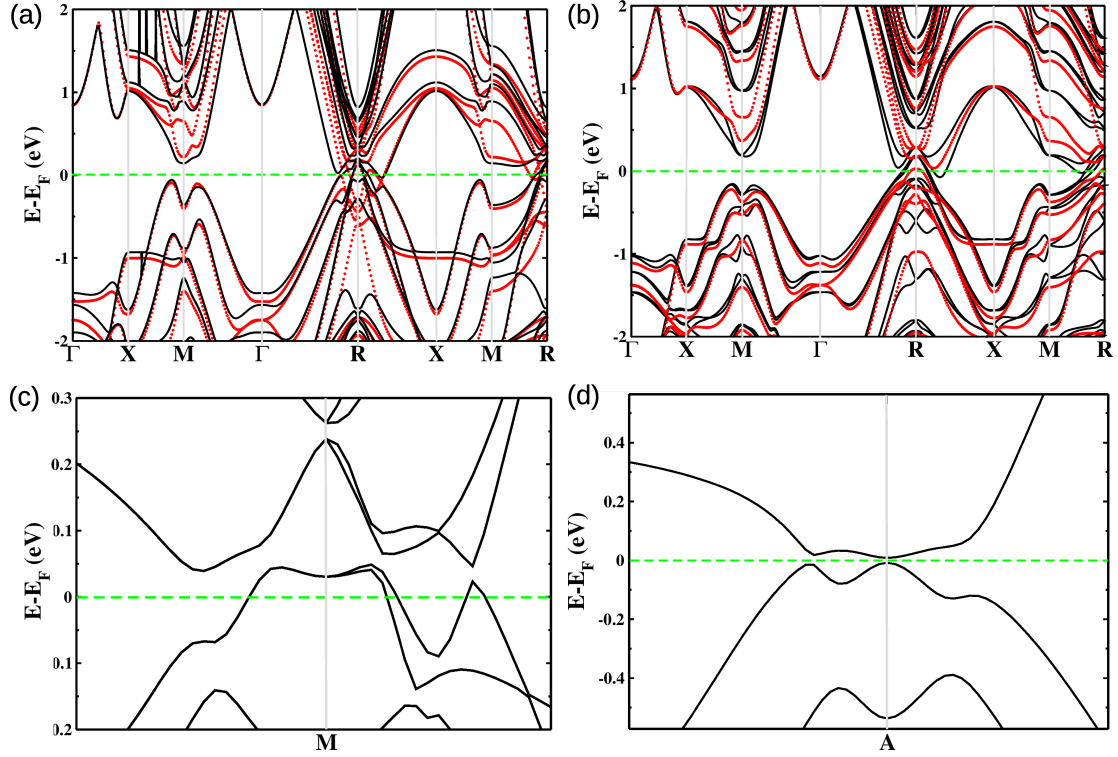


Figure 4.3: *Electronic structure of eight atoms FCC ($1 \times 1 \times 1$) (a) $(\text{GeSe})_{0.6}(\text{AgBiSe}_2)_{0.4}$ and (b) offcentered structure calculated with (black color lines) and without (red color lines) the inclusion of spinorbit interaction (SOI). Zoomed version of electronic structure of cubic $(\text{GeSe})_{0.60}(\text{AgBiSe}_2)_{0.40}$ ($1 \times 1 \times 2$, 16 atoms) at (c) M point and (d) A point which clearly shows conduction band minima and valence band maxima don't cross each other.*

Our estimates of lattice parameters of $(\text{GeSe})_{0.9}(\text{AgBiSe}_2)_{0.1}$ in the rhombohedral structure are $a=b=3.92 \text{ \AA}$ and $c=10.29 \text{ \AA}$, which agree well with experimental values of $a=b=3.98 \text{ \AA}$ and $c=10.17 \text{ \AA}$. We find that the band gap of *GeSe* decreases with *AgBiSe₂* alloying, consistent with the trend observed in experimental measurements using diffuse reflectance spectroscopy. Our estimates of the band gap of $(\text{GeSe})_{0.9}(\text{AgBiSe}_2)_{0.1}$ is $\sim 0.05 \text{ eV}$, when spin-orbit coupling is included smaller than the estimate of $\sim 0.2 \text{ eV}$ obtained from calculations without spin orbit coupling in our analysis.

$(\text{GeSe})_{1-x}(\text{AgBiSe}_2)_x$ with $x=0.4$ exists in the cubic phase (Fm-3m) with experimental lattice parameters $a=b=c=5.76 \text{ \AA}$ and the optimized lattice parameters obtained here

are $a=b=5.77 \text{ \AA}$ and $c=11.58 \text{ \AA}$ (for the $1 \times 1 \times 2$ supercell). In the current experimental work, the observed band gap slightly increases and stays about 0.3-0.4 eV in the cubic phase when the concentration of $AgBiSe_2$ increases above $x > 0.1$. Electronic structures of the 8 atoms FCC unit cell calculated with and without SOC reveal vanishing band gaps with overlapping bands at the fermi level (see Figure 4.3a). To get a more accurate estimate of band gap theoretically, we investigated the role of structural distortions in cubic phase. We determined the extent of off-centring by introducing displacements in Bi atom along the $\langle 111 \rangle$ direction. The relaxation of the structure results in large off-centring with values shown in the Table 1.

	Along x direction \AA	Along y direction \AA	Along z direction \AA
Ge	0.17	0.08	0.06
Ag	0.19	0.24	0.19
Bi	0.03	0.02	0.03
Ge	0.06	0.08	0.17
Se	0.01	0.18	0.03
Se	0.14	0.03	0.14
Se	0.03	0.03	0.05
Se	0.11	0.04	0.02

Table 4.1: *Off-centring displacements of atoms in the cubic structure of $(GeSe)_{0.6}(AgBiSe_2)_{0.4}$ obtained after relaxation of the structure.*

Electronic structure of the relaxed structure calculated without SOC has a band gap of 0 eV whereas we find weakly overlapping bands at R point and the fermi level after effects of SOC are included (as shown in Figure 4.3b). We simulated chemical disorder in the system with a $1 \times 1 \times 2$ supercell. Electronic structure calculated with this supercell of $(GeSe)_{0.6}(AgBiSe_2)_{0.4}$, without including spin-orbit interaction reveals overlapping bands at the fermi level and a band gap of 0 eV when spin-orbit coupling is included (as shown in Figure 4.4c).

For better understanding of the electronic properties, we examined the projected density of states (PDOS). In pure $GeSe$, we find that valence band (VB) is contributed mostly by Se-p orbitals, and weakly by Ge-s and Ge-p orbitals. Its conduction band (CB)

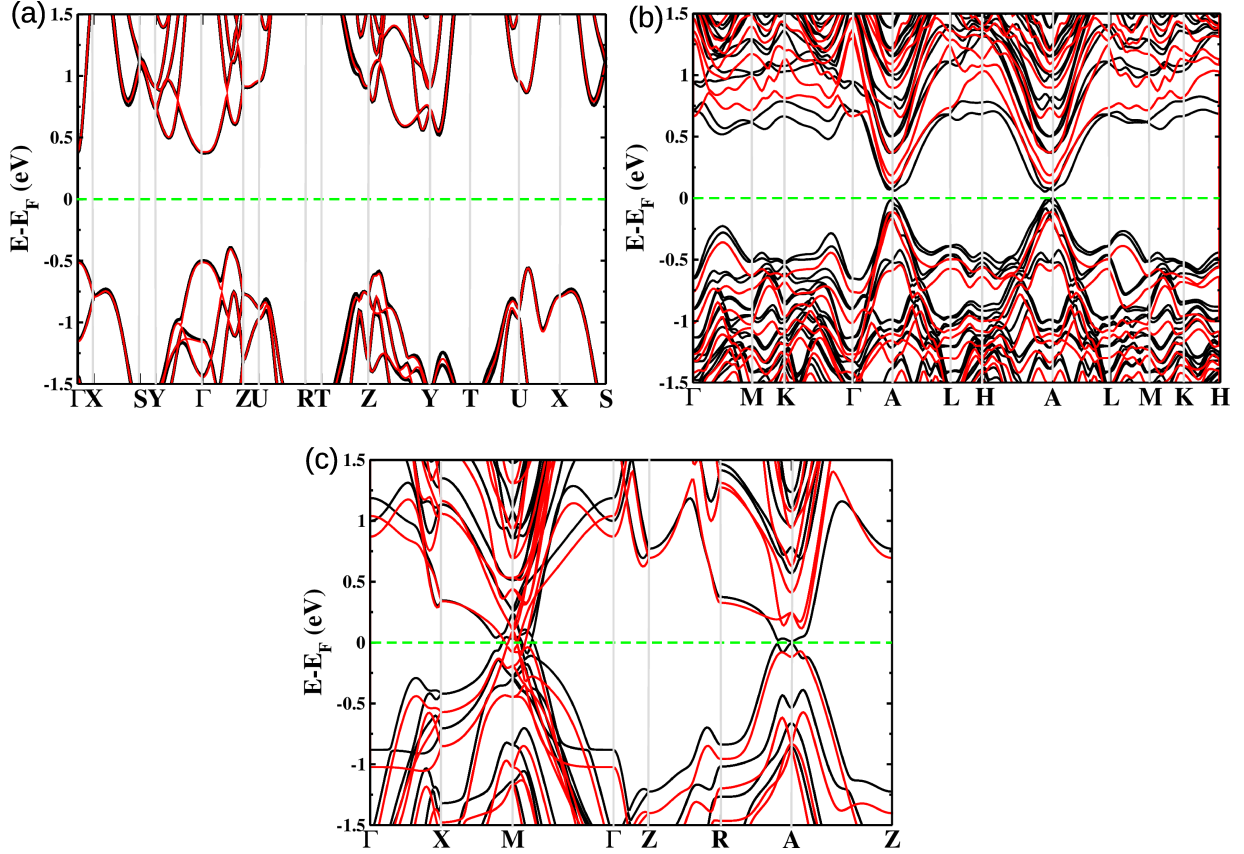


Figure 4.4: *Electronic band structure of a) orthorhombic GeSe, b) rhombohedral, and c) cubic $(GeSe)_{0.90}(AgBiSe_2)_{0.10}$ and $(GeSe)_{0.60}(AgBiSe_2)_{0.40}$ respectively with (black lines) and without (red lines) the inclusion of spin-orbit coupling (SOC).*

is contributed by Ge-p orbitals. In the rhombohedral phase, contributions to valence band are dominated by Se-p, Ge-s and Ge-p orbitals as was seen in pure GeSe, while the CB is contributed by Ge-p orbitals and weakly by Bi-p and Se-p orbitals. In the cubic phase, contributions of Ge-s and Ge-p orbitals to the VB vanishes and Bi-p, Se-p and Ge-p orbitals contribute to the CB. The density of states of $(GeSe)_{1-x}(AgBiSe_2)_x$ with $x = 0, 0.1$ and 0.4 are shown in Figure 4.5a), 4.5b) and 4.5c) respectively. Ge-chalcogenide based thermoelectric materials are generally p-type semiconductors owing to intrinsic Ge vacancies, and so far, the pristine orthorhombic *GeSe* seems to be no exception to this. However, the cubic $(GeSe)_{1-x}(AgBiSe_2)_x$ ($0.35 < x < 0.50$) show negative S values indicating a n-type conduction. The n-type carrier conduction is also in agreement with the negative sign of Hall coefficients. Bi^{3+} substitution in place of Ge^{2+} acts as a donor

dopant and increases the n-type carrier concentration which is also evident from the projected density of states (PDOS) analysis. While, the contribution of the Ge p-orbital is significant in the formation of the conduction band (CB) edge of orthorhombic and rhombohedral GeSe, the contribution of Bi p-orbital considerably increases and Ge p vanishes in the CB edge of cubic phase.

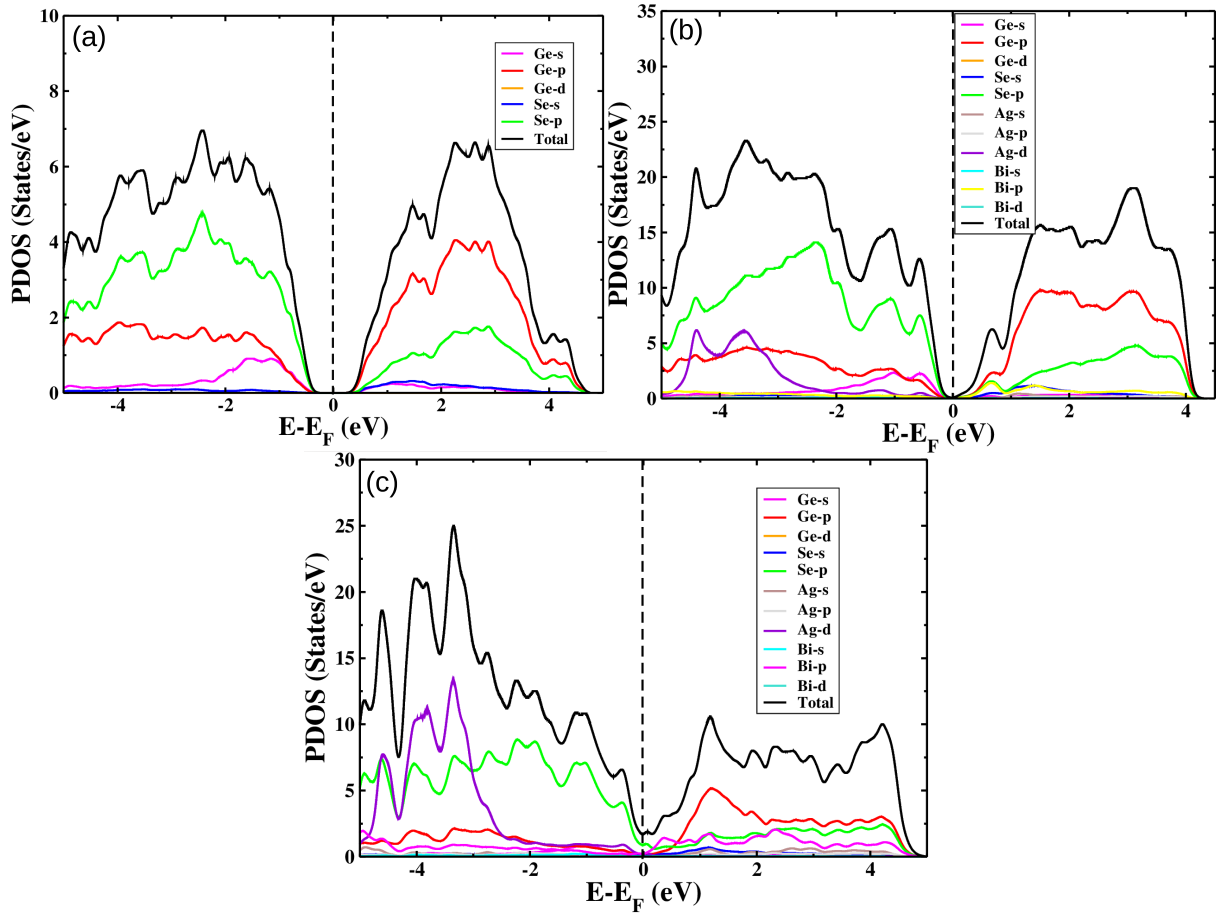


Figure 4.5: *Electronic density of states (DOS) and projected density of states (PDOS) of (a) GeSe (orthorhombic), (b) (GeSe)_{0.9}(AgBiSe₂)_{0.1} (rhombohedral) and (c) (GeSe)_{0.6}(AgBiSe₂)_{0.4} (cubic) calculated with inclusion of the spin-orbit coupling.*

4.4 Conclusion

In summary, using first-principles calculations within density functional theory, we reproduce the trend in the evolution of band gap of $(GeSe)_{1-x}(AgBiSe_2)_x$ with increasing x .

The gap in the cubic structure stabilized at large x is strongly influenced by the chemical disorder in occupation of Bi, Ag and Ge at the cationic site. The anomalous closing and opening of the band gap of $GeSe$ with increasing $AgBiSe_2$ concentration is due to the influence of positive (rhombohedral phase) and negative (cubic phase) chemical pressure. Interestingly, cubic $(GeSe)_{1-x}(AgBiSe_2)_x$ possess n-type conduction with reasonable high carrier concentration, which is rare in Ge-chalcogenides based thermoelectrics.

Bibliography

- [1] a) G. Tan, L.-D. Zhao, M. G. Kanatzidis, *Chem. Rev.* **116**, 12123 (2016); b) J. Sootsman, D. Y. Chung, M. G. Kanatzidis, *Angew. Chem. Int. Ed.* **48**, 8616 (2009); *Angew. Chem.* **121**, 8768 (2009); c) Z. Ge, L. Zhao, D. Wu, X. Liu, B. Zhang, J. Li, J. He, *Mater. Today* **19**, 227 (2016); d) Y. Xiao, H. Wu, W. Li, M. Yin, Y. Pei, Y. Zhang, L. Fu, Y. Chen, S. J. Pennycook, L. Huang, J. He, L.-D. Zhao, *J. Am. Chem. Soc.* **139**, 18732 (2017); e) K. Biswas, J. He, I. D. Blum, C. I. Wu, T. P. Hogan, D. N. Seidman, V. P. Dravid, M. G. Kanatzidis, *Nature* **489**, 414 (2012); f) B. Poudel, Q. Hao, Y. Ma, Y. Lan, A. Minnich, B. Yu, X. Yan, D. Wang, A. Muto, D. Vashaee, X. Chen, J. Liu, M. S. Dresselhaus, G. Chen, Z. Ren, *Science* **320**, 634 (2008); g) A. Banik, S. Roychowdhury, K. Biswas, *Chem. commun.* **54**, 6573 (2018).
- [2] a) R. J. Korkosz, T. C. Chasapis, S.-h. Lo, J. W. Doak, Y. J. Kim, C.-I. Wu, E. Hatzikraniotis, T. P. Hogan, D. N. Seidman, C. Wolverton, V. P. Dravid, M. G. Kanatzidis, *J. Am. Chem. Soc.* **136**, 3225 (2014); b) M. Samanta, K. Biswas, *J. Am. Chem. Soc.* **139**, 9382 (2017); c) Q. Zhang, B. L. Liao, Y. C. Lan, K. Lukas, W. S. Liu, K. Esfarjani, C. Opeil, D. Broido, G. Chen, Z. Ren, *Proc. Natl. Acad. Sci. USA* **110**, 13261 (2013).
- [3] a) S. Perumal, S. Roychowdhury, K. Biswas, *J. Mater. Chem. C* **4**, 7520 (2016); b) F. D. Rosi, J. P. Dismukes, E. F. Hockings, *Electr. Eng.* **79**, 450 (1960); c) F. Fahrnbauer, D. Souchay, G. Wagner, O. Oeckler, *J. Am. Chem. Soc.* **137**, 12633 (2015); d) S. Perumal, S. Roychowdhury, D. S. Negi, R. Datta, K. Biswas, *Chem. Mater.* **27**, 7171 (2015); e) J. Li, X. Zhang, S. Lin, Z. Chen, Y. Pei, *Chem. Mater.* **29**, 605 (2017); f)

- Y. Gelbstein, J. Davidow, S. N. Girard, D. Y. Chung, M. G. Kanatzidis, *Adv. Energy Mater.* **3**, 815 (2013); g) D. Wu, L.-D. Zhao, S. Hao, Q. Jiang, F. Zheng, J. W. Doak, H. Wu, H. Chi, Y. Gelbstein, C. Uher, C. Wolverton, M. G. Kanatzidis, J. He, *J. Am. Chem. Soc.* **136**, 11412 (2014); h) S. Roychowdhury, K. Biswas, *Chem* 2018, 4, 939; i) S. Roychowdhury, M. Samanta, S. Perumal, K. Biswas, *Chem. Mater.* **30**, 5799 (2018).
- [4] Z. Huang, S. A. Miller, B. Ge, M. Yan, S. Anand, T. Wu, P. Nan, Y. Zhu, W. Zhuang, G. J. Snyder, P. Jiang, X. Bao, *Angew. Chem. Int. Ed.* **56**, 14113 (2017); *Angew. Chem.* **129**, 14301 (2017).
- [5] V. L. Deringer, R. P. Stoffel, R. Dronskowski, *Phys. Rev. B* **89**, 094303 (2014).
- [6] L.-D. Zhao, S.-H. Lo, Y. Zhang, H. Sun, G. Tan, C. Uher, C. Wolverton, V. P. Dravid, M. G. Kanatzidis, *Nature* **508**, 373 (2014).
- [7] S. Hao, F. Shi, V. P. Dravid, M. G. Kanatzidis, C. Wolverton, *Chem. Mater.* **28**, 3218 (2016).
- [8] a) X. Zhang, J. Shen, S. Lin, J. Li, Z. Chen, W. Li, Y. Pei, *J. Materiomics* **2**, 331 (2016); b) M. A. Hughes, Y. Fedorenko, B. Gholipour, J. Yao, T.-H. Lee, R. M. Gwilliam, K. P. Homewood, S. Hinder, D. W. Hewak, S. R. Elliott, R. J. Curry, *Nat. Commun.* **5**, 5346 (2014).
- [9] M. Sist, C. Gatti, P. Nørby, S. Cenedese, H. Kasai, K. Kato, B. B. Iversen, *Chem. Eur. J.* **23**, 6888 (2017).
- [10] Quantum-ESPRESSO is a community project for high-quality quantum-simulation software, based on density-functional theory, and coordinated by P. Giannozzi. See <http://www.quantum-espresso.org> and <http://www.pwscf.org>.
- [11] X. Hua, X. Chen, W. A. Goddard III, *Phys. Rev. B* **55**, 16103 (1997).
- [12] J. P. Perdew, K. Burke, M. Ernzerhof, *Phys. Rev. Lett.* **77**, 3865 (1996).

-
- [13] Z. Huang, S. A. Miller, B. Ge, M. Yan, S. Anand, T. Wu, P. Nan, Y. Zhu, W. Zhuang, G.J. Snyder, P. Jiang, X. Bao, *Angew. Chem. Int. Ed.* **56**, 14113 (2017).
- [14] V.L. Deringer, R.P. Stoffel, R. Dronskowski, *Phys. Rev. B* **89**, 094303 (2014).

Chapter 5

Phonon signatures of multiple topological quantum phase transitions in compressed TlBiS_2^*

5.1 Introduction

Topological insulators (TI) are a new kind of electronic state of matter possessing spin polarized conducting states at their surface and insulating states in its bulk. The existence of time reversal symmetry protects the topological surface states against non-magnetic impurities or defects [1]. TI have potential application in spintronics and quantum computation devices and also offers the essential platform to realize quantum particles like Majorana Fermions in condensed matter systems [1]. At first, theoretical prediction of TI were made in HgTe/CdTe quantum wells (two dimensional (2D)) [2] with subsequent experimental observations [3]. Soon after this discovery, bulk 3D TI materials (various strong SOC systems) were predicted theoretically [4] and confirmed using angle resolved photo emission spectroscopy (ARPES) at an ambient conditions [5–7]. Interestingly, some narrow band gap materials (at ambient conditions) with strong SOC have ability to be

*Manuscript based on this work under review in Phys. Rev. B: V. Rajaji, Raagya Arora, Saurav Ch. Sarma, B. Joseph, Umesh V. Waghmare, Sebastian C. Peter, and Chandrabhas Narayana

tuned into a topological insulator by external strain [8,9]. The non-adiabatic process involving the transformation of normal bulk insulator into a topological insulator is termed as the topological quantum phase transition (TQPT). The topological invariant quantity Z_2 characterizes the changes in the electronic state of the system ($Z_2 = 0$ trivial insulator and $Z_2 = 1$ non-trivial insulator) [1,10] during TQPT. Z_2 is the product of parities at the time reversal invariant momenta (TRIM) points of the Brillouin zone (BZ) of the system. In general, strain can be applied to the system either by chemical (doping or substitution) or physical methods (lattice compression). The physical route being cleaner (no atomic scale chemical inhomogeneities) is more appropriate in comparison to the chemical route which induces chemical disorder (inhomogeneities) in the system.

Another interesting class of materials are called as topological crystalline insulators (TCI) [11,12], where the gapless surface states are protected by mirror symmetry. These materials are different from topological insulators (TI) in which the time reversal symmetry protects the surface states and hence the protection of surface states for TCI perseveres even when time-reversal symmetry is broken. The presence of mirror symmetry in the crystal structure of a material results in the presence of planes in the BZ that are mirror symmetric. Therefore, mirror symmetry protected Dirac cones arise in the surface electronic structure. TCIs are characterized by a non-zero mirror Chern number. The individual Chern numbers C_{+i} and C_{-i} are defined on a mirror-invariant plane. The mirror Chern number [11] defined as $n_M = (C_{+i} - C_{-i})/2$ can be used as a topological invariant for TCI. A TCI supports an even number of Dirac cones and band inversions in sharp contrast to a TI characterized by odd number of band inversions. The first TCI phase experimental [13] observation was made in SnTe, which were earlier theoretically [14] predicted.

The narrow band gap tetradymite semiconductors Bi_2Se_3 (band gap $E_g = 0.30$ eV), Bi_2Te_3 ($E_g = 0.12$ eV) and Sb_2Te_3 ($E_g = 0.28$ eV) crystallize in rhombohedral structure (space group SG: $R\bar{3}m$) and are 3D TI at ambient conditions with surface states consisting of a single Dirac cone at the Γ point of the BZ [4–7]. In the tetradymite

semiconductors family, the Bi_2Se_3 is having the larger band gap ($E_g \sim 1$ eV) and lesser SOC strength than remaining members (Bi_2Se_3 , Bi_2Te_3 , and Sb_2Te_3). There are no topologically non-trivial states present at ambient conditions in Sb_2Se_3 . It is well known that the thermodynamic parameter pressure P can tune the strength of the SOC and also the band gap. Interestingly, hydrostatic pressure induced band inversion with parity change at Γ point in the Sb_2Se_3 compound has been theoretically predicted [15] and then subsequently phonon anomalies are noticed at ~ 2.5 GPa [16]. Similarly, thallium based III-V-VI₂ ternary chalcogenides $TlBiSe_2$ ($E_g = 0.28$ eV) and $TlBiTe_2$ ($E_g = 0.11$ eV) crystallize in rhombohedral structure (SG: $R\bar{3}m$) and are 3D TI at ambient conditions [17]. In this family, $TlBiS_2$ ($E_g = 0.42$ eV) is having relatively higher band gap and lesser SOC than $TlBiSe_2$ and $TlBiTe_2$ compounds. Under the application of external strain, the TQPT is theoretically predicted in the $TlBiS_2$ system [18]. The above two examples (tetradymite semiconductors and thallium based III-V-VI₂ ternary chalcogenides) illustrate the interplay between the crystal symmetry, band gap, and spin orbit coupling. In other words, when the compound of 3D TI family shares the same crystal and electronic structure, but lacks the band gap and SOC, and then pressure can serve as an ideal external tool to induce the band inversion in it.

Thallium based III-V-VI₂ ternary chalcogenide $TlBiS_2$ is the narrow band gap semiconducting material and has significant interest on the aspect of thermoelectric and topological properties under different conditions [18]. Even though $TlBiS_2$ share the same crystal structure (SG: $R\bar{3}m$) as tetradymite compounds (Bi_2Se_3 , Bi_2Te_3 , and Sb_2Te_3), there is a considerable difference exists between them. The tetradymite semiconductors consist of quintuple layers stacking along the c axis, and each quintuple layers are separated by weak Van der Waals type interactions and therefore it is a quasi 2D nature. In $TlBiS_2$, each Tl (or Bi) layer is sandwiched between the two S layers. But, strong coupling exists between the two layers and makes it intrinsically 3D natures [18,19]. Recently, it is observed that the substitution of Se ($x \sim 0.5$) at S site [$TlBi(S_{1-x}Se_x)_2$], leading to the formation of a single Dirac cone at the Γ point [20]. Here, the substituted Se (i)

increases the effective SOC strength of $TlBiS_2$ compound without changing the crystal structure, and (ii) decreases the band gap. Consequently non-trivial topological phase transition ($Z_2=1$) is observed in $[TlBi(S_{1-x}Se_x)_2]$ at ambient pressure. This interesting chemical approach strongly stimulated us to perform the high pressure studies on $TlBiS_2$. Because, the substitution of Se is analogous to the externally applied pressure which can also possibly tune the effective hybridization, the relative strength of the SOC, bandgap and topological invariant Z_2 .

In this work, the pressure dependent structural and vibrational properties of the rhombohedral phase of $TlBiS_2$ compound were investigated using in situ synchrotron XRD and Raman scattering measurements respectively by Prof. Chandrabhas Narayana's group.[†] Combined Raman and synchrotron XRD results indicate that the rhombohedral phase shows the structural stability up to ~ 4.0 GPa and beyond which the first-order structural phase transition takes place. Further, two isostructural electronic transitions are observed from phonon (E_g and A_{1g}) anomalies at ~ 0.5 GPa and ~ 1.80 GPa and corroborated with our first principle theoretical calculations to TQPT ($Z_2 = 1$) and TCI ($n_M = 2$) transitions respectively. Finally, the significance of the obtained results is discussed in connection with other known pressure induced topological materials.

5.2 Computational Details and Crystal Structure

Our first-principles theoretical calculations are based on density functional theory (DFT) employing the Quantum ESPRESSO (QE) code [21]. We used a generalized gradient approximation (GGA) [22] to the exchange-correlation energy functional as parametrized by Perdew, Burke, and Ernzerhof (PBE) [23]. The projector augmented wave (PAW) potentials [24] with valence configuration $4f^{14} 6s^2 6p^2 5d^{10}$, $4f^{14} 6s^2 6p^3 5d^{10}$ and $4d^{10} 5s^2 5p^2$ were adopted for Tl, Bi and S respectively. Electronic wave functions and charge density were represented in plane wave basis sets truncated with cut-off energies of 55

[†]Chemistry and Physics of Materials Unit, Jawaharlal Nehru Centre for Advanced Scientific Research, Bangalore-560064.

Ry and 550 Ry respectively. The discontinuity in occupation numbers of electronic states was smeared using a Fermi-Dirac distribution function with broadening of $k_B T = 0.003$ Ry and integrations over BZ were sampled on a uniform $6 \times 6 \times 6$ mesh of k-points. In the simulation of pressure-dependent properties, we used scalar-relativistic PAW potentials to optimize the structure with respect to lattice constants and atomic coordinates. The structure was optimized to minimize the enthalpy, $H = E + PV$ at a given pressure. Atomic coordinates of these optimized structures were used as the initial structure for further optimization using fully-relativistic potentials. Effects of SOC were included in our calculations of the electronic structure through the use of fully relativistic potentials [24], while we used scalar-relativistic PAW potentials in the calculation of phonons. Electronic spectrum was determined at Bloch vectors along high symmetry lines ($\Gamma - L - Z - F - \Gamma - Z$) in the BZ. Lattice dynamical properties were determined using density functional linear response (called as density functional perturbation theory [25]) as implemented in the QE package [21]. To obtain phonon dispersion, dynamical matrices were obtained on a $2 \times 2 \times 2$ q-points grid in the BZ. We Fourier interpolated these dynamical matrices to obtain the phonon dispersion along high symmetry lines ($\Gamma - L - Z - F - \Gamma - Z$) in the BZ. To determine the bulk electronic topology of $TlBiS_2$, we used Z2PACK code [26] to determine the Z_2 topological invariants and mirror Chern number (n_M). This code uses hybrid Wannier functions [27, 28] and employs the ideas of time reversal polarization in the determination of the Z_2 invariants.

We used first-principles calculations to simulate the rhombohedral phase (SG: $R\bar{3}m$) of $TlBiS_2$ as a function of pressure. The structure is centrosymmetric with inversion centres at both Tl and Bi atoms. Tl, Bi, and two S atoms are located at the $(0.5, 0.5, 0.5)$, $(0, 0, 0)$, (u, u, u) and $(1-u, 1-u, 1-u)$ sites, respectively. Our estimates of the optimized lattice constants of $TlBiS_2$ are $a = 7.74 \text{ \AA}$ and angle $\alpha = 31.03^\circ$, which agree within the typical GGA errors with experimental lattice parameters ($a = 7.67 \text{ \AA}$, $\alpha = 31.05^\circ$) [30]. The calculated internal parameter characterizing the positions of the S atoms is $u = 0.261$.

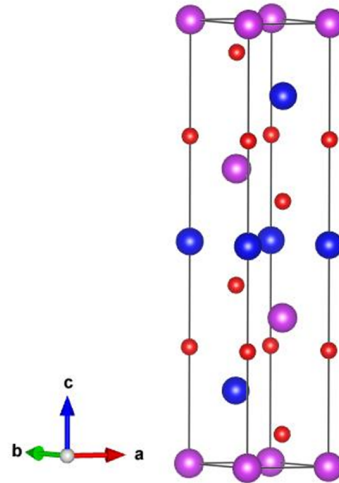


Figure 5.1: Unit cell of the hexagonal (supercell) phase of $TlBiS_2$ (violet, blue, and red spheres represents the Tl, Bi, and S atoms respectively).

5.3 Results and Discussions

To understand the experimentally observed isostructural anomaly at ~ 0.5 GPa and ~ 1.8 GPa, we used first-principles calculations to simulate the rhombohedral phase (SG: $R\bar{3}m$) of $TlBiS_2$ as a function of pressure.

5.3.1 Evolution of electronic structure

Electronic structure of $TlBiS_2$ calculated including spin-orbit interaction at the optimized lattice constants reveals a direct band gap of 0.10 eV. Band gap estimated here is slightly lower than the experimental bandgap of 0.42 eV, which is typical of DFT calculations of band gaps. The electronic structure of $TlBiS_2$ exhibits valleys at the Γ and F points of the Brillouin zone. The valence band maximum (VBM) at the Γ valley has a higher energy than the VBM at the F valley [see Fig. 5.2(b)], whereas the conduction band minima (CBM) at the Γ valley is lower in energy than the CBM at the F valley. The band gaps estimated using optimized lattice constants (ambient pressure) at Γ and F points are 0.09 eV and 0.33 eV respectively [see Fig. 5.2(b)].

With increasing hydrostatic pressure, the CBM and VBM in both the valleys come closer and cross each other resulting in inversion of bands. A close examination of the

electronic structure reveals that the critical pressures (P_C^Γ and P_C^F) marking band inversions at the Γ and F points are different. With increasing hydrostatic pressure from -1 GPa to 4 GPa, the energy gap at the Γ point first closes and then reopens at $P \sim 0$ GPa, and a similar behaviour is found at F point with a critical pressure $P \sim 3$ GPa [see Fig. 5.2(e)]. These values of critical pressures (P_C^Γ and P_C^F) differ from previous calculations [31], primarily because of differences in estimated lattice constants due to different pseudopotentials, and exchange correlation functionals. At the Γ point, the band inversion occurs in between -0.5 and -0.3 GPa (i.e., $-0.5 < P_C^\Gamma < -0.3$ GPa, hence $P_C^\Gamma \sim -0.4$ GPa).

Inversion of bands is evident in the isosurfaces of charge densities [see Fig. 5.3(a)] associated with VBM and CBM at -0.3 and -0.5 GPa. On the other hand since the band gap separating the VBM and CBM at the F point is higher than the gap between them at the Γ point a higher pressure is required for the band inversion to occur at F point. Examining the isosurfaces of charge densities associated with VBM and CBM at the F point [see Fig. 5.3(b)] at 3.5 and 3.7 GPa, it is clear that band inversion at the F point occurs in between 3.5 and 3.7 GPa (i.e., $3.5 < P_C^F < 3.7$ GPa, hence $P_C^F \sim 3.6$ GPa). Evolution of electronic structure with hydrostatic pressure corroborates that $TlBiS_2$ remains a direct band gap semiconductor up to 4 GPa with bulk band gaps of 0.10, 0.17, 0.14, 0.03, 0.07 and 0.19 eV for pressures of 0, 1, 2, 3 and 4 GPa respectively. At pressure (P) ~ 2 GPa we observe a shift in the conduction band minimum and valence band maximum at the Γ to those at the F point. With increasing hydrostatic pressure, the Fermi level [marked with the dashed horizontal black line in Figs. 5.2(a) to 5.2(e)] does not cross the top valence band and bottom conduction band indicating that $TlBiS_2$ does not undergo a semiconductor to metal phase transition. The robust semiconducting nature of $TlBiS_2$ is also established from the evolution of electronic density of states (DOS) with hydrostatic pressure [see Fig. 5.4(c)].

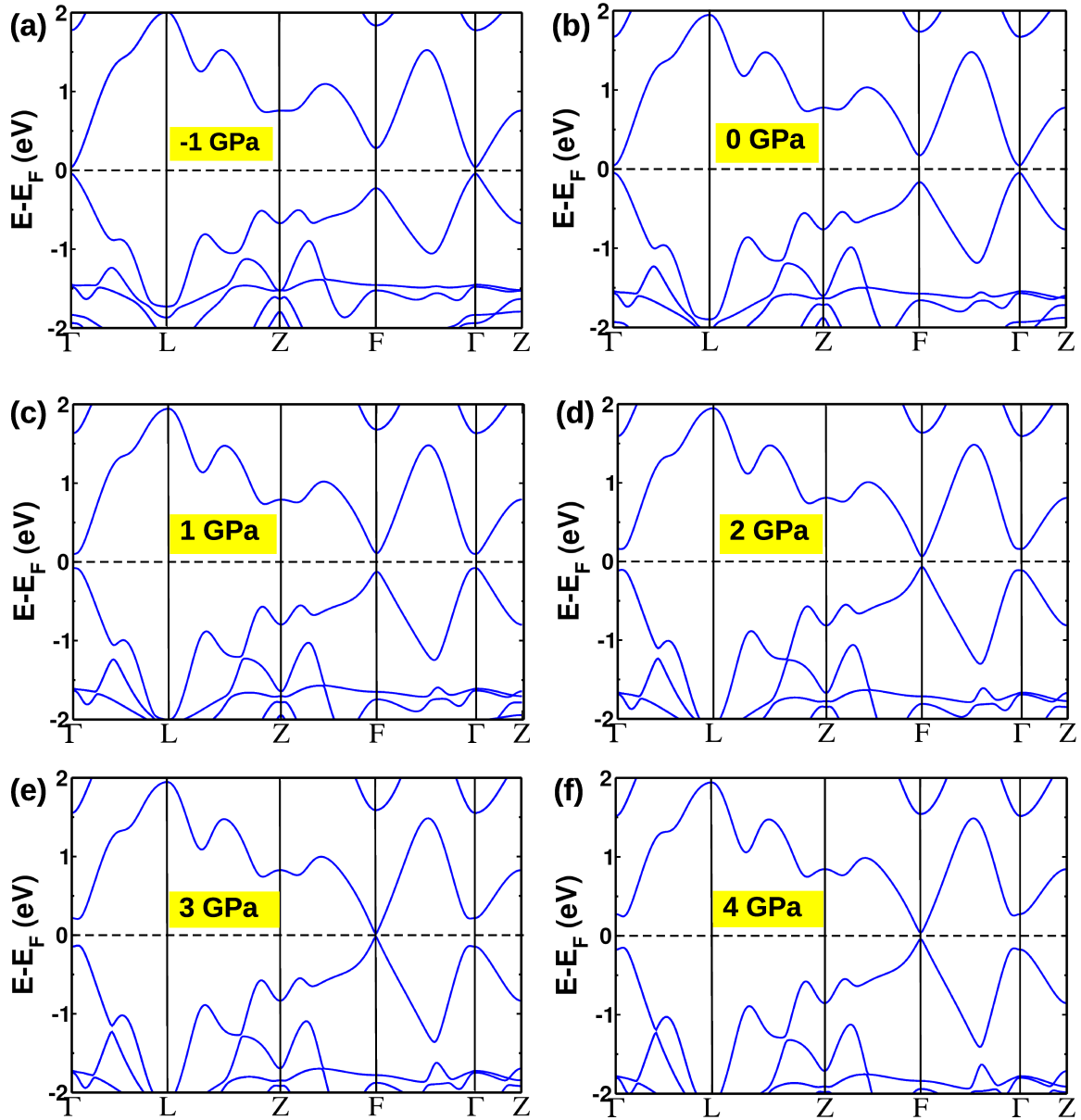


Figure 5.2: (a) – (f) Electronic structure of $TlBiS_2$ are calculated with spin-orbit coupling at different hydrostatic pressures (from -1 GPa to 4 GPa). Band inversion takes place at the Γ and F points in the Brillouin zone as a function of pressure near $P_C = -0.4$ GPa and $P_C = 3.6$ GPa, respectively.

5.3.2 Calculation of topological invariants

Bulk electronic topology of $TlBiS_2$ was investigated as a function of pressure in order to confirm its topological quantum phase transition (TQPT). A TQPT is typically indicated by the crossing of valence and conduction bands at the critical pressures (P_C^Γ and P_C^F).

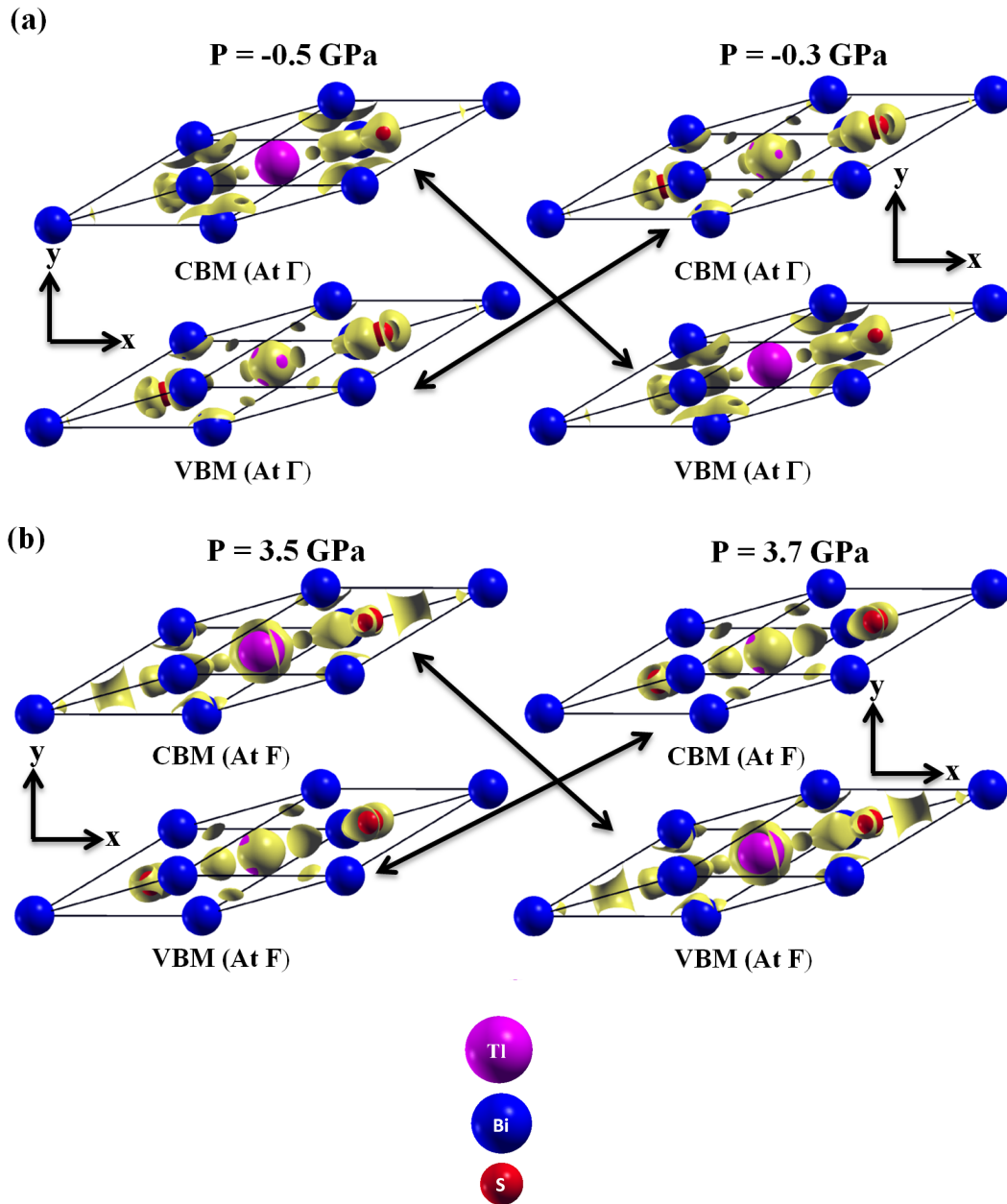


Figure 5.3: *Isosurfaces of charge densities associated with valence band maxima (VBM) and conduction band minima (CBM) before and after the band inversion at the Γ point (a) and the F point (b) reveal that the band inversion at Γ takes place in between -0.3 GPa and -0.5 GPa (i.e., $-0.5 < P_C < -0.3$ GPa, hence $P_C \sim -0.4$ GPa at Γ point), whereas the band inversion at the F point occurs in between 3.5 and 3.7 GPa (i.e., $3.5 < P_C < 3.7$ GPa, $P_C \sim 3.6$ GPa at F point).*

To verify the change in topology due to band inversion we determined the strong Z_2 topological index using a robust, quantitative and exact method as employed in the Z2PACK code [27]. The strong Z_2 topological invariant (ν_0) of $TlBiS_2$ calculated at -0.5 GPa and

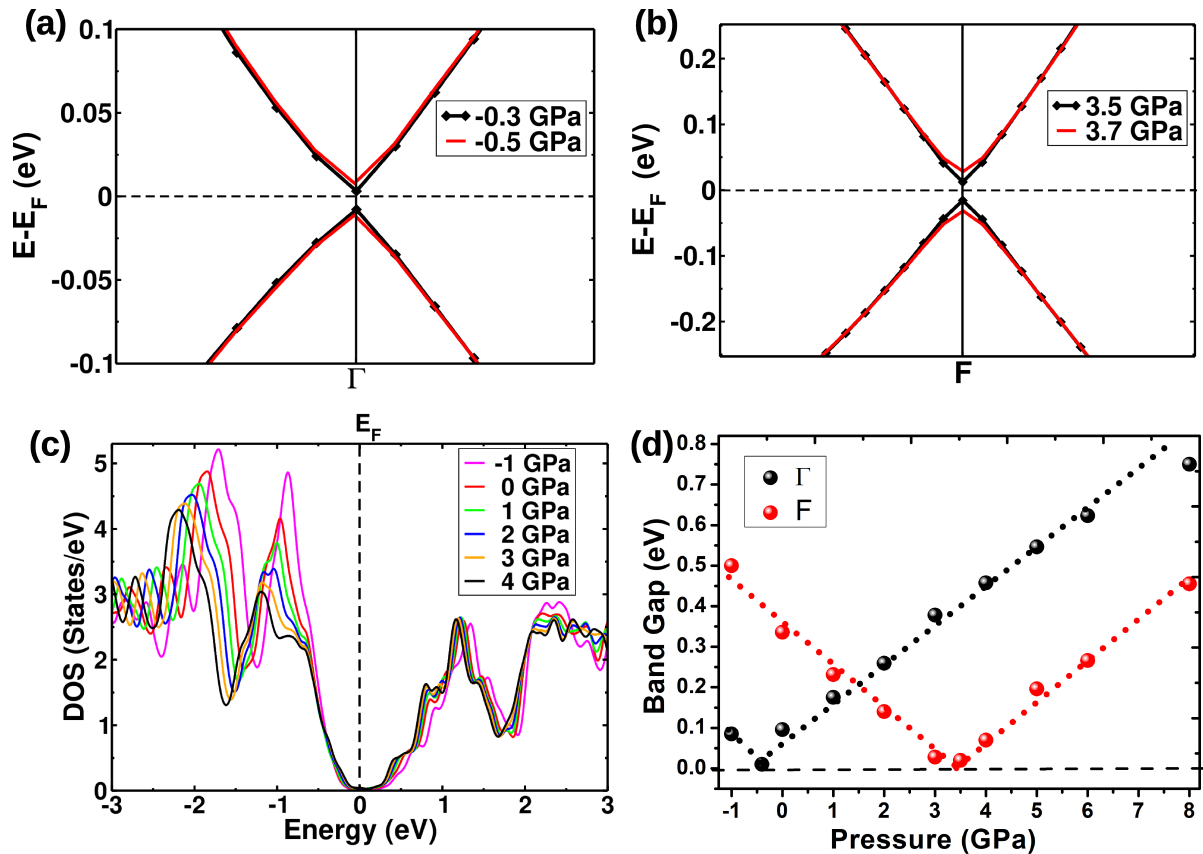


Figure 5.4: *Electronic structures of rhombohedral $TlBiS_2$ around the Γ point (a) and the F point (b) showing the band inversion between the top valence and lowest conduction bands as a function of hydrostatic pressures. Band inversion takes place in the Brillouin zone near $P_C = -0.4$ GPa at Γ point and $P_C = 3.6$ GPa at F point. Electronic density of states of $TlBiS_2$ calculated with spin-orbit coupling at different hydrostatic pressures (c). Evolution of band gap with hydrostatic pressure at Γ and F points showing opening and closing of gaps at the critical pressures (P_C^Γ and P_C^F).*

-0.3 GPa is $\nu_0=0$ (normal insulator) and $\nu_0=1$ (topological insulator) respectively. Thus Z_2 topological index confirms the change in electronic topology and establishes the non-trivial band topology of $TlBiS_2$ at pressures greater than $P_C^\Gamma \sim -0.4$ GPa. We find that the topological invariants calculated at -1, 0, 1, 2, and 3 GPa ($\nu_0 = 0, \nu_0 = 1, \nu_0 = 1, \nu_0 = 1$ and $\nu_0 = 1$ respectively), are consistent with the band inversion picture.

To probe the effect of second band inversion which occurs at F point on the electronic topology we examined the Z_2 topological invariant at 3.5 GPa and 3.7 GPa. $TlBiS_2$ changes from a strong topological insulator at 3.5 GPa ($\nu_0 = 1$) to a system with trivial topology at 3.7 GPa ($\nu_0 = 0$). Thus, the Z_2 topological index based argument confirms a

trivial phase resulting from even number of band inversions at the time-reversal invariant momenta. The topological invariant Z_2 calculated at 4, 5, 6, and 8 GPa are all $\nu_0 = 0$, hence revealing the topological trivial topology of $TlBiS_2$ after the second critical pressure $P_C^F \sim 3.6$ GPa.

The even number of band inversions is an indicator of the TCI phase. In our system, the band gap closes and reopens with an even number of inversions between the two extreme pressures (-0.4 GPa and 3.6 GPa). This implies that even though the phase above 3.6 GPa cannot be a Z_2 TI, we obtain a TCI phase driven by the mirror symmetry of the hexagonal lattice. Hence we have calculated the mirror Chern number (n_M) as a function of pressure. The mirror Chern number (n_M) of $TlBiS_2$ calculated at 3.5 GPa and 3.7 GPa is $n_M=1$ and $n_M=2$ (topological crystalline insulator) respectively. Thus n_M confirms the change in electronic topology and establishes the non-trivial band topology of $TlBiS_2$ with respect to TCI phase characterized by $n_M = 2$ at pressures greater than 3.6 GPa. In summary, ongoing from -0.5 GPa to -0.3 GPa the odd number of inversions occurring at Γ point results in a change of Z_2 topological invariant from 0 to 1. At pressures greater than 3.6 GPa i.e. following the second band inversion a total even number of inversions (3 from F and 1 from Γ) results in $n_M = 2$ and Z_2 topological index 0. The comparison between invariant quantities Z_2 and n_M are shown in the Table III.

Pressure(GPa)	Z_2 Topological index	Mirror Chern number (n_M)
3.5	1	1
3.6	0	2

Table 5.1: *Mirror Chern number (n_M) and Z_2 topological index of $TlBiS_2$ calculated at 3.5 GPa and 3.7 GPa. The second band inversion at F around $P_C^F \sim 3.6$ GPa results in a TCI phase characterized by n_M and $\nu_0=0$ (trivial with respect to Z_2 topological insulators)*

5.3.3 Vibrational Properties

Raman experiments show anomalies in the line widths of A_{1g} and E_g mode at ~ 0.5 GPa and ~ 1.8 GPa indicating isostructural electronic transition in $TlBiS_2$. In order to

theoretically examine the changes in A_{1g} and E_g mode we calculate the phonon frequencies using linear response theory including the effects of electron phonon coupling (EPC). At 0 GPa the calculated frequencies 234 cm^{-1} and 200 cm^{-1} for A_{1g} and E_g modes respectively agree well with their experimental counterparts 242 cm^{-1} (A_{1g}) and 210 cm^{-1} (E_g). For both A_{1g} and E_g modes, the trend of its increasing frequency with pressure is captured correctly by our calculations, and is consistent with experiments.

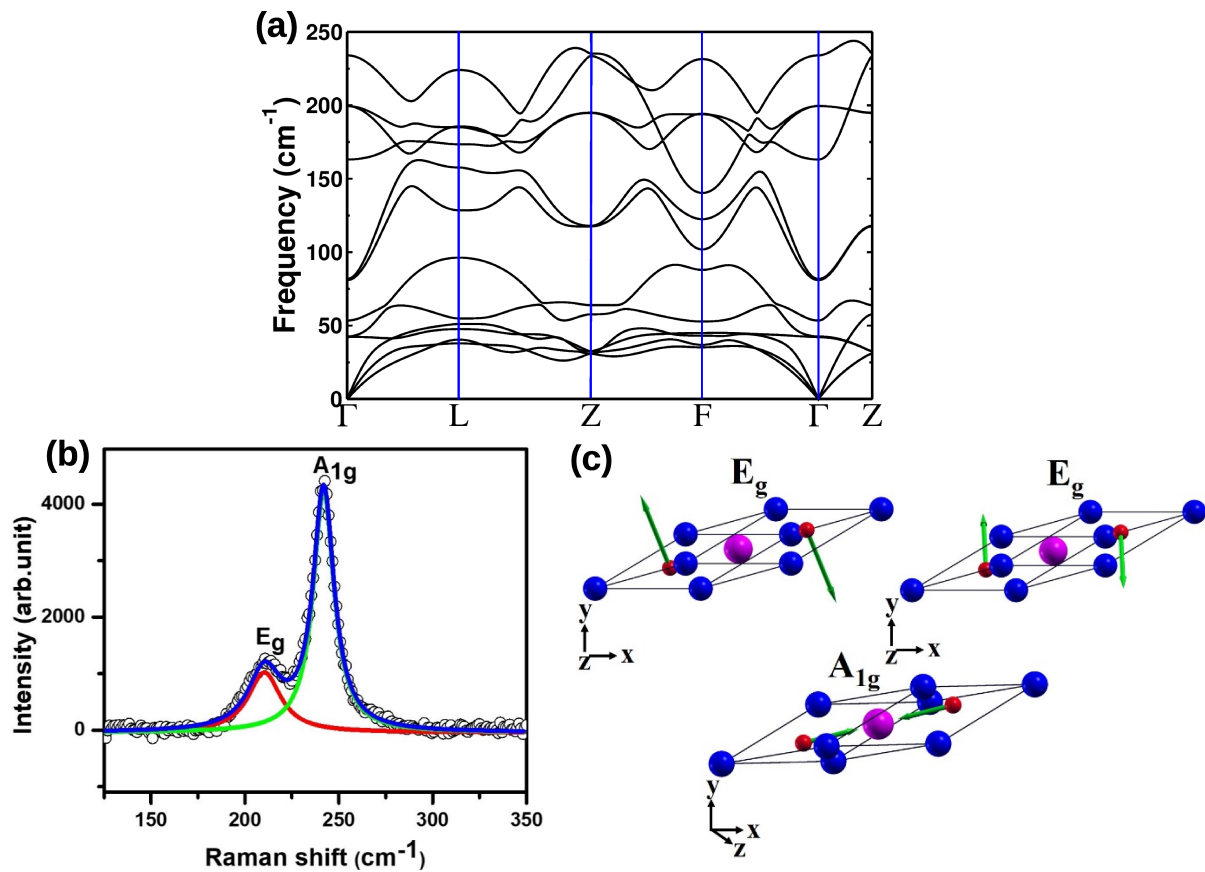


Figure 5.5: *Phonon dispersion of TlBiS₂ for theoretical lattice constant at 0 GPa (a). At 0 GPa negative frequencies are not present in the system indicating a stable structure. (b) Experimental Raman spectrum of TlBiS₂ at an ambient conditions, and (c) visualization of the atomic displacement patterns for the E_g and A_{1g} modes obtained from calculations.*

We note that there are changes in slope ($=d\omega/dP$) of pressure dependence of both the Raman active phonon modes at ~ 3 GPa [see Fig. 5.6(a) and 5.6(b)]. Figure 5.6(c) and 5.6(d) shows that E_g mode couples more strongly with electrons than A_{1g} mode. Though E_g mode does not show any significant change in EPC with pressure the EPC of A_{1g} mode

shows a sharp fall at ~ 3 GPa. The reduction of EPC can be a result of gap closing at ~ 3.6 GPa, where we had found the band inversion. Thus, there is clear correlation between changes in the slopes of Raman active modes as a function of pressure, and topological quantum phase transitions obtained within the same theoretical framework.

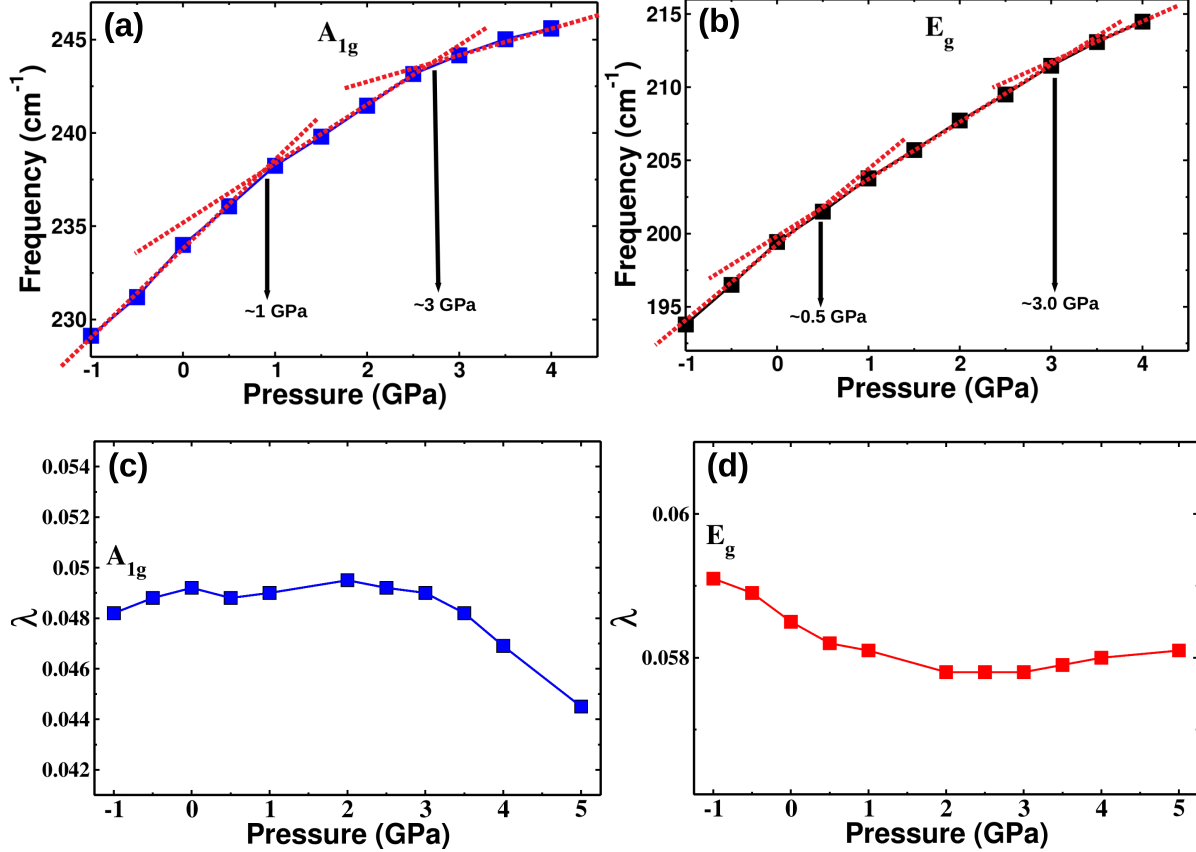


Figure 5.6: Changes in the DFT calculated frequencies of Raman active, (a) E_g and (b) A_{1g} modes of $TlBiS_2$ with pressure (from 0 GPa to 4 GPa). The changes in the electron phonon coupling of these modes are shown in (c,d). There are changes in slope ($=d\omega/dP$) of pressure dependence of both the Raman active phonon modes at ~ 3 GPa.

5.4 Conclusions

As a function of pressure $TlBiS_2$ exhibits two band inversions; first band inversion at Γ point followed by the second one at F point. As a consequence there are changes in the electronic topology of the system, confirmed with Z_2 topological invariant calculated at various pressures. We have attributed the two isostructural electronic transitions at 0.5

GPa and 1.80 GPa respectively to the non-trivial TQPT ($Z_2 = 1$) and TCI ($n_M = 2$) transitions based on our first principles theoretical calculations. Thus, our DFT calculations show that the observed anomalies in the FWHM of phonon modes are connected with topological phase transitions at -0.4 GPa and 3.6 GPa.

Bibliography

- [1] M. Z. Hasan and C. L. Kane, *Rev. Mod. Phys.* **82**, 3045 (2010).
- [2] B. A. Bernevig, T. L. Hughes and S.C. Zhang, *Science* **314**, 1757 (2006).
- [3] M. König, S. Wiedmann, C. Brüne, A. Roth, H. Buhmann, L. W. Molenkamp, X.-L. Qi and S.-C. Zhang, *Science* **318**, 766 (2007).
- [4] H. Zhang, C.X. Liu, X.-L. Qi, X. Dai, Z. Fang and S.C. Zhang, *Nat. Phys.* **5**, 438 (2009).
- [5] Y. Xia, D. Qian, D. Hsieh, L. Wray, A. Pal, H. Lin, A. Bansil, D. Grauer, Y. S. Hor, R. J. Cava and M. Z. Hasan, *Nat. Phys.* **5**, 398 (2009).
- [6] Y. L. Chen, J. G. Analytis, J. H. Chu, Z. K. Liu, S. K. Mo, X. L. Qi, H. J. Zhang, D. H. Lu, X. Dai, Z. Fang, S. C. Zhang, I. R. Fisher, Z. Hussain and Z. X. Shen, *Science* **325**, 178 (2009).
- [7] D. Hsieh, Y. Xia, D. Qian, L. Wray, F. Meier, J. H. Dil, J. Osterwalder, L. Patthey, A. V. Fedorov, H. Lin, A. Bansil, D. Grauer, Y. S. Hor, R. J. Cava and M. Z. Hasan, *Phys. Rev. Lett.* **103**, 146401 (2009).
- [8] M. S. Bahramy, B. J. Yang, R. Arita and N. Nagaosa, *Nat. Commun.* **3**, 679 (2012).
- [9] X. Xi, C. Ma, Z. Liu, Z. Chen, W. Ku, H. Berger, C. Martin, D. B. Tanner and G. L. Carr, *Phys. Rev. Lett.* **111**, 155701 (2013).
- [10] L. Fu, C. L. Kane and E. J. Mele, *Phys. Rev. Lett.* **98**, 106803 (2007).

-
- [11] J. C. Y. Teo, L. Fu, and C. L. Kane, Phys. Rev. B **78**, 045426 (2008).
- [12] L. Fu, Phys. Rev. Lett. **106**, 106802 (2011).
- [13] Y. Tanaka, Z. Ren, T. Sato, K. Nakayama, S. Souma, T. Takahashi, K. Segawa, and Y. Ando, Nat. Phys **8**, 800 (2012).
- [14] T. H. Hsieh, H. Lin, J. Liu, W. Duan, A. Bansil, and L. Fu, Nat. Commun. **3**, 982 (2012).
- [15] W. Liu, X. Peng, C. Tang, L. Sun, K. Zhang and J. Zhong, Phys. Rev. B **84**, 245105 (2011).
- [16] A. Bera, K. Pal, D. V. S. Muthu, S. Sen, P. Guptasarma, U. V. Waghmare and A. K. Sood, Phys. Rev. Lett. **110**, 107401 (2013).
- [17] Y. L. Chen, Z. K. Liu, J. G. Analytis, J. H. Chu, H. J. Zhang, B. H. Yan, S. K. Mo, R. G. Moore, D. H. Lu, I. R. Fisher, S. C. Zhang, Z. Hussain and Z. X. Shen, Phys. Rev. Lett. **105**, 266401 (2010).
- [18] Q. Zhang, Y. Cheng and U. Schwingenschlögl, Sci. Rep. **5**, 8379 (2015).
- [19] R. J. Cava, H. Ji, M. K. Fuccillo, Q. D. Gibson and Y. S. Hor, J. Mater. Chem. C **1**, 3176 (2013).
- [20] T. Sato, K. Segawa, K. Kosaka, S. Souma, K. Nakayama, K. Eto, T. Minami, Y. Ando and T. Takahashi, Nat. Phys. **7**, 840 (2011).
- [21] Quantum-ESPRESSO is a community project for high-quality quantum-simulation software, based on density-functional theory, and coordinated by P. Giannozzi. See <http://www.quantum-espresso.org> and <http://www.pwscf.org>.
- [22] X. Hua, X. Chen, W. A. Goddard III, Phys. Rev. B **55**, 16103 (1997).
- [23] J. P. Perdew, K. Burke, M. Ernzerhof, Phys. Rev. Lett. **77**, 3865 (1996).

-
- [24] Kresse, Georg, and D. Joubert, *Phys. Rev. B* **59**, 1758 (1999).
- [25] A. Dal Corso, *Comput. Mat. Sci.* **95**, 337 (2014).
- [26] S. Baroni, S. de Gironcoli, A. Dal Corso, and P. Giannozzi, *Rev. Mod. Phys.* **73**, 515 (2001).
- [27] D. Gresch, G. Autès, O. V. Yazyev, M. Troyer, D. Vanderbilt, B. A. Bernevig, and A. A. Soluyanov, *Phys. Rev. B* **95**, 075146 (2017).
- [28] A. A. Soluyanov and D. Vanderbilt, *Phys. Rev. B* **83**, 235401 (2011).
- [29] J. Bhattacharjee and U. V. Waghmare, *Phys. Rev. B* **71**, 045106 (2005).
- [30] Ozer, M., K. M. Paraskevopoulos, A. N. Anagnostopoulos, S. Kokou, and E. K., *Semicond. Sci. Technol.* **11**, 1405 (1996).
- [31] Zhang, Qingyun, Yingchun Cheng, and Udo Schwingenschlögl, *Scientific reports* **5**, 8379 (2015).

Chapter 6

Raman study of pressure induced phase transitions in a topological crystalline insulator SnTe and a normal semiconductor SnSe*

6.1 Introduction

SnTe, a narrow band-gap IV-VI semiconductor with a band-gap of ~ 0.2 eV at room temperature [1], has stimulated intense interest due to being a topological Crystalline Insulator (TCI) [2]. Here the metallic surface states are protected by the mirror symmetry of the crystal as compared to Z_2 topological insulators where the surface states are protected by the time-reversal symmetry [3]. TCIs have multiple surface states associated with particular crystal surfaces. Angle resolved photoemission spectra (ARPES) have confirmed that SnTe has four Dirac cone surface states on $\{100\}$, $\{111\}$ and $\{110\}$ surfaces in the first surface Brillouin zone [2, 4]. TCI's are characterized by a 'mirror chern' number [5],

*Raman study of pressure induced phase transitions in a topological crystalline insulator SnTe and a normal semiconductor SnSe: Sukanya Pal, Raagya Arora, Subhajit Roychowdhury, Kaniska Biswas, D. V. S. Muthu, U. V. Waghmare, and A. K. Sood (**Preprint available**)

a new topological invariant, associated with these surface states. SnTe is also a “negative band gap” material whose ordering of conduction and valence band near the Fermi energy is inverted compared to normal semiconductors like PbTe [6–9]. This band inversion takes place near the L points in the Brillouin zone where the valence band maximum has L_6^- symmetry and the conduction band minimum has L_6^+ symmetry. Low temperature Raman study has revealed a phase transition at $T_c \sim 105\text{K}$ from ambient $Fm\bar{3}m$ structure to rhombohedral structure of space group $R3m$ due to softening of a phonon mode [10] arising from strong coupling between interband electronic transitions and the transverse optic phonon. This structure transition is accompanied by a ferroelectric phase transition [11] and electrical transport shows a kink in the resistivity curve at the T_c [12]. The Transition temperature depends on the carrier concentration in the sample, decreasing with higher carrier density [13, 14]. On further lowering the temperature, a second phase transition occurs at 22K from rhombohedral to orthorhombic structure [15].

We now review the high pressure studies done so far on SnTe. Resistance gradually decreases as the pressure increases but at ~ 1.8 GPa suddenly the resistance increases by 360 percentage and again gradually decreases a pressure is increased further. This transition is also accompanied by a first order structural phase transition from sodium chloride to orthorhombic crystal structure (space group $Pnma$) as revealed by x-ray diffraction [16]. But another First-principles calculations show that band-gap reduces to zero at 1.5 GPa and then gradually opens up at higher pressures [17]. However, subsequent angle dispersive x-ray studies along with first principles structural calculations argued that SnTe undergo a reversible phase transition from cubic $Fm\bar{3}m$ to the intermediate structures ($Pnma$, $Cmcm$ and GeS type structures) at 4.1 GPa and the transition to the final $Pm\bar{3}m$ state begins at 18.1 GPa. The transitions at 4.1 GPa and 18.1 GPa are associated with change in volume, indicating their first order nature [18]. Further first principle calculations showed that the high pressure ($Pm\bar{3}m$) phase is superconducting, having a critical temperature of $\sim 7.5\text{K}$, which decreases with further increase of pressure [19].

SnSe is a p-type IV-VI semiconductor with an indirect band gap of ~ 0.9 eV and a direct

band gap of ~ 1.3 eV [20]. At ambient conditions it has a layered orthorhombic structure with $Pnma$ space group which can be viewed as distorted NaCl structure. Similar to other IV-VI binary semiconductors like GeSe, SnS, GeS, SnSe has covalent interaction between the atoms (with its three neighbors) within the layers. Each layer consists of zig-zag double-layer planes of the tin and selenium atoms and these layers are separated by a weak vander Waals force. The center of inversion lies in between the double layers [21,22].

High pressure has intense effect in crystallographic and electronic structures which in turn effects the energy band gap of materials. Some of the earlier studies on the high-pressure behaviors of SnSe are revisited here: One of the earliest dispersive x-ray diffraction study showed that SnSe does not undergo any phase transition up to 34 GPa [23]. Electrical resistivity study showed a dependency with pressure where the electrical resistance decreased around 6.5 GPa indicating a change in energy gap of the material [24]. A recent study using first-principles calculations suggests that SnSe transforms from orthorhombic ($Pnma$) structure to orthorhombic ($Cmcm$) structure at ~ 7 GPa and remains in semiconducting state in the $Cmcm$ phase indicating no pressure induced electronic transitions at this pressure [25]. A recent synchrotron radiation study showed that high-pressure phase of SnSe has an orthorhombic structure with $Pbnm$ symmetry and the transition takes place around 10.5 GPa [26]. Another study with electrical transport measurements, first-principles calculations along with X-ray diffraction data, has shown that SnSe undergoes an electronic transition from semiconducting to semimetallic state around 12.6 GPa followed by an orthorhombic to monoclinic structural transition [27].

Thus it is clear that the effect of pressure on structural and electrical properties of SnTe and SnSe has not been clearly understood till date and our aim in this paper is to investigate the pressure induced phase transitions of these two semiconductors by Raman scattering; in particular to look for the pressure dependence of Raman phonon frequencies and their linewidths. Our results reveal a topological phase transition only for SnTe at 1.8 GPa and other two structural phase transitions around 6 and 12 GPa for both SnTe and SnSe.

6.2 Computational Methods

Our first-principles calculations are based on density functional theory (DFT) employing the Quantum ESPRESSO [28] (QE) code. To treat the exchange and correlation energy of electrons, we used a generalized gradient approximation (GGA) [29] with a functional parametrized by Perdew, Burke, and Ernzerhof (PBE) [30]. The projector augmented wave (PAW) potentials [31] with valence configuration $4d^{10} 5s^2 5p^2$, $4d^{10} 5s^2 5p^4$ and $3d^{10} 4s^2 4p^4 4d^{-2}$ were adopted for Sn, Te and Se respectively.

Expansion of wave functions and charge density in plane wave basis set was truncated with energy cut-off of 50 Ry and 500 Ry respectively. The discontinuity in occupation numbers of the electronic states at the Fermi level was smeared with an energy width of $k_B T = 0.005$ Ry in the Fermi-Dirac distribution function. Face-centered cubic ($Fm\bar{3}m$), orthorhombic (Pnma, Pnma[GeS] type and Cmcm) and cubic ($Pm\bar{3}m$) phases of SnTe were theoretically analyzed to understand the experimentally observed pressure dependent phase transitions. In calculations of cubic ($Fm\bar{3}m$) structure of SnTe, the Brillouin zone (BZ) integrations were sampled with a uniform mesh of $16 \times 16 \times 16$ k points, while for orthorhombic (Pnma and Cmcm) and cubic ($Pm\bar{3}m$) unit cells, the Brillouin zone (BZ) integrations were sampled with a uniform mesh of $8 \times 8 \times 8$ and $8 \times 10 \times 10$ k points respectively.

To study the pressure dependent phase transitions in SnSe, its orthorhombic Pnma and Cmcm structures were analyzed. For Pnma phase wave functions and charge density were represented in plane wave basis sets truncated with cut-off energies of 45 Ry and 400 Ry respectively and fixed at 45 Ry and 360 Ry for Cmcm phase. The discontinuity in occupation numbers of electronic states was smeared using a Fermi-Dirac distribution function with broadening of $k_B T = 0.003$ Ry. Brillouin Zone (BZ) integrations were sampled on uniform $8 \times 10 \times 10$ and $10 \times 8 \times 10$ meshes of k-points for Pnma and Cmcm structures respectively.

To determine pressure-dependent structure and phonon spectra we used scalar-relativistic PAW potentials to optimize the structure with respect to lattice constants and atomic

coordinates, through minimization of enthalpy, $H = E + PV$ at a given pressure. Lattice dynamical properties were calculated using self-consistent linear response theory within DFT (known as density functional perturbation theory [33]) as implemented in the QE distribution [28].

To obtain phonon dispersion of $Fm\bar{3}m$ phase of SnTe and $Cmcm$ phase of SnSe, interatomic force constant matrices were obtained at q -vectors on a $4 \times 4 \times 4$ mesh and $2 \times 1 \times 1$ meshes respectively, and dynamical matrices at an arbitrary q -vector were obtained using Fourier interpolation. Effects of spin-orbit coupling (SOC) were included in our calculations of electronic structure through the use of fully relativistic [32] potentials.

To assess electronic topology of SnTe, we have used Z2Pack code [34] to determine the Z_2 topological invariant and the mirror chern number (n_M). This involves use of hybrid Wannier functions [35, 36] and employs the idea of time reversal polarization in calculations of the Z_2 invariants.

6.3 Results and Discussion

6.3.1 SnTe

SnTe, a narrow band-gap IV-VI semiconductor with a band-gap of 0.2 eV at room temperature [37], has stimulated intense interest due to its non trivial topological Crystalline Insulating (TCI) [38] nature. Its metallic surface states are protected by the mirror symmetry of the crystal as compared to Z_2 topological insulators where the surface states are protected by the time-reversal symmetry [39]. TCIs are characterized by a non-zero mirror Chern number, with individual Chern numbers C_i and \bar{C}_i defined on a mirror-invariant plane. The mirror Chern number [40, 41] defined as $n_M = (C_{+i} - C_{-i})/2$ can be used as a topological invariant of a TCI. A TCI supports an even number of Dirac cones in its surface electronic structure and band inversions in sharp contrast to a Z_2 TI exhibiting odd number of band inversions. The first experimental [38] observation of TCI phase was reported in SnTe, following a theoretical prediction [39].

We now present theoretical calculations to understand its pressure dependent transitions at $P = 2$ GPa, 4 GPa, 11 GPa and 18 GPa observed in experiments. Our estimates of the optimized lattice constant of cubic ($Fm\bar{3}m$) phase of SnTe is $a = 6.37$ Å, which is within the typical errors of GGA calculations relative to the experiment [42] ($a = 6.32$ Å). Electronic structure of SnTe calculated with spin-orbit interaction at the optimized lattice constants reveals a band gap of 0.015 eV, a bit underestimated with respect to its experimental value [37] of 0.03 eV, which is typical of DFT estimates of band gaps. SnTe is a "negative" band gap material with inverted ordering of conduction and valence bands in comparison with normal semiconductor like PbTe [43–46]. This band inversion takes place near the L points in the Brillouin zone where the valence band maximum has L_6^- symmetry and the conduction band minimum has L_6^+ symmetry.

With increasing hydrostatic pressure, CBM and VBM at the L point move away from each other and the band gap increases (See Fig. 6.1d). The band gap at L point increases from 0.015 eV at 0 GPa to 0.4 eV at 5 GPa. A close examination of the electronic structure near the L point (See Fig. 6.1a and 6.1b) reveals a crossing among the conduction bands on moving from 0 GPa to 2 GPa. The band inversion at the L point between the CBM and 2nd CBM is evident from the isosurfaces of charge densities (See Fig. 6.1e) associated with these conduction bands evolving across the critical pressure. Such band inversion is an indicator of electronic topological transition (ETT) in materials, and hence motivates us to check the bulk electronic topology of SnTe. Symmetry analysis shows that parity of the electronic wave functions at CBM and 2nd CBM are L_6^+ and L_6^- . To proceed with the symmetry based arguments, we determined Z_2 topological index using a robust and more accurate method as implemented in the Z2Pack code. The calculated Z_2 topological invariant (ν_0) of SnTe remains zero before and after the band inversion, confirming no change in its electronic topology, and establishing the trivial band topology of SnTe with respect to Z_2 . In SnTe, there could be changes in electronic topology with respect to TCI phase, as SnTe is a topological crystalline insulator at ambient conditions. Therefore, we study the evolution of the mirror Chern numbers (n_M) as a function of pressure. The

mirror Chern numbers (n_M) of SnTe calculated at 0 GPa and 2 GPa are $n_M=2$. Clearly, $n_M=2$ confirms robust non trivial TCI phase of SnTe at pressures greater than the critical pressure.

To probe this further, we monitored effects of hydrostatic pressure on its zone center Γ) point optical phonon modes. A compression of the unit cell leads to hardening of all the three degenerate optical Γ_{15} modes (See Fig. 6.2a), as evident in the phonon density of states (See Fig. 6.2e). Upon application of hydrostatic pressure, the Γ point instability at $\omega \sim -43$ i cm^{-1} vanishes and a stable structure is obtained at $P \geq 1$ GPa exhibiting Γ point optical mode frequency of 40 cm^{-1} . Anomalous behaviour of this optical phonon modes on moving from 0 GPa to 2 GPa (See Fig. 6.2c) corroborates the experimentally observed changes in Raman spectra at 1.8 GPa. Concurrent anomalous evolution of the electron phonon coupling with pressure across the critical pressure (See Fig. 6.2d) further validates the subtle Raman changes observed at low pressure.

To investigate the pressure dependent structural phase transition to orthorhombic (Pnma, Pnma [GeS type], Cmcm) phases, we estimated the changes in enthalpy (ΔH) of these structures and the cubic ($Fm\bar{3}m$) structure relative to Pnma phase. Fig. 6.3 shows that the ΔH of the cubic structure with respect to orthorhombic (Pnma) phase increases monotonically with pressure and attains a positive value at 5.8 GPa. Thus, we predict a cubic ($Fm\bar{3}m$) to orthorhombic (Pnma) structural phase transition at 5.8 GPa correlating with the experimentally observed Raman changes at 5 GPa. Further, we find that the orthorhombic Pnma structure of SnTe remains stable up to 21 GPa. To theoretically investigate the possibility of the experimentally observed 12 GPa phase transition, electronic structures of orthorhombic Pnma and Pnma (GeS type) phases have been calculated. Here, we examine the electronic properties of these polymorphs of SnTe in the intermediate pressure range (See Fig. 6.4 and 6.5). At 6 GPa, electronic structure shows that the overlap between the conduction and valence bands makes Pnma (GeS type) structure metallic (See Fig. 6.5a), while Pnma is a zero band gap semiconductor (See Fig. 6.4a). With increasing hydrostatic pressure the band gap of the Pnma phase decreases in

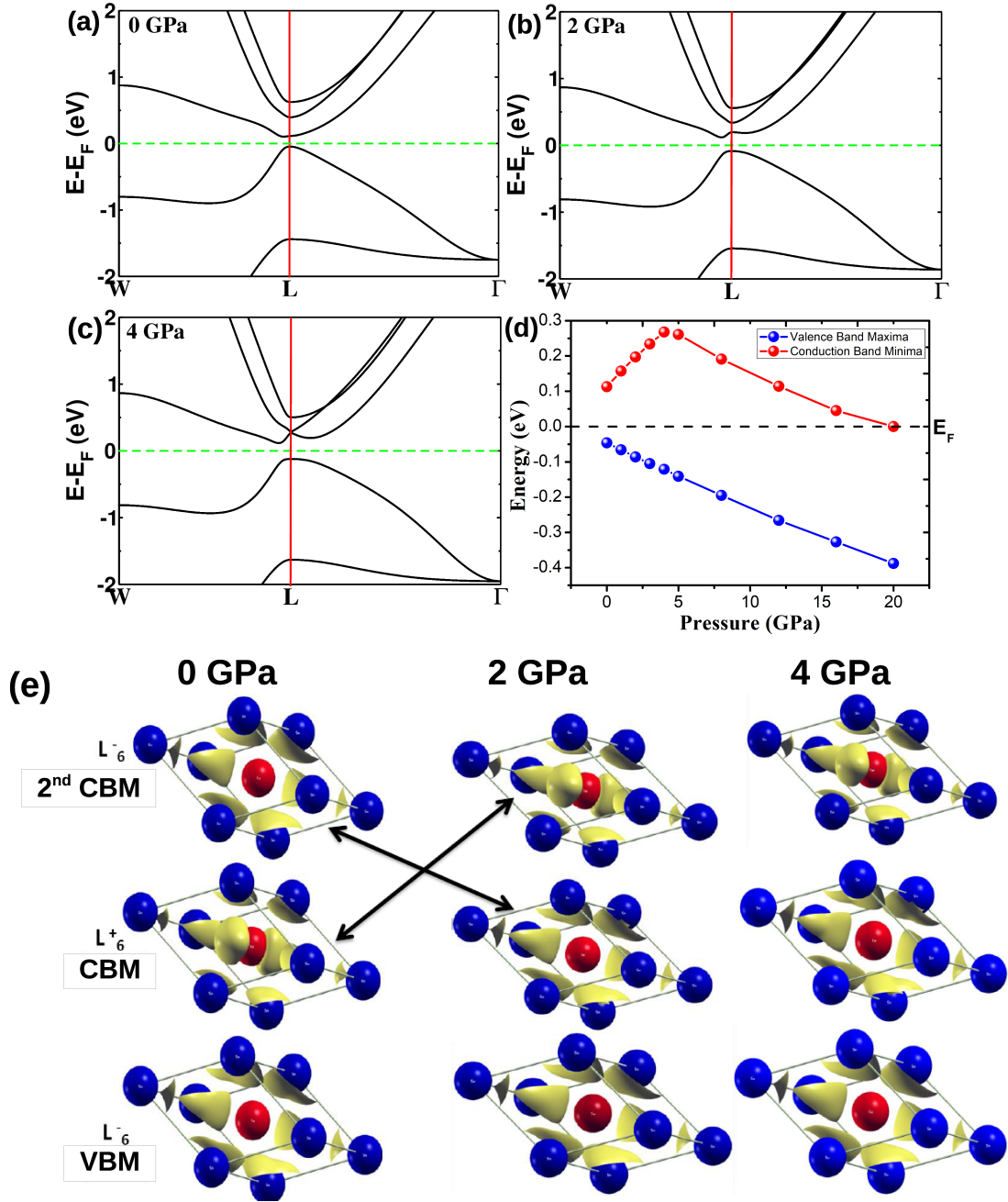


Figure 6.1: *Electronic structure of cubic ($Fm\bar{3}m$) phase of SnTe calculated with spin-orbit coupling at (a) 0 GPa, (b) 2 GPa and (c) 4 GPa and variation in VBM and CBM with pressure at the L point of the Brillouin zone (d). Isosurfaces of charge densities (e) associated with electronic states at valence band maximum (VBM), conduction band minimum (CBM) and 2nd conduction band minimum at L point below (a) and above (b) the critical pressure revealing inversion of the lowest two conduction bands at this transition.*

magnitude (See Fig. 6.4b to 6.4f), and at $P=8$ GPa the metallization of the Pnma phase is achieved, through an indirect band gap closure along the X Γ Z directions. In addition,

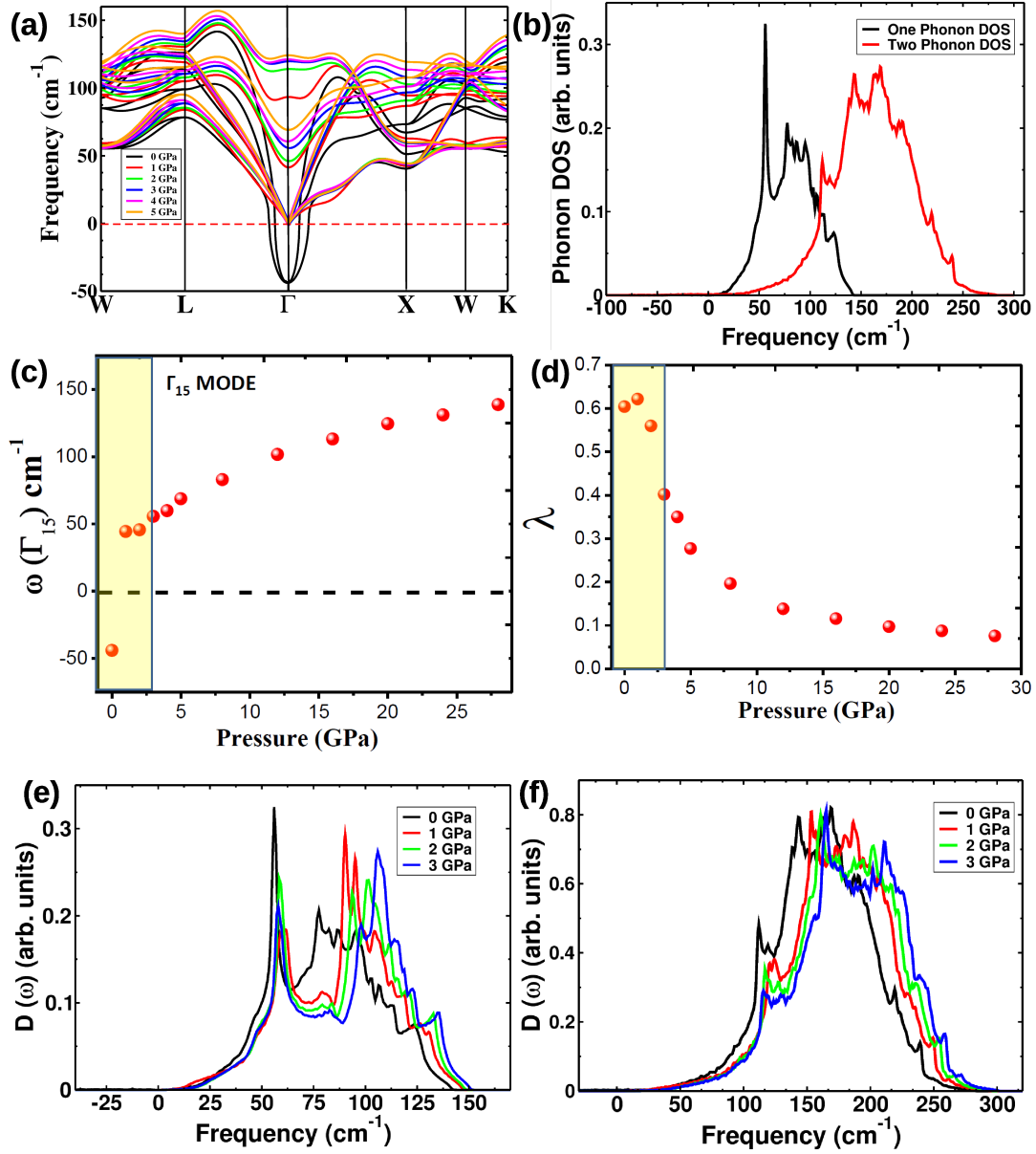


Figure 6.2: Calculated phonon dispersion of the cubic ($Fm\bar{3}m$) structure of SnTe at pressures ranging from 0 GPa to 5 GPa (a), exhibiting imaginary phonon frequencies depicting the instability of cubic structure at $P = 0$ GPa. One and two phonon density of states of cubic SnTe at 0 GPa (b). Calculated frequency ω of the optical phonon (Γ_{15}) at Γ point as a function of pressure showing an anomaly at low pressures and its electron-phonon coupling in (d). Evolution of one phonon DOS (e) and two phonon DOS (f) with hydrostatic pressure ranging from 0 GPa to 3 GPa.

the VBM at T-point crosses the Fermi level at pressure of 11 GPa (See Fig. 6.4c). With increasing hydrostatic pressure the enhanced metallic behaviour of Pnma phase is also evident from the increased density of states at the Fermi level (See Fig. 6.4g.) Although Pnma (GeS type) phase remains metallic throughout the range of intermediate pressures,

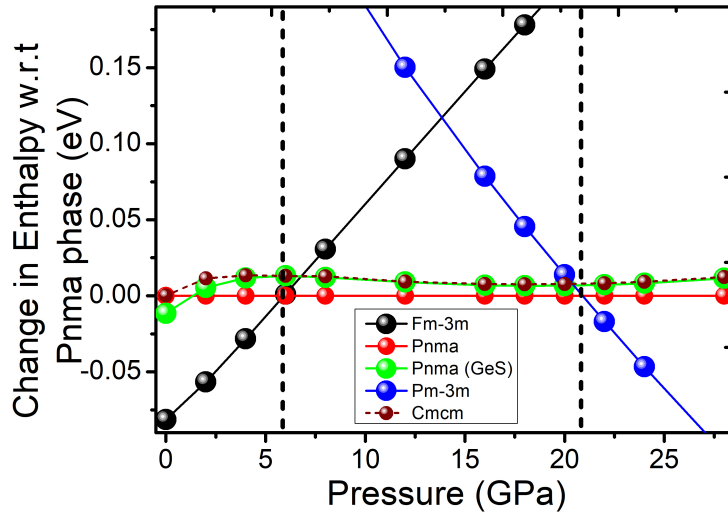


Figure 6.3: Pressure dependent enthalpy (ΔH) of cubic $Fm\bar{3}m$, orthorhombic $Pnma$ (GeS), $Cmcm$ and cubic $Pm\bar{3}m$ phases of $SnTe$ relative to the orthorhombic $Pnma$ phase

it shows enhanced density of states at the Fermi level with increasing pressures (See Fig. 6.5g). This is attributed to the additional contribution of valence bands along the UX direction near E_F and new valence bands crossing the Fermi level along XS direction at ~ 13 GPa (See Fig. 6.5e).

However these electronic structure calculations are not sufficient to analyze the experimentally observed phase transition. To explore the 12 GPa phase transition further, we analyze Γ point phonons of the orthorhombic $Pnma$ and $Pnma$ (GeS) structures were studied. At 16 GPa, the $Pnma$ (GeS) phase exhibits softer Γ point phonon modes than those of $Pnma$ phase (See Fig. 6.6). The observed evolution of Raman modes across the transition pressure of 12 GPa also point to a similar trend. We therefore attribute the experimentally observed Raman changes in $SnTe$ at 12 GPa to the coexistence of orthorhombic $Pnma$ (GeS) and $Pnma$ structures. The presence of $Pnma$ (GeS) phase above 12 GPa pressure thus results in lower frequency phonon modes. The difference in enthalpy of $Pnma$ and $Pnma$ (GeS) phases (See Fig. 6.3) decreases from 13 meV to 7 meV on moving from 8 GPa to 16 GPa hinting the possibility of their coexistence at $P > 12$ GPa, correlating with experimentally observed Raman changes. To analyze the

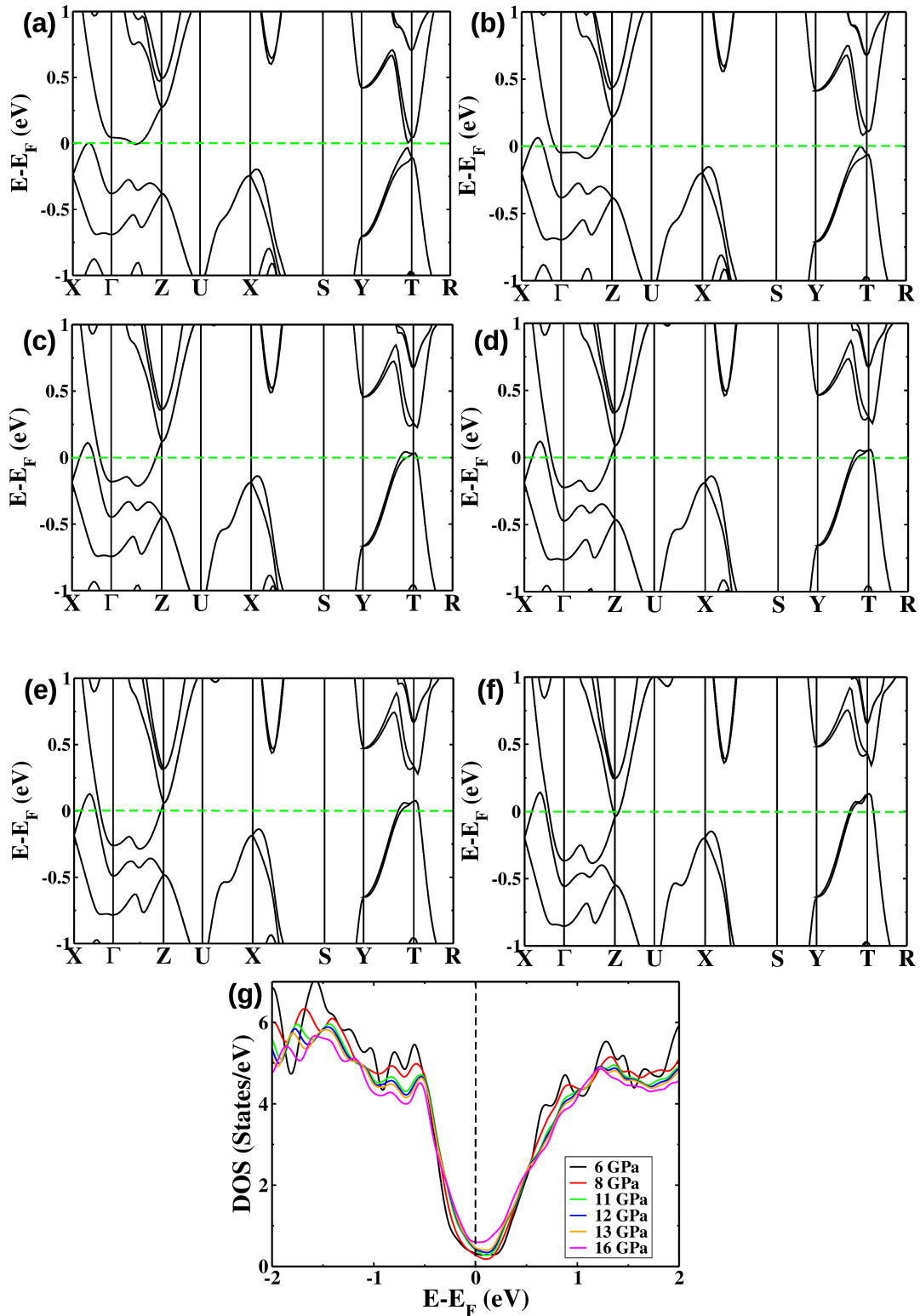


Figure 6.4: *Electronic structure of the orthorhombic ($Pnma$) structure of SnTe at $P = 6$ GPa (a), 8 GPa (b), 11 GPa (c), 12 GPa (d), 13 GPa (e) and 16 GPa (f) calculated with the inclusion of effects of the spin orbit coupling and corresponding electronic density of states showing enhanced metallicity with increasing pressure (g).*

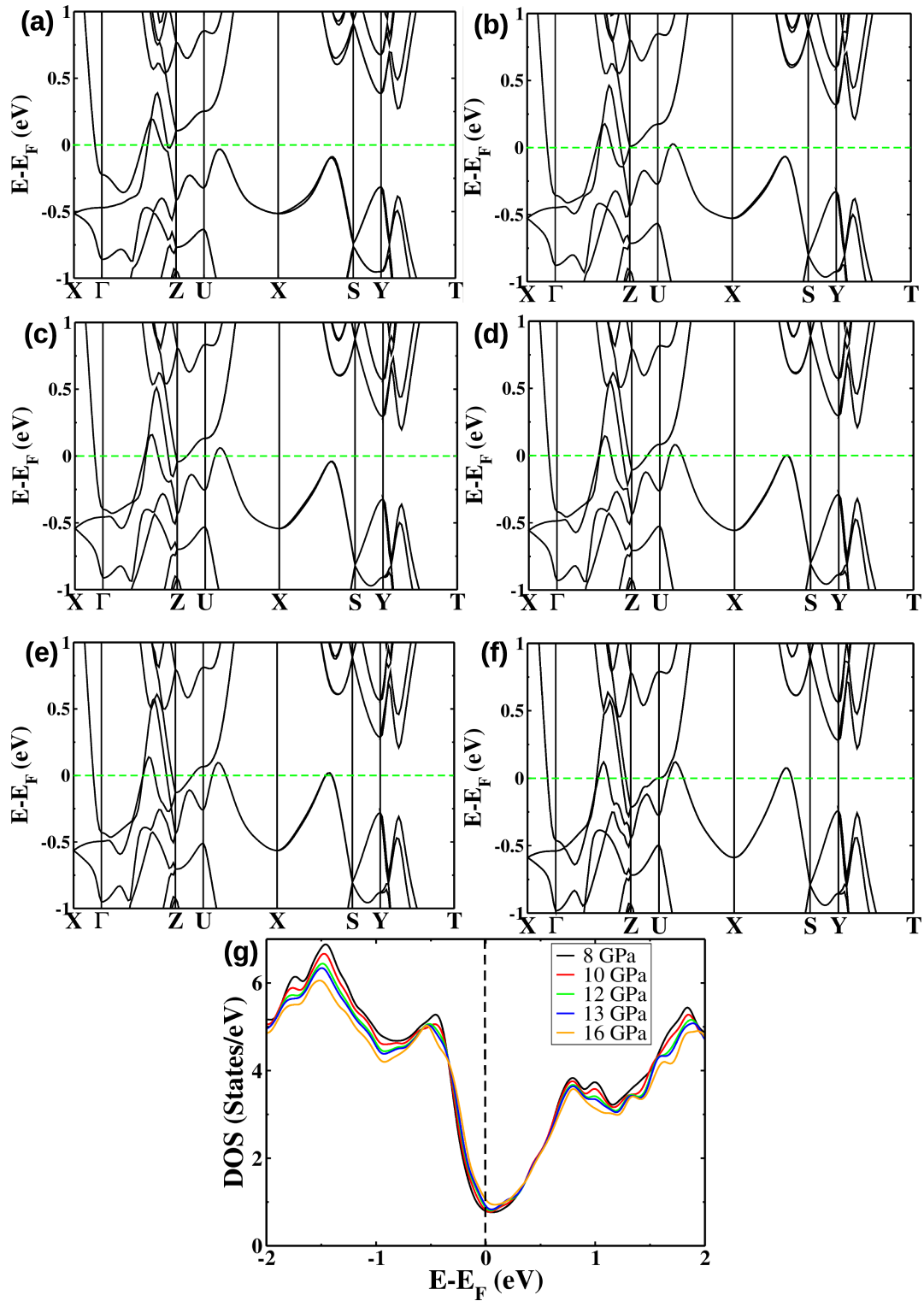


Figure 6.5: *Electronic structure of the orthorhombic $Pnma$ (GeS type) structure of SnTe at $P = 6$ GPa (a), 8 GPa (b), 10 GPa (c), 12 GPa (d), 13 GPa (e) and 16 GPa (f) calculated with the inclusion of spin-orbit coupling. Electronic density of states calculated with spin-orbit coupling at different hydrostatic pressures (g).*

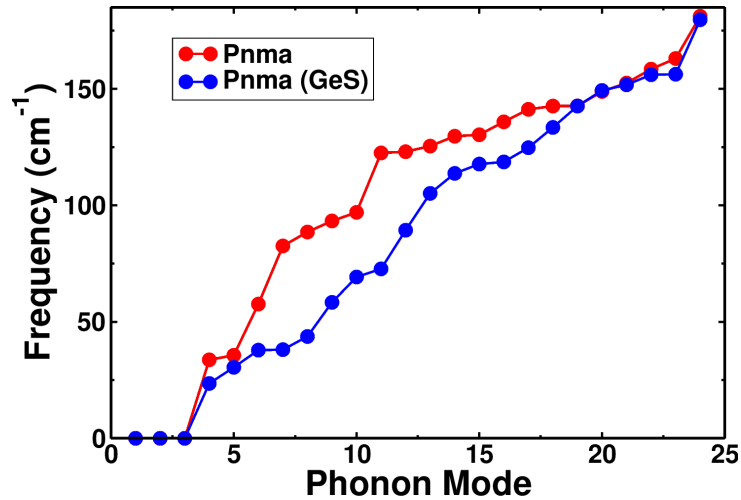


Figure 6.6: *Frequencies of the zone centre (Γ) optical phonons of Pnma and Pnma (GeS type) phases at 16 GPa showing notably softer optical phonon modes of Pnma (GeS) phase in comparison to Pnma phase*

pressure dependent phase transition from Pnma to cubic ($Pm\bar{3}m$) phase, we obtained the changes in enthalpy of these structures, and find a phase transition from orthorhombic Pnma phase to cubic phase at 21 GPa (See Fig. 6.3).

6.3.2 SnSe

We now discuss our results on SnSe, where the experimentally observed Raman transitions take place at pressures of 6.2 GPa and 12.9 GPa. Experimentally the changes in pressure coefficients of mode frequencies (dw/dP) and disappearance or appearance of new modes indicate possible transitions at high pressures. To understand the experimentally observed pressure anomaly in SnSe, we used first-principles calculations to simulate the orthorhombic Pnma and Cmc m phases of SnSe as a function of pressure. At ambient conditions SnSe has a layered orthorhombic crystal structure with Pnma space group having eight atoms per unit cell and experimental lattice parameters [47] $a=11.57$ Å, $b=4.19$ Å and $c=4.46$ Å. Our estimates of its lattice constant are $a=11.77$ Å, $b=4.22$ Å and $c=4.53$ Å, which are within typical overestimation of GGA calculations compared to their experimental values. Electronic structure of orthorhombic Pnma SnSe calculated including spin-orbit interaction at the optimized lattice constants reveals an indirect band

gap of 0.71 eV. Band gap estimated here is slightly lower than the experimental bandgap of 0.90 eV [48], typical of DFT calculations of band gaps. Under compression, both VBM and CBM gradually move towards the Fermi level, and the energy band gap reduces from 0.7 eV at 0 GPa to 0.1 eV at 6 GPa. (See Fig. 6.7a to 6.7e). Thus, Pnma phase of SnSe undergoes a semiconductor-semimetallic phase transition at hydrostatic pressure of ~ 6 GPa.

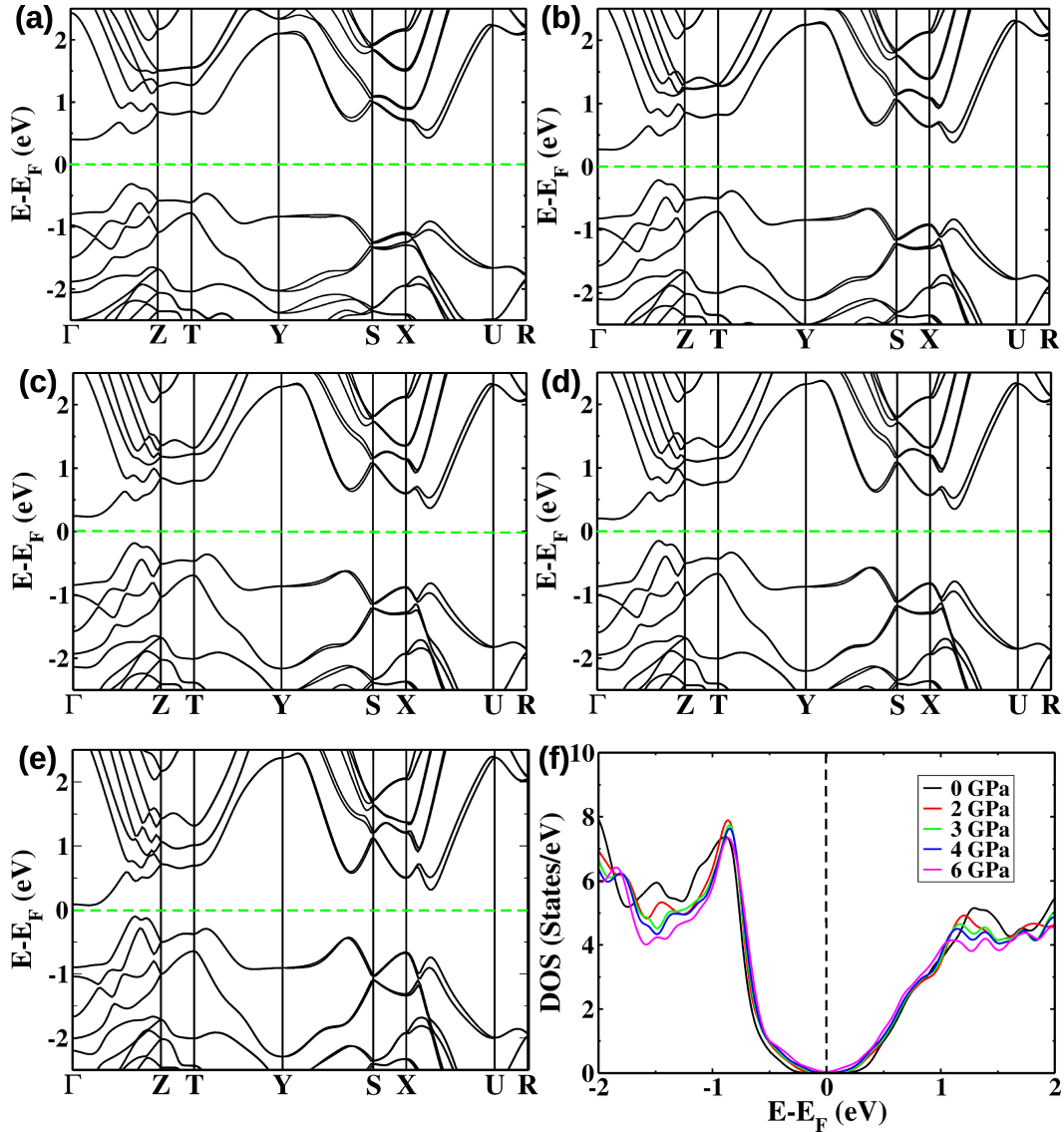


Figure 6.7: *Electronic structure of the orthorhombic (Pnma) structure of SnSe at $P = 0$ GPa (a), 2 GPa (b), 3 GPa (c), 4 GPa (d), and 6 GPa (e) calculated with the inclusion of effects of the spin-orbit coupling and corresponding electronic density of states showing enhanced DOS at Fermi level with increasing pressure (f)*

To investigate the pressure dependent structural phase transition to orthorhombic

(Cmcm) phase, we estimated changes in enthalpy (ΔH) of the orthorhombic Cmcm phase and the Pnma phase of SnSe. ΔH of the Pnma structure increases with pressure and attains a positive value at 6.3 GPa (Fig. 6.8). At $P=6.3$ GPa, clearly our calculations predict a structural phase transition from the Pnma to Cmcm structure correlating with the experimentally observed Raman anomalies at 6 GPa.

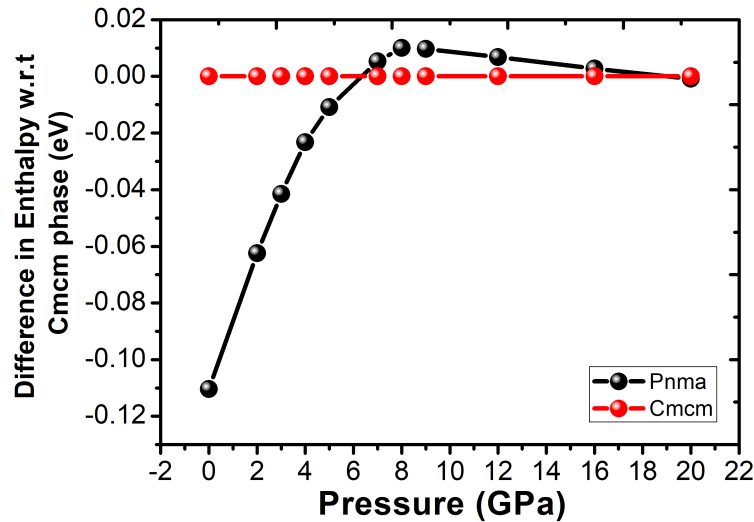


Figure 6.8: *Pressure dependent enthalpy (ΔH) of the orthorhombic Pnma phase of SnTe relative to the orthorhombic Cmcm phase, demonstrating a structural phase transition from Pnma to Cmcm phase at $P = 6.3$ GPa*

Our theoretical estimates of lattice parameters of Cmcm structure of SnSe are $a = b = 4.29$ Å and $c = 11.93$ Å respectively, which compares well with experimental characterization [49] (Cmcm: $a, c = 4.31$ Å, $b = 11.70$ Å). At 0 GPa, its electronic structure (calculated including spin-orbit coupling) reveals well separated valence bands and conduction bands across the gap of a 0.2 eV (See Fig. 6.9). With increasing hydrostatic pressure, evolution of electronic structure reveals emergence of semi-metallic behaviour of Cmcm phase of SnSe, with valence band maxima (VBM) and conduction band minima (CBM) crossing each other at 7 GPa (See Fig. 6.9b). Thus with increasing hydrostatic pressure (from 0 GPa to 7 GPa), Cmcm phase undergoes a insulator to semi-metal phase transition accompanied by a structural phase transition from Pnma to Cmcm phase at ~ 6.3 GPa. To probe the experimentally observed transition at 13 GPa, band structure

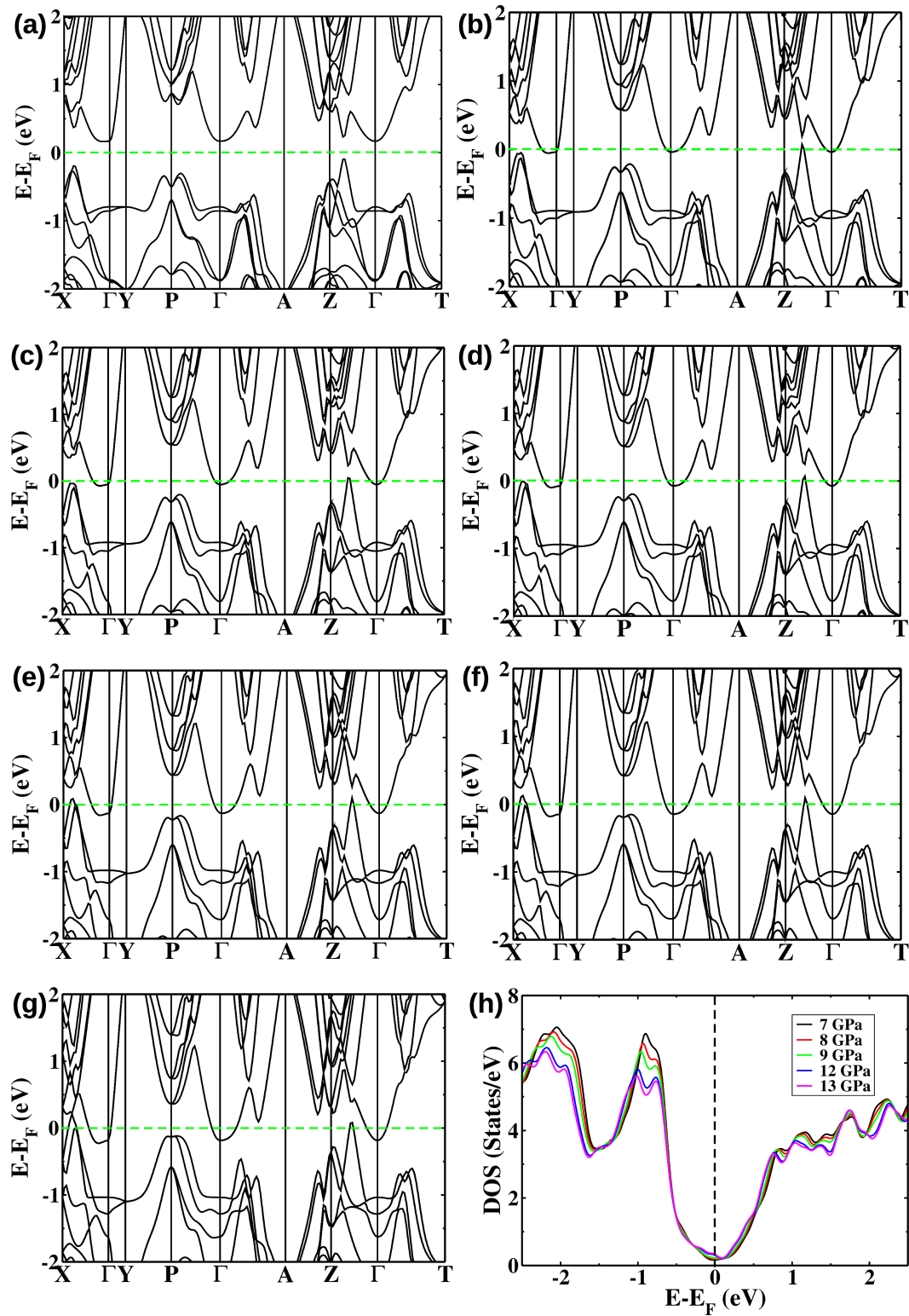


Figure 6.9: *Electronic structure of the orthorhombic ($Cmcm$) structure of $SnSe$ at $P = 0$ GPa (a), 7 GPa (b), 8 GPa (c), 9 GPa (d), 12 GPa (e), 13 GPa (f) and 16 GPa (g) calculated with the inclusion of spin-orbit coupling and corresponding electronic density of states (h).*

and phonons for Cmc m phase of SnSe were calculated and examined closely. The Cmc m phase shows enhanced density of states at the Fermi level with increasing hydrostatic pressures (Fig. 5h). This is attributed to the additional contribution of conduction bands

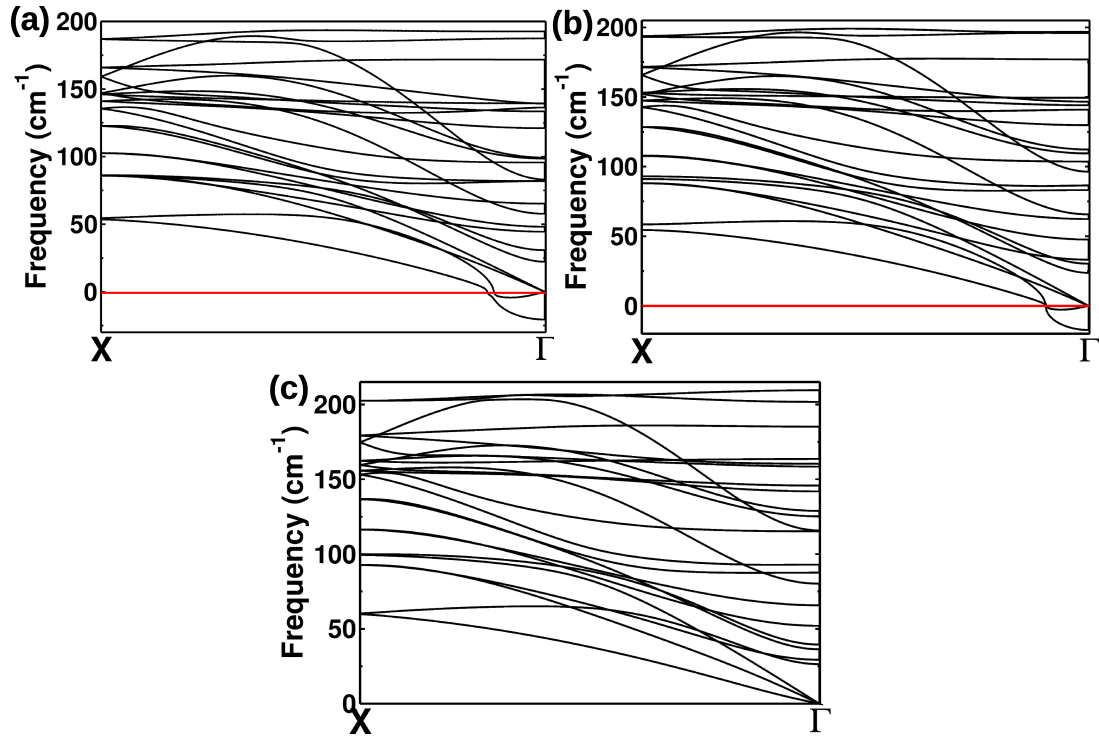


Figure 6.10: *Phonon dispersion of orthorhombic (Cmc m) structure of SnSe at $P = 9$ GPa (a), 12 GPa (b) and 16 GPa (c) calculated along the $X\Gamma$ direction.*

at Fermi level with increasing hydrostatic pressure and new valence bands along ΓX direction crossing the Fermi level at ~ 12 GPa (See Fig. 6.9e). Consequently, Cmc m phase of SnSe undergoes a semi-metal to metal transition at ~ 12 GPa. Examining the phonons of Cmc m phase along the ΓX direction reveals an instability at 9 GPa (Fig. 6.10a). On compression, the instability reduces and a stable structure exhibiting no imaginary frequencies is obtained at 16 GPa (Fig. 6.10c). The transition observed in experiments at 12.9 GPa is thus identified as a semi-metal to metal transition (occurring at 12 GPa in our calculations).

6.4 Conclusions

Our DFT calculations show that the low pressure (1.8 GPa) Raman anomalies in SnTe are most likely associated with band inversion occurring among conduction bands as a function of pressure, though there is no change in the electronic topology of SnTe. The transition at $P = 5$ GPa and 11 GPa in SnTe are associated with cubic ($Fm\bar{3}m$) to orthorhombic (Pnma) structural phase transition and the onset of coexistence of orthorhombic Pnma and Pnma (GeS) phases respectively.

Our theoretical analyses of the experimentally observed Raman anomalies in SnSe at 6 GPa and 13 GPa shows that phase transition at 6 GPa is associated with a structural phase transition from Pnma to Cmc m phase, and the transition at 13 GPa correlates with semi-metal to metal transition.

Bibliography

- [1] L. Esaki and P. J. Stiles., Phys. Rev. Lett. **16**, 1108 (1966).
- [2] Y. Tanaka, Zhi Ren, T. Sato, K. Nakayama, S. Souma, T. Takahashi, Kouji Segawa, and Yoichi Ando., Nat Phys **8**, 800 (2012).
- [3] Timothy H. Hsieh, Hsin Lin, Junwei Liu, Wenhui Duan, Arun Bansil, and Liang Fu., Nat Commun **3**, 982 (2012).
- [4] Junwei Liu, Wenhui Duan, and Liang Fu., Phys. Rev. B **88**, 241303 (2013).
- [5] Jeffrey C. Y. Teo, Liang Fu, and C. L. Kane., Phys. Rev. B **78**, 045426 (2008).
- [6] Sohrab Rabi., Phys. Rev. **182**, 821 (1969).
- [7] J. O. Dimmock, I. Melngailis, and A. J. Strauss., Phys. Rev. Lett. **16**, 1193, (1966).
- [8] Y. W. Tung and Marvin L. Cohen., Phys. Rev., **180**, 823 (1969).
- [9] J S Melvin and D C Hendry. Journal of Physics C: Solid State Physics **12**, 3003 (1979).
- [10] S. Sugai, K. Murase, and H. Kawamura. Solid State Communications, **23**, 127 (1977).
- [11] L. J. Brillson, E. Burstein, and L. Muldower., Phys. Rev. B **9**, 1547 (1974).
- [12] S. Katayama and D. L. Mills., Phys. Rev. B **22**, 336 (1980).
- [13] K. L. I. Kobayashi, Y. Kato, Y. Katayama, and K. F. Komatsubara., Phys. Rev. Lett. **37**, 772 (1976).

-
- [14] S. Sugai, K. Murase, S. Katayama, S. Takaoka, S. Nishi, and H. Kawamura., *Solid State Communications*, **24**, 407 (1977).
- [15] I. Ortalli., *Ferroelectrics* **54**, 325 (1984).
- [16] James A Kafalas and Anthony N Mariano., *Science*, **143**, 952 (1964).
- [17] Wei Li, Qin yu He, Jun fang Chen, Zhong liang Pan, and Teng Wang., *Chemical Physics Letters*, **616**, 196 (2014).
- [18] Dan Zhou, Quan Li, Yanming Ma, Qiliang Cui, and Changfeng Chen., *The Journal of Physical Chemistry C*, **117**, 5352 (2013).
- [19] Dan Zhou, Quan Li, Yanming Ma, Qiliang Cui, and Changfeng Chen., *The Journal of Physical Chemistry C.*, **117**, 12266 (2013).
- [20] I. Lefebvre, M. A. Szymanski, J. Olivier-Fourcade, and J. C. Jumas., *Phys. Rev. B* **58**, 1896 (1998).
- [21] Atsushi Okazaki and Ikuhiko Ueda., *Journal of the Physical Society of Japan*, **11**, 470 (1956).
- [22] H. R. Chandrasekhar, R. G. Humphreys, U. Zwick, and M. Cardona., *Phys. Rev. B* **15**, 2177 (1977).
- [23] Chattopadhyay, T., Werner, A., von Schnering, H.G., and Pannetier, J., *Rev. Phys. Appl. (Paris)*, **19**, 807 (1984).
- [24] A. Agarwal, P. H. Trivedi, and D. Lakshminarayana., *Crystal Research and Technology* **40**, 789, 2005.
- [25] Sebahaddin Alptekin., *Journal of Molecular Modeling* **17**, 2989 (2011).
- [26] I Loa, R J Husband, R A Downie, S R Popuri, and J-W G Bos., *Journal of Physics: Condensed Matter* **27**, 072202 (2015).

-
- [27] Jiejuan Yan, Feng Ke, Cailong Liu, Li Wang, Qinglin Wang, Junkai Zhang, Guanghui Li, Yonghao Han, Yanzhang Ma, and Chunxiao Gao., *Phys. Chem. Chem. Phys.* **18**, 5012 (2016).
- [28] QUANTUM-ESPRESSO is a community project for high-quality quantum-simulation software, based on density-functional theory, and coordinated by P. Giannozzi. See <http://www.quantum-espresso.org> and <http://www.pwscf.org>.
- [29] X. Hua, X. Chen, W. A. Goddard III, *Phys. Rev. B* **55**, 16103 (1997).
- [30] J. P. Perdew, K. Burke, M. Ernzerhof, *Phys. Rev. Lett.* **77**, 3865 (1996).
- [31] Kresse, Georg, and D. Joubert, *Phys. Rev. B* **59**, 1758 (1999).
- [32] A. Dal Corso, *Comput. Mat. Sci.* **95**, 337 (2014).
- [33] S. Baroni, S. de Gironcoli, A. Dal Corso, and P. Giannozzi, *Rev. Mod. Phys.* **73**, 515 (2001).
- [34] D. Gresch, G. Autès, O. V. Yazyev, M. Troyer, D. Vanderbilt, B. A. Bernevig, and A. A. Soluyanov, *Phys. Rev. B* **95**, 075146 (2017).
- [35] A. A. Soluyanov and D. Vanderbilt, *Phys. Rev. B.* **83**, 235401 (2011).
- [36] J. Bhattacharjee and U. V. Waghmare, *Phys. Rev. B* **71**, 045106 (2005).
- [37] L. Esaki and P. J. Stiles, *Phys. Rev. Lett.* **16**, 1108 (1966).
- [38] Y. Tanaka, Zhi Ren, T. Sato, K. Nakayama, S. Souma, T. Takahashi, Kouji Segawa and Yoichi Ando., *Nat Phys* **8**, 800 (2012).
- [39] Timothy H. Hsieh, Hsin Lin, Junwei Liu, Wenhui Duan, Arun Bansil and Liang Fu., *Nat Commun* **3**, 982 (2012)
- [40] Jeffrey C. Y. Teo, Liang Fu, and C. L. Kane, *Phys. Rev. B* **78**, 045426 (2008).
- [41] Liang Fu, *Phys. Rev. Lett.* **106**, 106802 (2011)

-
- [42] J.H.C. Hogg, H. H. Sutherland, *Acta Cryst. B* **24**, 1968 (1982).
- [43] Sohrab Rabii, *Phys. Rev.*, **182**, 821 (1969).
- [44] J. O. Dimmock, I. Melngailis and A. J. Strauss, *Phys. Rev. Lett.* **16**,1193 (1966).
- [45] Y. W. Tung and Marvin L. Cohen, *Phys. Rev.* **180**, 823 (1969).
- [46] J S Melvin and D C Hendry, *Journal of Physics C: Solid State Physics*, **12**, 3003 (1979).
- [47] Atsushi Okazaki and Ikuhiko Ueda, *Journal of the Physical Society of Japan*, **11**, 470 (1956).
- [48] I. Lefebvre, M. A. Szymanski, J. Olivier-Fourcade and J. C. Jumas, *Phys. Rev. B*, **58**, 1896 (1998).
- [49] Chattopadhyay, T., Pannetier, J. and Vonschnering, H. G., *J. Phys. Chem. Solids* **47**, 879 (1986)